TESE DE DOUTORADO EM COTUTELA ENTRE

UNIVERSIDADE DE BRASÍLIA E SORBONNE UNIVERSITÉ

Área de concentração:

FÍSICO-QUÍMICA – PPGQ/UNB: PROGRAMA DE PÓS-GRADUAÇÃO EM QUÍMICA

FÍSICO-QUÍMICA – ED388: CHIMIE PHYSIQUE ET CHIMIE ANALYTIQUE DE PARIS CENTRE

Dispersões de nanopartículas de ferrita do tipo espinélio em solventes à base de líquidos iônicos para aplicações termoelétricas

Apresentada por

Ana Alice Andrade Meireles Guerra

para a obtenção do título de

Doutora da Sorbonne Université e Doutora da Universidade Brasília

Tese defendida em 09 de dezembro de 2024

Diante da banca composta por:

Dr. Alexandre PARIZE	Universidade Federal de Santa Catarina	Relator
Dra. Darja LISJAK	Jožef Stefan Institute	Relatora
Dr. Leonardo G. PATERNO	Universidade de Brasília	Examinador
Dra. Sophie CASSAIGNON	Sorbonne Université	Examinadora
Dr. Alex F. C. CAMPOS	Universidade de Brasília	Orientador
Dra. Emmanuelle DUBOIS	Sorbonne Université	Orientadora

PhD THESIS IN CO-TUTORSHIP BETWEEN

THE UNIVERSIDADE DE BRASÍLIA AND SORBONNE UNIVERSITÉ

Concentration área:

PHYSICAL CHEMISTRY – PPGQ/UNB: GRADUATE PROGRAM IN CHEMISTRY

PHYSICAL CHEMISTRY – ED388: PHYSICAL CHEMISTRY AND ANALYTICAL CHEMISTRY OF PARIS CENTRE

Dispersions of spinel ferrite nanoparticles in ionic liquid-based solvents in view of thermoelectric applications

Presented by

Ana Alice Andrade Meireles Guerra

in order to obtain the title of

Doctor from Sorbonne University and Doctor from the University of Brasília

Thesis defended in the 09th of December of 2024

In front of the jury composed by:

Dr. Alexandre PARIZE	Universidade Federal de Santa Catarina	Referee
Dra. Darja LISJAK	Jožef Stefan Institute	Referee
Dr. Leonardo G. PATERNO	Universidade de Brasília	Examiner
Dra. Sophie CASSAIGNON	Sorbonne Université	Examiner
Dr. Alex F. C. CAMPOS	Universidade de Brasília	Thesis Director
Dra. Emmanuelle DUBOIS	Sorbonne Université	Thesis Director

In memory of my beloved mother Célia de Andrade M. Guerra

ACKNOWLEDGEMENTS

First, I want to thank my parents for their endless love and support throughout these years. I know that a big part of what I've achieved wouldn't have been possible without them. A special thanks to my mom, who was always there and was the person I loved most to share my happiness with. I know you are still with me. I'll love you forever, mom!

I'd also like to thank my husband for standing by my side through the ups and downs. Thank you for sharing this journey of life with me. Love you!

To the rest of my family, my grandparents, sister, and my husband's family, I'm grateful for your support and for celebrating the good moments together.

Thank you to my lifelong friend, each one of you is truly special. You're always there for the best laughs and memories.

My supervisor, Professor Alex, deserves special thanks for all his support with the science, logistics, and motivation, since my master´s studies. But, above all, thank you for the friendship we've built, which grew stronger through both great and challenging times in France. I hope our partnership continues and you are an example to me in so many ways.

I'm also thankful for my supervisor in France, Dra. Emmanuelle. My year in France was intense, and the results wouldn't be the same without your guidance. Thank you for being supportive and for sharing your lab knowledge and scientific insights. It was a pleasure to get to know you and I hope our collaboration continues. I learned a lot from you.

I'm also grateful to my friends from Maison du Brésil and UnB, whose openness to share a relaxing conversation helped me recharge. Each of you is truly special.

I'm also really grateful for the friends I made at the Phenix lab, all of you made this PhD journey lighter with great moments in and outside the lab. I hope to see you all again somewhere in the world.

Thank you to the teams at the Complex Fluids Laboratory at the Institute of Physics, the Environmental and Applied Nanoscience Laboratory at UnB, and the Phenix lab at Sorbonne Université for all the support.

Finally, I acknowledge the financial support of CAPES for the PhD scholarship and the CAPES-COFECUB program for funding my time in France. My gratitude also

goes to the Distrito Federal Research Foundation for supporting my participation in academic events.

ABSTRACT

The world energy demand has increased due to population growth and technological and economic development. Furthermore, the majority of consumed energy still comes from fossil and non-renewable sources. This situation underscores the need to explore alternative energy solutions, such as thermoelectric materials, which convert thermal energy into electricity via the Seebeck Effect. Thermoelectric devices offer several advantages, including robustness, silent operation, the use of renewable energy sources, and zero greenhouse gas emissions. However, thermoelectric materials present low efficiency, which jeopardizes their applications in large-scale energy conversion. Recent research has shown that thermoelectric materials composed of ferrofluids (FFs) present promising results for thermoelectric applications. Thus, the current study aims to enhance thermoelectric conversion by dispersing charged magnetic nanoparticles (NPs) in liquids, due to their thermodiffusive and magnetic properties. The research focuses on core@shell magnetic NPs ($CoFe_2O_4$@γ-Fe_2O_3) and evaluates how factors like NP composition, size, ligand type, heating, and water content impact colloidal dispersion. These dispersions are examined in pure ionic liquids (ILs), specifically EMIM TFSI, which is particularly suited for thermoelectric applications, as well as in propylene carbonate (PC), a polar organic solvent with much lower viscosity but non-ionic properties. Mixtures of these solvents at varying mole fractions are also studied. Various characterization techniques such as X-ray diffraction (XRD), transmission electron microscopy (TEM), magnetic measurements, dynamic light scattering (DLS), and small angle X-ray scattering (SAXS) are employed to evaluate colloidal dispersion stability, with a specific focus on their potential for thermoelectric applications. Characterization of the precursor FFs revealed that variations in nanoparticle size significantly impacted magnetic properties and surface organization, influencing interparticle interactions. All FFs displayed visual stability immediately after synthesis and one year later, with DLS and SAXS confirming stable clusters, where smaller NPs formed larger clusters. Phosphonic ligands effectively stabilized NPs for non-aqueous transfer, unlike sulphonic ligands, probably due to the core properties of the studied NPs. In EMIM TFSI and PC mixtures, dispersions were stable across all tested compositions, resisting flocculation over several months. The nanoparticles formed smaller clusters in non-aqueous solvents compared to water, with steps like low-pressure pumping and heating enhancing stability. The solvent mixture dispersions at optimal electrical conductivity and reduced viscosity show potential as complex liquids for studying thermoelectricity in liquid thermocells.

Keywords: Thermoelectric materials, ferrofluids, ionic liquids, propylene carbonate, and colloidal stability.

RESUMO

A demanda mundial por energia tem aumentado devido ao crescimento populacional e ao desenvolvimento tecnológico e econômico. Além disso, a maior parte da energia consumida ainda provém de fontes fósseis e não renováveis. Essa situação evidencia a necessidade de explorar alternativas energéticas, como materiais termoelétricos, que convertem energia térmica em eletricidade por meio do Efeito Seebeck. Dispositivos termoelétricos oferecem várias vantagens, incluindo robustez, operação silenciosa, uso de fontes de energia renováveis e zero emissões de gases de efeito estufa. No entanto, esses materiais apresentam baixa eficiência, o que limita suas aplicações em conversão de energia em larga escala. Pesquisas recentes indicam que materiais termoelétricos compostos por ferrofluidos (FFs) apresentam resultados promissores para essas aplicações. Assim, o presente estudo busca aprimorar a conversão termoelétrica dispersando nanopartículas magnéticas carregadas (NPs) em líquidos, devido às suas propriedades termodifusivas e magnéticas. A pesquisa se concentra em NPs magnéticas com estrutura core@shell ($CoFe_2O_4$@γ-Fe_2O_3) e avalia como fatores como composição e tamanho das NPs, tipo de ligante, aquecimento e presença de água impactam a dispersão coloidal. Essas dispersões são analisadas em líquidos iônicos puros, especificamente o EMIM TFSI, particularmente adequado para aplicações termoelétricas, e no propileno carbonato, um solvente orgânico polar com menor viscosidade, mas propriedades não iônicas. Misturas desses solventes em diferentes frações molares também são estudadas. Diversas técnicas de caracterização, como difração de raios X (DRX), microscopia eletrônica de transmissão (TEM), medições magnéticas, espalhamento dinâmico de luz (DLS) e espalhamento de raios X a baixos ângulos (SAXS), são empregadas para avaliar a estabilidade da dispersão coloidal, com foco no potencial para aplicações termoelétricas. A caracterização dos FFs precursores revelou que variações no tamanho das NPs impactaram significativamente as propriedades magnéticas e a organização superficial, influenciando as interações entre partículas. Todos os FFs apresentaram-se visualmente estáveis logo após a síntese e um ano depois, com DLS e SAXS confirmando a formação de clusters estáveis, onde NPs menores formaram clusters maiores. Ligantes fosfônicos estabilizaram efetivamente as NPs para transferência para solventes não aquosos, ao contrário do ligante sulfônico, provavelmente devido às propriedades do núcleo das NPs estudadas. Em misturas de EMIM TFSI e PC, as dispersões se mostraram estáveis em todas as composições testadas, resistindo à floculação por vários meses. As nanopartículas formaram clusters menores em solventes não aquosos em comparação com a água, com etapas como remoção de água por bombeamento a baixa pressão e aquecimento aprimorando a estabilidade. As dispersões nas misturas de solventes, com condutividade elétrica otimizada e viscosidade reduzida, mostram potencial como líquidos complexos para o estudo da termoeletricidade em células termelétricas líquidas.

Palavras-chave: Materiais termoelétricos, ferrofluidos, líquidos iônicos, propileno carbonato e estabilidade coloidal.

Summary

List of Figures

List of Tables

Abbreviations

d_0 – average particle diameter obtained from TEM

d_h – hydrodynamic diameter

DLS – Dynamic Light Scattering

DLVO - Derjaguin, Landau, Verwey, Overbeek

DMSO - dimethyl sulfoxide

d_{rx} – average particle diameter obtained from XRD

EAN - Ethylammonium nitrate

EMIM TFSI - 1-Ethyl-3-methylimidazoliumbis(trifluoromethylsulfonyl)imide

FAAS - Flame Atomic Absorption Spectroscopy

FF – ferrofluid

ICP – MS - Inductively Coupled Plasma – Mass Spectrometry

IL – Ionic Liquids

NPs – Nanoparticles

$PAC_4MIM^{\pm}Br^{-}$ - 1-methyl-3-(butylphosphonic acid) imidazolium bromide

$PAC_6MIM^{\pm}Br^{-}$ - 1-methyl-3-hexylphosphonic acid) imidazolium bromide

PC - Propylene Carbonate

R_g – Radius of gyration

SAXS - Small Angle X-ray Scattering

$SBMIM^{\pm}/TFSI^{-}$ - 1-Methyl-3-(4-sulfobutyl)imidazolium bis(trifluoromethanesulfonyl)imide

SQUID - Superconducting Quantum Interference Device

TEM - Transmission Electron Microscopy

UnB – University of Brasilia

vdW – Van der Waals

XRD – X-ray Diffraction

Introduction

The global energy demand has increased significantly due to population growth, technological, and economic development. The U.S. Department of Energy predicts that the average global energy consumption will grow by 50% by 2050 (1). Currently, a large portion of consumed energy is of fossil and non-renewable origin. In this context, the search for alternative and more efficient renewable energy sources has become a growing focus of scientific efforts.

The harnessing of lost energy in the form of heat could contribute as an alternative and renewable energy option, as approximately 66% of consumed energy is wasted through exhaust gases and cooling fluids (2). This low-grade waste heat could be reused by thermoelectric devices that directly convert heat into electricity (3). The significant advantages of thermoelectric devices include their robustness, absence of moving parts, silent operation, potential use of renewable energy sources, and no production of toxic gases. However, its contribution remains relatively modest compared to other sustainable sources due to the low efficiency of converting heat into electricity, limiting their use to applications where cost is not a limiting factor, such as power for space probes, remote energy sources for oil pipelines, and small devices like watches and calculators (4).

To expand the use of thermoelectric technology on a larger scale, it is essential to research and develop thermoelectric materials with higher efficiency. The low efficiency of current materials is the main obstacle to the widespread adoption of this technology. Additionally, most materials with considerable thermoelectric performance are composed of rare, costly, and toxic elements (5).

In this context, colloidal dispersions of charged nanoparticles (NPs) have recently gathered attention for thermoelectric applications, as both the NPs and the dispersing solvent can offer promising properties (6). The thermoelectric efficiency of these materials is primarily influenced by the thermodiffusion of the charged species. When exposed to a temperature gradient, the NPs in a colloidal dispersion migrate, leading to a concentration gradient of charged species, phenomenon known as the Soret effect.

Among these dispersions, the FFs which are composed of magnetic NPs stand out due to their thermodiffusive and their magnetic properties, which can be exploited to enhance the performance of thermoelectric devices. A study demonstrated that

incorporating iron oxide NPs into an aqueous dispersion improved thermoelectric efficiency by approximately 30% (7).

In addition to the role of NPs, the choice of solvent also plays a significant role in achieving high thermoelectric efficiency. Solvents with high thermal stability can enhance thermoelectric conversion (8,9). Among the potential candidates, ionic liquids (ILs) and propylene carbonate (PC) are noteworthy. ILs offer high conductivity due to their ionic composition but can present challenges due to their higher viscosity compared to traditional solvents. Among ILs, EMIM TFSI (1-Ethyl-3-methylimidazoliumbis(trifluoromethylsulfonyl)imide) is particularly promising for thermoelectric applications because of its high sensitivity to electric fields (10), excellent thermal stability, and lower viscosity compared to other ILs. On the other hand, PC with its high boiling point, low toxicity, and low flammability, offers significantly lower viscosity but lacks ionic properties. Therefore, in this work mixtures of EMIM TFSI and PC will be also studied aiming to achieve an optimal balance between viscosity and electrical conductivity, potentially enhancing performance.

Despite the expectation of promising results, research on dispersions of magnetic NPs in pure ILs and their mixtures with other solvents is still focused on evaluating the colloidal stability of these systems. Previous studies have demonstrated that stable colloidal dispersions of maghemite NPs (γ-Fe_2O_3) in pure ILs (11,12) and in mixtures of ILs with water (13) can be achieved by carefully controlling parameters such as the ionic composition of the liquids and the surface properties of the NPs. These studies have laid the groundwork for the present study, offering valuable insights into colloidal stability and providing experimental preparation protocols.

In this work, NPs consisting of a cobalt ferrite core and a maghemite-rich shell ($CoFe_2O_4$@γ-Fe_2O_3) will be studied. These NPs offer significantly higher magnetic anisotropy, which has the potential to enhance thermoelectric efficiency, as indicated by some modeling and simulation studies (14,15). Additionally, they benefit from the surface functionalization versatility and long-term chemical stability of maghemite, with a composition similar to that of previously studied NPs.

The overall objective of this work is to evaluate the influence of various parameters, including NP composition and size, the nature of the ligand used to modify the NP surface, pH, temperature, and aging on the colloidal stability of core@shell magnetic NPs dispersed in pure EMIM TFSI, PC, and their mixtures. Additionally, this study

investigates the effect of heating during NP surface functionalization to determine its impact on ligand adsorption and NP leaching.

This work is organized into six chapters. The first chapter offers an extensive literature review, establishing the foundational concepts necessary for understanding the work and exploring the current state of the art related to this field. This chapter not only introduces key theories and methodologies but also situates the study within the broader scientific context.

Chapter 2 is dedicated to a detailed description of the materials and methods used in the research providing discussion regarding the synthesis of the precursors samples, the characterization techniques employed throughout the study and the preparation of the samples for the analysis of several parameters, outlining the procedures and protocols.

The results of the study are presented in Chapters 3, 4 and 5. Each of these chapters is designed to address different aspects of the findings, breaking down the results into manageable sections to enhance understanding. Finally, Chapter 6 presents the conclusions drawn from the research, along with a discussion of future perspectives.

Chapter 1

This chapter provides a comprehensive literature review, beginning with an overview of thermoelectric materials, which sets the stage for understanding their relevance to the study. The review then explores the properties and applications of FFs, followed by a discussion on ILs, with a specific focus on EMIM TFSI. The chapter also explores PC as another key solvent for thermoelectric applications. Additionally, the chapter addresses NP interactions and colloidal stability, covering key concepts such as van der Waals interactions, repulsive forces from the electrical double layer (EDL), and DLVO theory. It further discusses the limitations of DLVO theory by introducing non-DLVO forces. The chapter concludes by examining NP colloidal stability in various environments, including ILs, PC, and solvent mixtures, laying a solid foundation for the following experimental work.

1. Literature review

1.1. Thermoelectric Materials

The induction of a temperature gradient ΔT in a conductor or semiconductor causes the diffusion of charge carriers from the hot region to the cold due to kinetic agitation, generating electrical potential. This phenomenon is named the Seebeck effect, in honor of its discoverer, Thomas Johann Seebeck, and is described by Equation 1.

$$V = -Se\Delta T \quad (1)$$

where V is the induced voltage, Se is the Seebeck coefficient and ΔT is the temperature gradient.

Figure 1 illustrates the Seebeck effect for a solid material, where the phenomenon was initially studied. In this system, holes in the hole-rich (p-type) material diffuse toward the electron-rich (n-type) material. In contrast, electrons in the electron-rich (n-type) material diffuse into the hole-rich (p-type) material, generating an electromotive force.

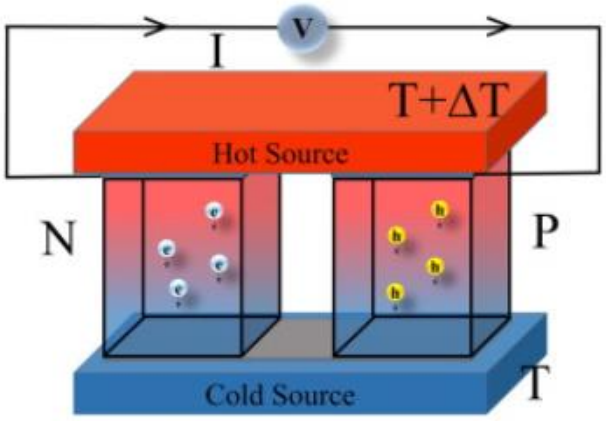

Figure 1. Seebeck Effect functioning. Reproduced from (16).

Despite being a sustainable technology with broad application possibilities, thermoelectricity has not been extensively employed due to the low efficiency of thermoelectric materials. The efficiency of converting thermal energy into electricity in a thermoelectric device is commonly expressed by the figure of merit ZT (Equation 2) (17).

$$ZT \propto \frac{S_e^2 \sigma T}{\kappa} \quad (2)$$

Where σ is the electrical conductivity, T is the absolute temperature and κ is the thermal conductivity.

Materials that began to exhibit more significant Seebeck coefficients were semiconductors with a small energy gap. However, even these materials show low ZT values, ranging from 0.1 to 1 (18). With the development of nanotechnology, Hicks and Dresselhaus (19) predicted a considerable increase in thermoelectric efficiency through the use of nanomaterials. At that time, there was a significant growth in the number of publications in the field of thermoelectric materials, as observed in the second rising region (II) of Figure 2.

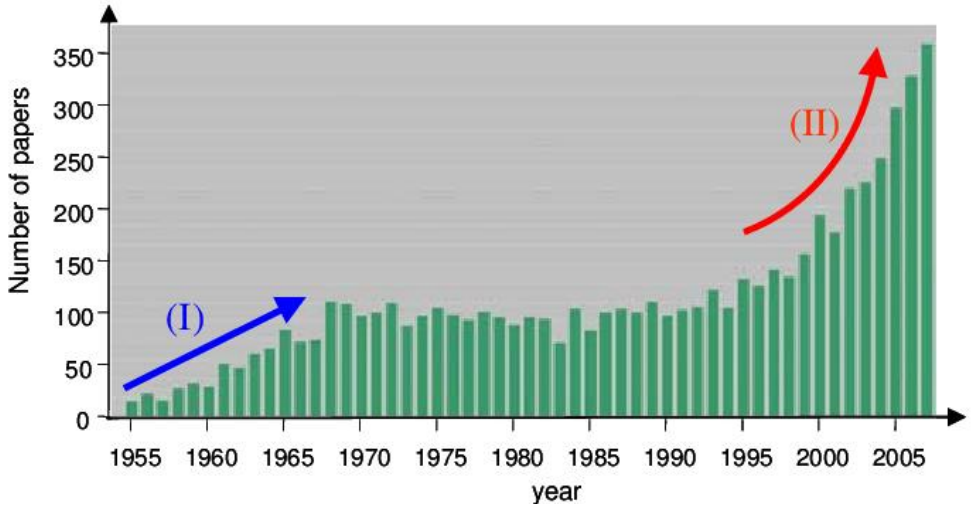

Figure 2. Number of articles published as a function of years for thermoelectric materials. Reproduced from (5).

In general terms, the increase in efficiency guaranteed by nanomaterials lies in the possibility of achieving lower thermal conductivity values for nanostructured materials, contributing to the increase in ZT. However, even with discoveries in the field, currently, most materials that exhibit good thermoelectric performance are composed of rare, costly, and toxic materials (5).

One potential solution explored to address these issues is the use of liquid-based thermo-electrochemical cells, or thermocells. These devices consist of a two-electrode system with an electrolyte that contains a redox couple connected to an external circuit (Figure 3) (20). In this setup, the temperature difference drives the redox reaction,

causing oxidation of the redox couple at the anode and reduction at the cathode. The flow of current in a thermocell remains continuous because the reduced species are transported through the electrolyte by convection, diffusion, and migration toward the anode, where they undergo oxidation. The oxidized species are then transported back to the cathode, sustaining a continuous reaction cycle. This phenomenon is called thermogalvanic effect.

The thermocell is highly versatile and capable of being manufactured in small diameters. It can be placed in polymeric or ceramic matrices, thanks to its flexibility and resistance to high temperatures. Additionally, it is cost-effective and scalable, making it a practical option for various applications (7).

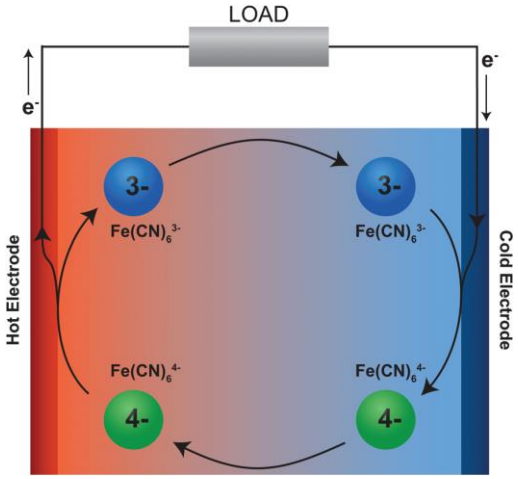

Figure 3. Mechanism of the liquid-based thermo-electrochemical cells, or thermocells. Reproduced from (3).

In addition to these advantages, incorporating complex fluids into thermocells, such as FFs, which are liquids containing magnetic NPs, can further enhance thermoelectric efficiency. A recent study demonstrated that the presence of oxide magnetic NPs improved energy conversion by up to 30% (7).

Figure 4 illustrates a thermocell with NPs dispersed in the electrolyte. In this system, besides the thermogalvanic effect, a phenomenon known as the thermoelectro-diffusion effect also occurs. This effect is closely related to the thermodiffusion of charged species, which is called the Soret effect, where a temperature gradient creates a concentration gradient of charged species between the electrodes, thereby enhancing thermoelectric efficiency (7). This phenomenon is represented by Equation 3, where η_i

is the concentration, ΔT is the temperature variation, and S_T is the Soret coefficient, which is proportional to the entropy transported by molecules or mobile particles in the system.

$$\frac{\Delta n_i}{n_i} = S_T \Delta T \tag{3}$$

Beyond the Soret effect, the magnetic characteristic of FFs allows for exploring the influence of inducing a magnetic field on the thermoelectric phenomenon. A 25% increase in the Seebeck coefficient was observed in a diluted FF based on maghemite NPs when a moderate magnetic field was applied to the system (21).

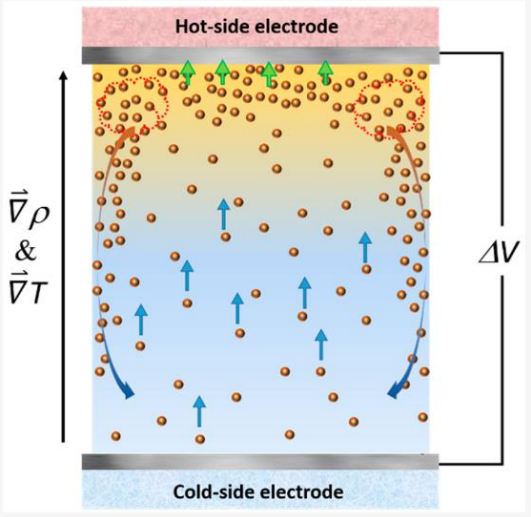

Figure 4. Thermocell with dispersed NPs. Reproduced from (22).

Research into the use of complex fluids for thermoelectric applications is still in its early stages and understanding the colloidal stability of these systems is crucial for developing usable materials. Consequently, the upcoming chapters will provide a detailed exploration of the key concepts needed to grasp the colloidal stability of the complex fluids under study, starting with a chapter on FFs.

1.2. Ferrofluids (FFs)

Before introducing the concept of FFs, it is important to provide a brief explanation of colloidal dispersions, which is a mixture composed of fine particles, typically ranging from 1 nm to 1 μm in size, distributed uniformly in a continuous medium, which can be

liquid, gas or solid. Colloidal dispersions are classified based on the physical phase of the dispersed particles and the medium. In a sol, solid particles are dispersed in a liquid (e.g., paints). Gels are semi-solid systems with a network structure (e.g., gelatin). Aerosols have particles dispersed in a gas, like smoke or fog. Emulsions involve liquid droplets in another liquid (e.g., milk), and foams are dispersions of gas bubbles in a liquid or solid (e.g., whipped cream).

These dispersions are generally stable over time, with particles not settling out of the medium rapidly. This colloidal stability is mostly attributed to factors like the Brownian motion and the electrostatic repulsion among the particles. The Brownian motion involves the random movement of colloidal particles as they collide with molecules of the dispersing medium.

Colloidal dispersions have a wide range of applications across various fields, including medicine, the food industry, cosmetics, and environmental remediation. In this study, however, a particular type of colloidal dispersion will be examined in detail, the FFs.

FFs are a specific type of colloidal dispersion, consisting of magnetic NPs suspended in a carrier liquid, that can be polar or nonpolar. The FFs were originally developed in the 1960s by NASA researcher Solomon Steve Papell, to control fluids through the application of a magnetic field in space under zero-gravity conditions. He prepared two stable colloidal dispersions of magnetite (Fe_3O_4) particles using oleic acid as surfactant and dispersing them in heptane and JP_4 (a common rocket and turbojet fuel) (23). This pioneering work laid the foundation for subsequent research and development in the field.

The possibility of controlling the viscosity of a fluid by applying a magnetic field opened the use of this material for many applications, such as in rotating shaft seals to prevent leakage in hard drives and other precision instruments (24), in targeted drug delivery, as contrast agents in magnetic resonance imaging, and in hyperthermia treatment for cancer (25). Additionally, it is employed in loudspeakers to dampen vibrations and improve sound quality (24), among other uses.

The NPs in FFs are composed of ferromagnetic or ferrimagnetic materials, including metals such as iron, cobalt, and nickel, as well as metal oxides like iron oxide and iron nitride. Substituted ferrites, such as manganese, nickel, and cobalt ferrites, are

also commonly used. These particles are single-domain superparamagnetic materials, typically ranging in size from 3 to 15 nm (26).

Superparamagnetism is a phenomenon where magnetization appears only in the presence of a magnetic field, with the magnetization direction capable of randomly flipping due to thermal effects. This behavior is specific to nanoscale ferromagnetic or ferrimagnetic particles. A key advantage of superparamagnetic materials is their lack of net magnetization in the absence of a magnetic field, which helps prevent significant magnetic aggregation.

The synthesis of FFs can be divided into two main methods: top-down and bottom-up. The first method involves breaking down bulk materials into smaller particles, typically through mechanical grinding and high-energy ball milling. This approach allows the production of uniformly dispersed fine particles. However, the main disadvantage is the very long time of preparation (27). On the other hand, the bottom-up method involves building particles atom by atom or molecule by molecule, using chemical synthesis techniques such as coprecipitation, sol-gel processes, or thermal decomposition. Each technique has its advantages and disadvantages. In this study, the coprecipitation method followed by a surface treatment was chosen, as it is one of the most widely used and straightforward methods (27). Additionally, our research group has extensive experience with this technique, further supporting its selection.

In this study, the FFs under investigation consist of core@shell bimagnetic NPs, featuring a cobalt ferrite ($CoFe_2O_4$) core surrounded by a thin maghemite (γ-Fe_2O_3) shell, as depicted in Figure 5. These NPs were selected due to the cobalt ferrite's high magnetic anisotropy, which has the potential to enhance thermoelectric efficiency, as indicated by modeling and simulation studies (14,15). Moreover, the maghemite shell offers long-term chemical stability and high surface tunability, with a similar composition used in previous research conducted by our group in this field (11,13,28).

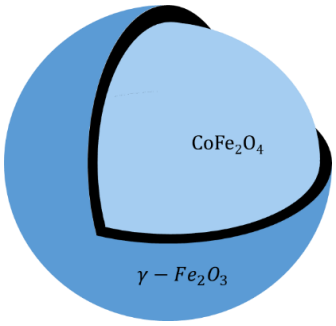

Figure 5. NPs core@shell structure.

Regarding the solvent used to disperse the particles, its right selection is crucial to achieving the desired properties of the FF. Beyond its role in the colloidal stabilization of magnetic NPs, the solvent may also offer specific advantages for certain applications. For instance, in thermoelectric applications, it is preferable to use solvents that can withstand high temperatures, have not too large viscosity, and exhibit high electrical conductivity. The following chapters will discuss the key characteristics of the solvents chosen to disperse the core-shell NPs in this work.

1.3. Ionic Liquids

ILs are supramolecular systems with low melting points and characteristics similar to an ionic system, typically consisting of organic cations and organic or inorganic anions. Among them are those with melting points below 100 °C, known as room-temperature ILs (29). These solvents offer several advantages that make them highly suitable for thermoelectric applications, including negligible vapor pressure, high thermal and electrochemical stability, high ionic conductivity, nonflammability, and good solubility (29–32).

A significant advantage of these solvents lies in the inherent synthetic flexibility of combining various cations with an expanding array of anions, enabling the precise tuning of their properties to suit a specific application. The most studied anion and cation molecular structures are shown in Figure 6. The imidazolium-based ILs are among the most extensively studied due to their exceptional properties, including a broad range of room temperature ILs, high conductivity, dispersive interactions that enhance solute dissolution, low melting points, and electrochemical stability (33).

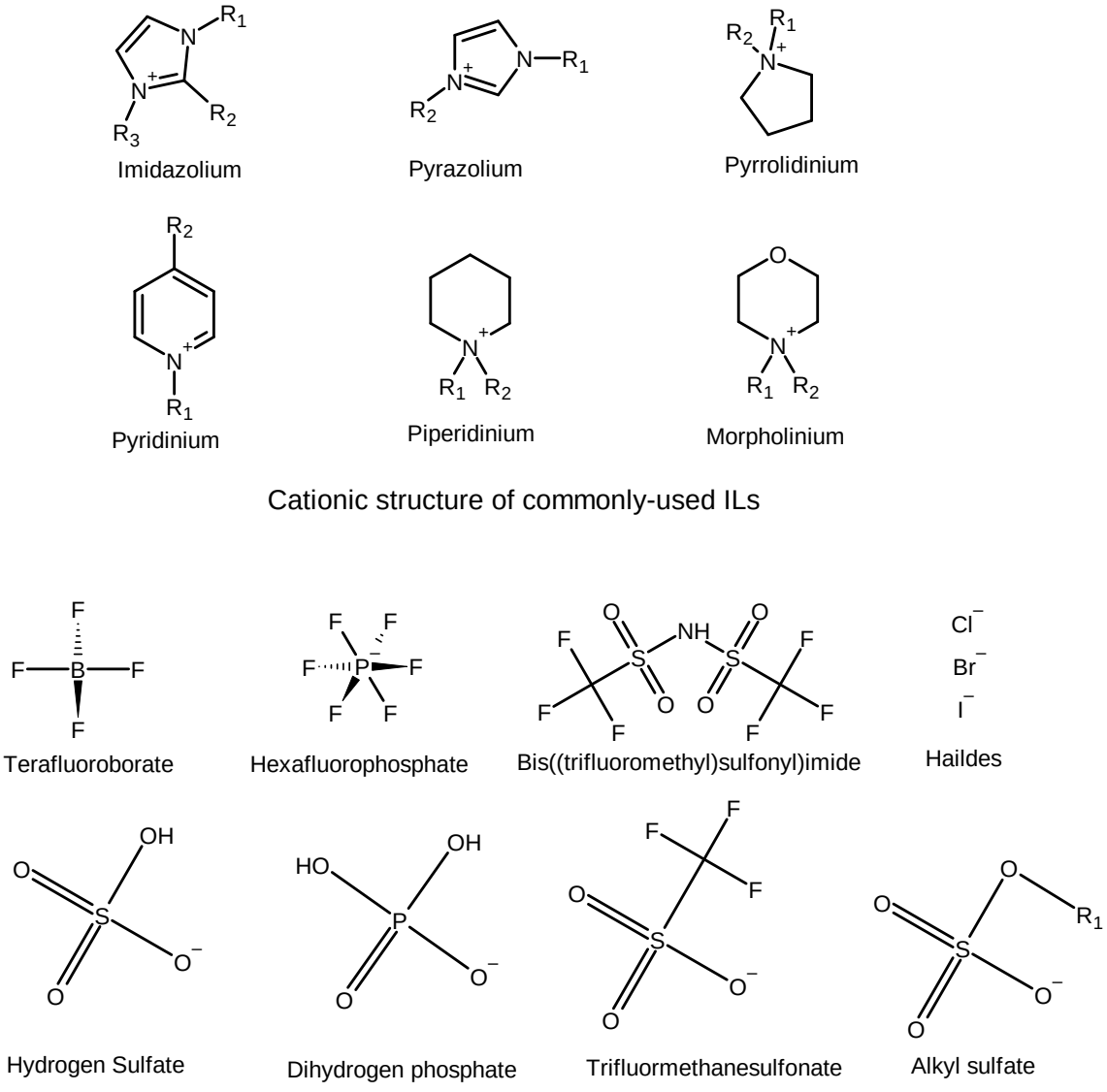

Figure 6. Commonly studied ILs cations and anions. Reproduced from (33).

In the context of colloidal stabilization, ILs serve as excellent dispersion media, allowing NPs to be stably dispersed even without surfactants or polymers. This characteristic can be generally explained by the interactions which come from their highly ionic nature. Typically, the ions in ILs are asymmetric with delocalized electrostatic charges. The combination of strong Coulombic forces and weaker directional interactions, such as hydrogen bonding, cation–π interactions, van der Waals forces, and dispersion interactions, can lead to the formation of nanoscale structures between the NPs and the ILs. These structures often include polar and nonpolar

domains, with solutes concentrating within the domains to which they have the greatest affinity (34).

One potential drawback of using ILs for energy conversion is their higher viscosity compared to molecular solvents (35). High viscosity can hinder mass transport, reducing energy conversion efficiency. However, ILs are highly miscible with polar substances, allowing them to be mixed with low-viscosity solvents that offer favorable properties for thermoelectric applications.

The ionic liquid selected for this study is 1-ethyl-3-methylimidazolium bis(trifluoromethylsulfonyl)imide, commonly known as EMIM TFSI, with synonyms including EMIM NTf2, EMIM BTI, EMIM BTA, C1C2Im TFSI, Im12 TFSI. Compared to other ILs, EMIM TFSI offers key properties for thermoelectric applications, such as high thermal stability, low viscosity (36) and strong sensitivity to electric Fields (10,36). Its molecular structure is shown in Figure 7.

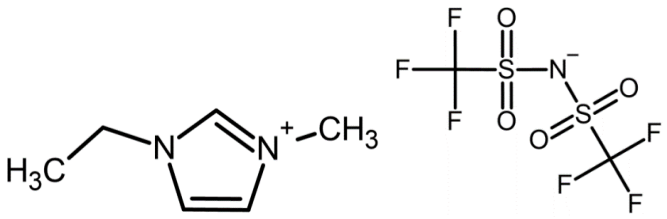

Figure 7. Molecular structure of EMIM TFSI.

The thermal stability of this ionic liquid can be attributed to the presence of the imidazolium ring in the cation, which is further reinforced by the methyl group at the C2 position within the ring, offering greater stability compared to other imidazolium-based ILs (33). Additionally, this stability is enhanced when the imidazolium cation is paired with anions such as $[TFSI]^-$, $[BF4]^-$, and $[PF6]^-$ (37,38).

The relatively low viscosity of this ionic liquid, compared to others, is primarily attributed to the short alkyl chains in the cation (39). Additionally, the flexible structure of the anion also plays a significant role in maintaining the low viscosity of the ionic liquid. For example, [BMIm]6cPFSI has a higher dynamic viscosity (239 mPa·s at 20 °C) than [BMIm]TFSI (62.3 mPa·s at 20 °C) due to the more rigid structure of the cyclic anion (40). Table 1 presents a compilation of the properties of EMIM TFSI.

Table 1. EMIM TFSI properties.

Property	Value	Reference
Molecular weight	391.30 g/mol	
Melting point/ freezing point	around -18 °C and -16 °C	(41)
Boiling point	no boiling point according to OECD103	(41)
Viscosity (at 25 °C)	0.03283 ± 0.0007 (Pa.s)	(42)
Density (at 25 °C)	1519.1 ± 1.1 (kg/m^3)	(43)
Vapour pressure (at 20 °C)	0,000000041 Pa	(41)
Refraction index (at 25 °C)	1.4334 ± 0.0012	(44)
Electrical conductivity (at 25 °C)	0.57 ± 0.011 (S/m)	(45)
Thermal conductivity (at 25 °C)	0.1319 ± 0.0012 (W/m/K)	(46)
Decomposition temperature	454 °C (TGA)	(41)

Although EMIM TFSI has a relatively low viscosity compared to other ILs, it remains higher than that of typical molecular solvents. To address this, an organic polar solvent will also be used in this study for NP dispersion, along with mixtures of this solvent and EMIM TFSI, to achieve more optimal dispersion conditions.

1.4. Organic polar solvents

Organic polar solvents are of interest for NP dispersion, with certain solvents showing strong potential for thermoelectric applications due to their high boiling point, low viscosity, and low toxicity.

Among these solvents, dimethyl sulfoxide (DMSO) is a highly polar, aprotic solvent that has gained attention due to its high capacity to dissolve many substances. This characteristic is attributed to a high dielectric constant of 46 (47). Additionally, it is classified as a green-grade solvent. For thermoelectric applications, DMSO's high boiling point of 189°C makes it ideal for high-temperature conditions. Numerous studies have investigated the dispersion of NPs in DMSO. The dispersion behavior of maghemite NPs, which share similar surface properties with those studied in this work, has been explored and will be discussed. An analysis of colloidal stability in polar organic solvents, such as DMSO, is provided in Section 1.6, offering valuable insights into the stabilization mechanisms of these systems.

Despite DMSO's promising properties for thermoelectric applications, we chose to evaluate propylene carbonate (PC) in this study due to its even more advantageous characteristics for such applications. PC exhibits a higher boiling point of 242°C and a dielectric constant of 64, which may improve the dissolution of other species in the dispersions. Additionally, PC is considered a green solvent due to its low flammability, volatility, and toxicity (48). For these reasons, PC was selected as the polar organic solvent for dispersing NPs, both in its pure form and in mixtures with EMIM TFSI. Table 2 presents the main properties of this solvent.

Table 2. PC properties

Property	Value	Reference
Molecular weight	102.09 g/mol	
Melting point	-48.8 °C	(49)
Boiling point	241.6 °C	(49)
Viscosity	0.002512 Pa.s	
Dielectric constant	64	
Density (at 25 °C)	1.2047 g/cu cm	(49)
Vapour pressure (at 25 °C)	0.045 mmHg	(50)
Refraction index (at 20 °C)	1.4189	(49)

Despite the good properties of this solvent, unlike ILs, which are composed solely of ions, PC is a non-ionic solvent formed by molecules as illustrated in Figure 8. Given this distinction, blending ILs with PC could provide an effective balance between viscosity and electrical conductivity. Hybrid electrolytes based on mixtures of ILs and PC have been developed to successfully replace traditional organic solvents in batteries and supercapacitors (51,52).

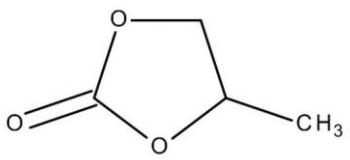

Figure 8. Molecular structure of PC.

Before delving into the colloidal stabilization of NPs in the selected solvents, it is essential to introduce key concepts regarding NP interactions, which will be covered in the following section.

1.5. Nanoparticles interactions and colloidal stability

One of the major challenges in NP dispersions lies in maintaining the colloidal stability of these systems. Considering the interplay between gravitational and viscous drag force and kinetic energy, very small particles take a long time to settle, and the NPs dispersions are considered stable. However, attractive forces between the NPs can result in agglomeration phenomena, leading to fluid-solid phase transitions. These forces must be offset by repulsive forces to keep the colloidal stability. Therefore, the fundamental forces at play in NP dispersions are discussed in this section, providing a basis for the discussions that follow.

1.5.1. Van der Waals interactions

Van der Waals (vdW) forces are a key source of attraction between NPs, influencing their behavior and stability in colloidal dispersions. These interactions are present in all particles regardless of material composition and are primarily due to polarization fluctuations that can destabilize colloidal dispersions, potentially leading to irreversible coagulation. More specifically, vdW or dispersion forces are defined by the interactions between all permanent and induced dipoles of the various colloids in the dispersions, averaged over the degrees of freedom of the polar solvent (53). These forces result from three components: the Keesom component, involving dipole-dipole interactions; the Debye component, corresponding to dipole-induced dipole interactions; and the dominant London component, which involves induced dipole-induced dipole interactions.

The vdW interactions between colloidal particles can be quantified using the Hamaker constant, which is influenced by the properties of the materials and the medium in which the particles are dispersed. The Hamaker constant is a complex function that depends on the frequency-dependent dielectric properties of all the media involved. The van der Waals interaction is determined by how the varying electric fields generated by one body interact with another.

Hamaker constant values for NPs are typically determined using either microscopic (London-Hamaker) or macroscopic (Lifshitz) approaches. In the case of the Lifshitz theory, *A* is derived using quantum-field theoretic techniques (54), and for two identical particles interacting within a medium, it can be calculated using Equation 4.

$$A \approx \frac{3}{4} K_B T \left(\frac{\varepsilon_1 - \varepsilon_2}{\varepsilon_1 + \varepsilon_2} \right)^2 + \frac{3h\upsilon_e}{16\sqrt{2}} \frac{\left(n_1^2 - n_2^2\right)^2}{\left(n_1^2 + n_2^2\right)^{3/2}} \quad (4)$$

where k_B is the Boltzmann constant, T is the temperature, ε_1 and ε_2 are the static dielectric constants of the particle material and the medium, respectively, h is the Planck's constant, υ_e is the characteristic frequency in the visible range and n_1 and n_2 are the refractive indices of the particle material and the medium, respectively. For iron oxide-based NPs, Hamaker constant values are of the order of 1×10^{-19} J (55).

This equation approximates the Hamaker constant by incorporating both the static dielectric properties and the optical properties of the interacting materials. According to this equation for similar particles dispersed in a medium, regardless of the values of the dielectric constants and refractive indices, the Hamaker constant will always be positive, indicating an attractive interaction, that must be balanced by repulsive forces to keep the stability of the dispersion. Hamaker estimated the vdW interaction energy between two spheres of diameters d_1 and d_2 neglecting retardation effects, as follows (56):

$$V_{vdW} = -\frac{A}{12} \cdot \left[\frac{d_1 d_2}{S \cdot (d_1 + d_2 + S)} + \frac{d_1 d_2}{(d_1 + S) \cdot (d_2 + S)} + 2 \ln \left(1 - \frac{d_1 d_2}{(d_1 + S) \cdot (d_2 + S)} \right) \right] \quad (5)$$

where S is surface-surface distance.

1.5.2. Repulsive interactions from the electrical double layer (EDL)

Electrostatic repulsion arises from the surface charges on NPs and the associated electrical double layer (EDL), which is formed when a particle with a surface charge is immersed in an electrolyte solution and ions of opposite charge (counter-ions) are attracted to the surface, while ions of the same charge (co-ions) are repelled.

The concept of the EDL has evolved significantly over time. The earliest explanation came from Hermann von Helmholtz in the 1850s, who proposed a model in which the charge on a solid surface is completely balanced by a layer of counterions

from the electrolyte, forming a simple capacitor-like structure. However, this model did not account for the thermal motion of ions.

Later, in the early 20th century, Louis Gouy and David Chapman expanded upon Helmholtz's model by introducing the concept of a diffuse layer, assuming a Poisson-Boltzmann distribution of the ions at a certain distance from the surface. In this model, the ions were considered non-interacting punctual charges. This led to the Gouy-Chapman model, which provided a more accurate description of the EDL. Despite its improvements, the Gouy-Chapman model had limitations, particularly in overestimating ion concentration near the surface.

In 1924, Oskar Stern advanced the model of the electric double layer by accounting for the finite size of ions, resulting in the Stern model, which integrates a compact layer of specifically adsorbed ions with the diffuse layer described by Gouy and Chapman. This combined model forms the basis of modern understanding of the electric double layer. Around the charged particle, two distinct regions are formed: the Stern layer and the diffuse layer, as shown in Figure 9. The Stern layer features a linear decay of potential as counter-ions are adsorbed onto the surface due to electrostatic attraction. In contrast, the diffuse layer extends outward where counter-ions and co-ions distribute according to electrostatic forces and thermal motion, resulting in an exponential decay of potential with distance from the surface.

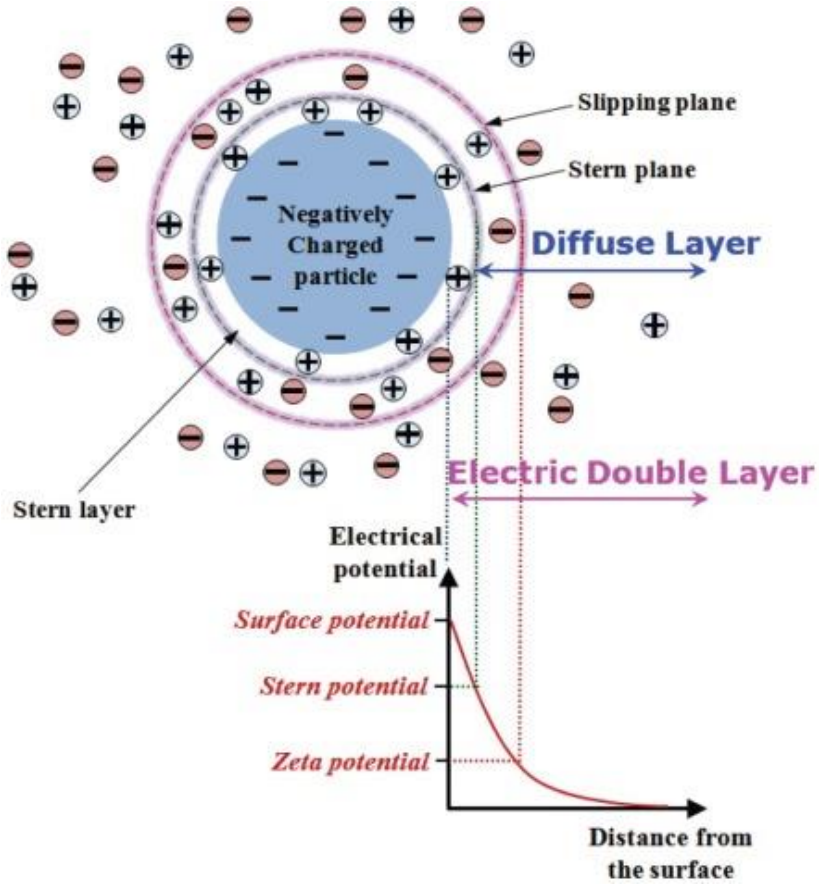

Figure 9. Electric Double Layer and corresponding electrical potential-distance curve. Reproduced from (57).

Moreover, in this model, there is the slipping plane, also known as the shear plane, which is an imaginary boundary within the electric double layer where the fluid's flow behavior changes relative to the particle surface influence. The potential corresponding to this plane is called zeta potential. It measures the magnitude of the electrostatic repulsion or attraction between particles in dispersion and reflects the surface charge density of the particles. A high zeta potential usually indicates strong repulsion between particles, leading to stable dispersion.

Another key concept related to the electric double layer is the Debye length, which defines the characteristic distance over which the electric potential decreases by a factor of 1/e from the surface, where e is the base of the natural logarithm (58). The Debye length represents the thickness of the diffuse layer, indicating the extent to which the surface charge influences the surrounding electrolyte solution. In systems with low ionic strength, the Debye length is longer, allowing the electric potential to extend further into the solution and resulting in a thicker diffuse layer. In contrast, in solutions

with high ionic strength, the Debye length is shorter, leading to a thinner diffuse layer and a more rapid decrease in electric potential.

Having explored the fundamental interactions such as van der Waals attractive forces and electric double layer repulsive forces, we can now turn our attention to the DLVO theory, which provides a first step for understanding the stability of colloidal systems. The DLVO theory integrates these two forces, combining the attractive van der Waals interactions with the repulsive electrostatic forces to explain how particles interact within a dispersion.

1.5.3. DLVO theory

The DLVO theory proposed by Derjaguin, Landau, Verwey, and Overbeek, states that the particles experience attractive van der Waals forces due to short-range unidirectional interactions between electrons in two neighboring molecules, and electrostatic repulsion from the overlap of electric double layers surrounding particles in a solution. The colloidal stability depends on the balance between these forces. If the repulsive forces dominate, particles remain dispersed, whereas if attractive forces prevail, particles aggregate.

The classical DLVO theory is typically introduced with the simplest scenario, where the total potential energy, V_T as two surfaces are brought closer together, is described as the sum of the van der Waals attractive potential V_{vDW} and the electric double layer repulsion potential V_{EL}, as presented in Equation 6.

$$V_T = V_{vdW} + V_{EL} \tag{6}$$

A general potential energy plot that qualitatively illustrates the key features of these interactions is shown in Figure 10. The van der Waals attraction decreases rapidly with separation distance, following an inverse power relationship. In contrast, the double-layer repulsion typically diminishes more gradually, often decreasing exponentially with distance. Consequently, van der Waals attraction tends to dominate at short separations, while double-layer repulsion becomes more significant at larger distances.

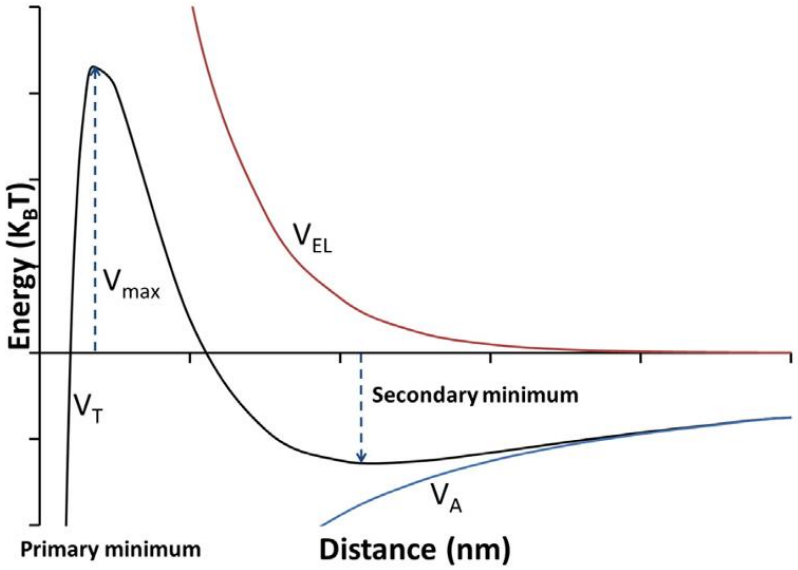

Figure 10. Energy-distance curve for the DLVO theory. Reproduced from (59).

The key aspect of this plot is the presence of a potential energy barrier at a distance roughly corresponding to the Debye length (60). A particle must have enough energy to overcome this barrier to reach the primary minimum, leading to irreversible particle aggregation. This potential barrier is crucial for maintaining stability in a colloidal system. In additon, the secondary minimum in the plot represents a weakly attractive interaction that can lead reversible aggregation of particles by thermal motion or slight perturbations.

While the DLVO theory provides a foundational understanding of the interactions between colloidal particles through the balance of van der Waals attraction and electric double layer electrostatic repulsion, this theory alone is insufficient to fully explain the behavior of many colloidal systems. To gain a more complete understanding, it is necessary to consider additional forces known as non-DLVO forces, including steric repulsion, attractive magnetic and solvation forces. These complementary concepts play a critical role in influencing colloidal stability, highlighting the need for an integrated approach that combines both DLVO and non-DLVO forces.

1.5.4. Steric repulsion forces

Among the non-DLVO forces, the steric repulsion is a stabilization mechanism achieved by adsorbing polymers or non-ionic surfactants onto the surface of NPs. The

long chains or the polymers or surfactants extend into the surrounding medium, creating an entropic barrier that prevents the close approach of the particles, as depicted in Figure 11. When two particles come close, the overlapping chains are compressed, leading to a repulsive force due to the unfavorable entropy reduction. The key advantage of steric stabilization is its ability to stabilize dispersions with high particle concentrations, a feat that electrostatic stabilization cannot achieve.

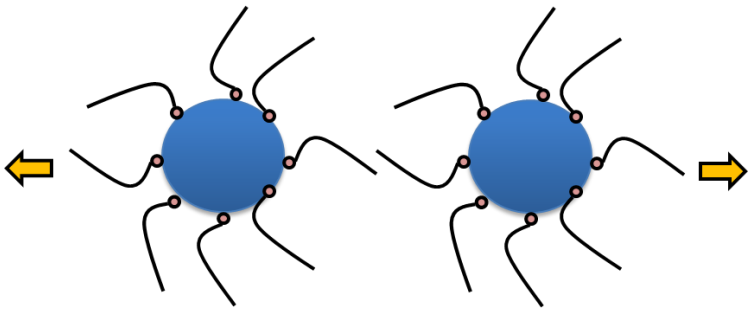

Figure 11. Steric repulsion mechanism.

The criterion for selecting a good steric stabilizer is that one segment of it should have an affinity for the suspended NP, allowing it to attach to the NP surface through adsorption, while the other segment should be compatible with the dispersion medium. For instance, the amphiphilic nature of surfactants makes them ideal for steric stabilization. The effectiveness of steric stabilization depends on the chain´s length and adsorption ability.

The steric stabilization is considered a thermodynamic stabilization method, where the total interaction potential is expressed as the total Gibbs free energy of the system (G_T), described by Equation 7 (61).

$$G_T = G_A + G_{ST} = G_A + G_{OS} + G_{VR} \tag{7}$$

The equation includes the contributions from attraction (G_A), steric repulsion (G_{ST}), osmotic repulsion (G_{OS}), and volume restraint interaction (G_{VR}).

The term G_{OS} corresponds to the increase in osmotic pressure that occurs when the polymer layers surrounding NPs overlap due to the increase in the concentration of solvated polymer tails near the interaction zone. This overlap causes solvent molecules to migrate into the overlapping region, creating a strong repulsive force that prevents NPs from agglomerating.

Concerning the term G_{VR}, volume restraint interaction occurs when the overlapping and compression of polymer chains reduce the volume of interacting polymers, resulting in a decrease in entropy. G_{VR} is always positive, indicating that it is favorable for repulsion. The steric stabilization can be achieved when $G_T>0$, which indicates that the choice of stabilizer and solvent needs to ensure that $G_{OS} + G_{vr} > G_{A.}$

1.5.5. Magnetic interactions

In addition to the attractive van der Waals forces, the dipolar interactions must be considered in FFs due to the magnetic nature of the NPs. For larger particles, magnetic forces are much weaker than electrostatic forces. However, as the particle size decreases to the nanoscale, these interactions become much more significant. This is because NPs are single-domain magnets, with permanent magnetic dipoles always magnetized to saturation magnetization, possessing a magnetic moment as described in Equation 8.

$$\mu_i = m_s \times V_i \tag{8}$$

where m_s is the volumetric magnetization of the material and V_i is the volume of the NP.

The interaction between two magnets dipoles μ_1 and μ_2 separated by the vector **r** is given by Equation 9.

$$V_{mag} = \frac{\mu_o}{4\pi r^3}\left[\mu_1 \cdot \mu_2 - \frac{3}{r^2}(\mu_1 \cdot \mathbf{r})(\mu_2 \cdot \mathbf{r})\right] \tag{9}$$

where μ_o is the magnetic permeability in the vacuum.

As shown in the equations, the magnetic moment depends on the NP volume, indicating that the effect of attractive magnetic forces is expected to be more pronounced for larger NPs.

The magnetic interaction forces between particles in dispersed systems lead to anisotropic interactions that strongly depend on the volume fraction of magnetic material and NP size (62). The anisotropic dipolar interaction energy between two magnetic particles, each carrying a magnetic moment separated by the vector **r**, can also be described by (Equation 10) (63):

$$\frac{V_{mag}(r,\theta_1,\theta_2)}{k_B T} = -X(2\cos\theta_1\cos\theta_2 - \sin\theta_1\sin\theta_2) \tag{10}$$

where

$$X(r) = \frac{1}{k_B T} \frac{\mu_0}{4\pi} \frac{\mu_1 \mu_2}{r^3} \tag{11}$$

The dimensionless parameter *X(r)* characterizes the intensity of the magnetic coupling. The orientations of the two dipoles are defined in Figure 12, where θ_i is the angle between the dipoles and **r**. The normalized potential energy $V_{mag} / k_B T$, at a fixed distance between the dipoles, depends on their orientation and fluctuates between −2X and +2X as the dipoles rotate. The maximum attraction of −2X occurs when the dipoles are aligned in the same direction, which can be achieved by applying an external magnetic field.

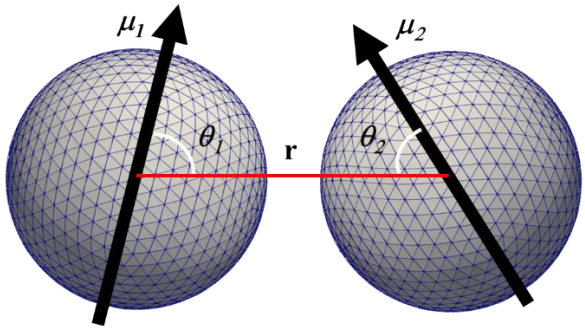

Figure 12. Representation of magnetic moments and their relative orientations.

In the case of weak magnetic coupling ($X(r) \ll 1$) typical of dilute systems where the distance between dipoles is large, the thermal energy $k_B T$ dominates over the dipolar interaction energy, allowing the dipoles to rotate freely. The magnetic interaction energy can then be calculated using the Potential Distribution Theorem (64), which averages over the orientation angles of the dipoles. Under these conditions, the potential decays with r^6 and can be expressed as follows (Equation 12) (64):

$$\frac{V_{mag}}{k_B T} = -\frac{X^2}{3} = -\frac{1}{3} \frac{(k_B T)^2 \mu_0^2}{16\pi^2} \frac{(\mu_1 \mu_2)^2}{r^6} \tag{12}$$

For two identical dipoles whose moments are $\mu = m_S V$ (where m_S is the saturation magnetization and V is the volume of the particle, assumed to be spherical), the latter equation can be rewritten as (Equation 13):

$$\frac{V_{mag}}{k_B T} = -\frac{\gamma_0^2}{48\pi^2} \quad (13)$$

whose parameter γ_0 represents the magnetic coupling term, equal to $4\pi X(r)$.

Conversely, for a strong magnetic coupling ($X(r) >> 1$), where large magnetic moments ate separated by short distances, the normalized potential decays with r^3 and writes (Equation 14):

$$\frac{V_{mag}}{k_B T} = -2X = -\frac{\gamma_0}{2\pi} \quad (14)$$

1.5.6. Solvation forces

Solvation forces are non-DLVO interactions that arise when solvent molecules are confined between two surfaces, leading to their organization into distinct layers, as shown in Figure 13. These are short-range interactions, where molecular layering generates an oscillatory effect. The strength of this effect depends on the properties of the solvent molecules and the characteristics of the surfaces, such as whether they are hydrophilic or hydrophobic, smooth or rough, crystalline or amorphous, homogeneous or heterogeneous, natural or patterned, rigid or fluid-like (65).

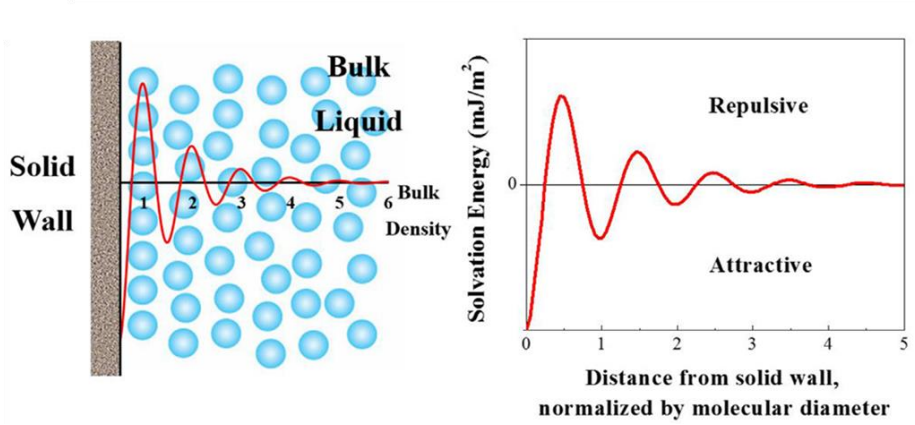

Figure 13. Solvent molecule layering and the corresponding solvation energy-distance curve. Reproduced from (66).

Solvation forces are system-dependent and challenging to interpret, as they are strongly influenced by the arrangement and interactions of molecules at the surface. In the case of ILs, which will be discussed in more detail in the next section, the layering

effect of ionic species plays a crucial role in ionic-liquid-based dispersions and significantly impacts the colloidal stability of these systems.

1.6. Nanoscale interactions between colloidal nanoparticles in different solvent compositions

1.6.1. Ionic Liquids

Traditional mathematical models used to understand colloidal behavior are commonly based on the Poisson-Boltzmann interpretation of the double electrical layer concept. However, this theory has qualitative and quantitative limitations for ionic liquid-based dispersions.

Most studies on NP dispersions in ILs focus on analyzing a specific type of ionic liquid, which may hinder the application of correlations obtained for different systems. Zhang *et al.* (67) examined colloidal dispersions of NPs in molten salts, which are inorganic liquids analogous to ILs. According to results obtained using molecular dynamics and simulations, solvent structuring at the solid-liquid interface occurred in these systems, regardless of the surface-solvent interaction. The authors concluded that the repulsive force due to the formation of ion layers far exceeds the contributions of the van der Waals and electrostatic forces of the double electrical layer, and the ionic structure near the solid-liquid interface is responsible for colloidal stability, as shown in Figure 14 (67).

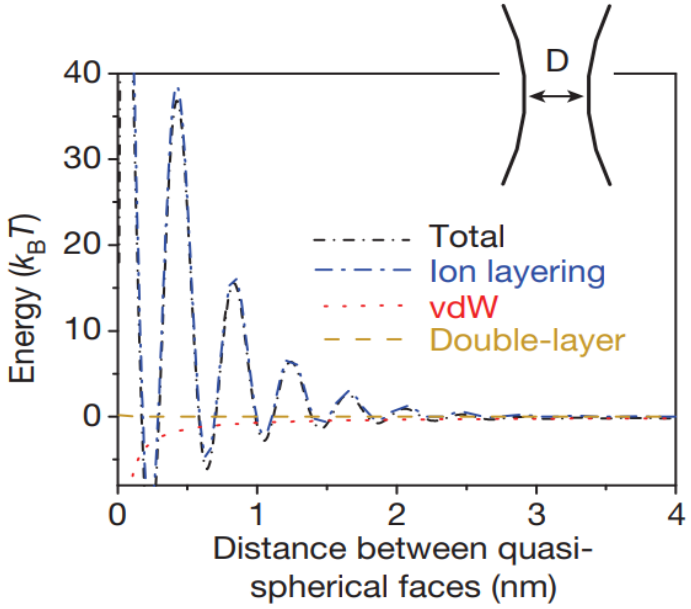

Figure 14. Energy-distance curve from interactions simulations between NPs dispersed in molten salts. Reproduced from (67).

Studies related to the structure formed at the ionic solid-liquid interface have shown that in the case of uncharged surfaces, counter-ions and co-ions are equally distributed. However, an increase in surface charge density leads to the formation of a multilayered structure, with the first layer rich in counter-ions and the second containing more co-ions than counter-ions. This alternating enrichment of co-ions and counter-ions, as shown in Figure 15 (a), can extend across several layers (a phenomenon known as overscreening). With a further increase in charge density, a monolayer of counter-ions that completely compensates the surface charge is formed. Finally, with even higher charge density, the presence of more than one layer of counter-ions at the interface is observed, as depicted in Figure 15 (b) (crowding phenomenon) (68).

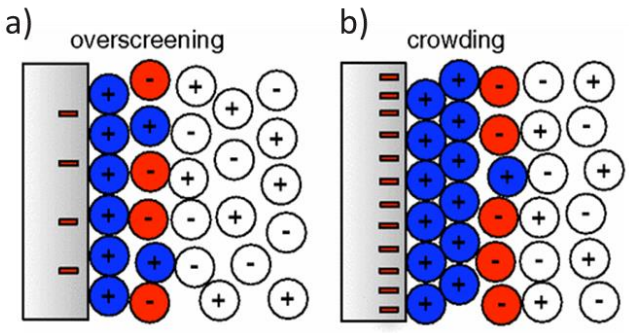

Figure 15. Mechanism structuring at the solid-ionic liquid interface. Reproduced from (68).

A quantitative analysis of ion structuring at the ionic solid-liquid interface was developed by Ivanistsev *et al.* (69). The authors describe the transitions of different layers through the dimensionless parameter for surface charge compensation (κ_{ion}) (Equation 15).

$$\kappa_{ion} = \frac{\sigma}{\theta_{ion}^{max}} \tag{15}$$

where σ is the surface charge density of the solid and θ_{ion}^{max} is the charge density of a densely packed monolayer of counter-ions, which depends solely on the charge and geometric parameters of the counter-ion.

In the case of $\kappa_{ion} = 0$, the ionic liquid organizes in the plane of the solid surface but not perpendicular to it. The layer surrounding the surface will have distributed anions and cations. An increase in charge, while $\kappa_{ion} < 1$, characterizes the formation of the overscreening regime, in which multilayers with alternating charges perpendicular to the surface occur, with the maximum number of layers when $\kappa_{ion} = 0.5$. When $\kappa_{ion} = 1$, a monolayer of counter-ions is formed and completely compensates the surface charge. Finally, for $\kappa_{ion} > 1$, the crowding phenomenon occurs. In Figure 16, a schematic diagram of the transition regimes of layer formation according to κ_{ion} is presented.

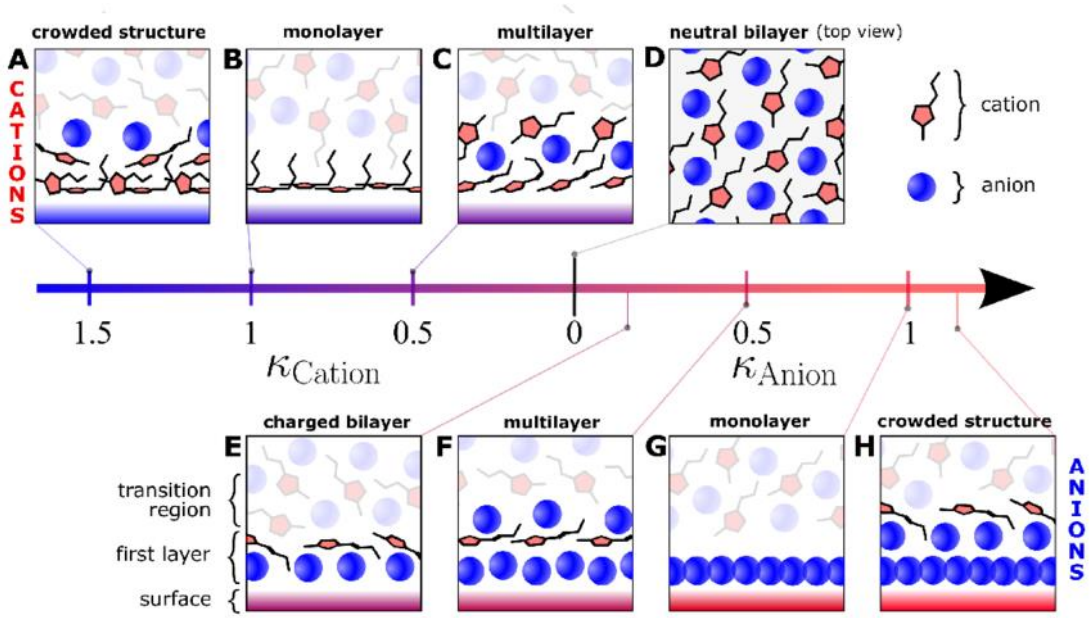

Figure 16. Ions structuring at the solid-ionic liquid interface. Reproduced from (70).

It is worth noting that this model should be used as a way to rationalize general trends for real systems, as this analysis does not encompass factors such as the presence of more than one type of counter-ion or a solvent different from the ionic liquid, or if the solid surface has a geometry different from a flat surface.

Riedl *et al.* studied dispersion routes of maghemite NPs in various types of ILs to determine essential parameters for colloidal stability (11). The emphasized factors included the nature of the ionic liquid's cations and anions, particle surface charge, pre-existing counter-ions, and the method of transferring NPs to ILs. Three types of NP surfaces with different structural charges were investigated: non-functionalized NPs (hydroxide groups on the surface), citrate-functionalized particles, and NPs coated with polymer (polyacrylate or polyacrylate co-maleate). Regarding the nature of the counter-ions, the following species were evaluated: Li^+, Na^+, NH_4^+, TBA^+, and $BMIM^+$ for anionic NPs and NO_3^-, ClO_4^-, $C_6H_5O_3S^-$, $TFSI^-$, and $SMIM^{\pm}TFSI^-$ for cationic NPs. Furthermore, the effect of the molecular solvent present before transferring NPs to the ionic liquid was tested using water or DMSO. Colloidal dispersions were analyzed at different length scales and over time.

In this work, after transferring NPs from the molecular solvent to the ionic liquid, some counter-ions previously condensed on the NP surface may remain or may be exchanged with ions from the ionic liquid. Additionally, intermediate situations can

occur. According to the results, the authors concluded that some previously condensed counter-ions remain near the solid-liquid interface. They are responsible for generating a specific organization of the ionic liquid, which interferes with interparticle interactions and consequently influences the formation of multilayers that enable colloidal stability. The influence of counter-ions may be due to their interactions with the ions of the ionic liquid or with water, and their relative size compared to the cations and anions of the ionic liquid, as well as their affinity/interaction for/with the solid surface.

Using the formalism presented by Bazant *et al.* (68) as a basis and considering factors such as the presence of counter-ions of different species, the authors evaluated the influence of NP surface charge and counter-ions from the ionic liquid. They concluded that if the surface charge density of the NPs is zero before transfer to the ionic liquid, no dispersion occurs in any type of ionic liquid. Moreover, if the surface charge density of the NP is moderate (16 and 32 $\mu C\ cm^{-2}$), the κ_{ion} parameter is between 0 and 1, with the formation of ionic liquid multilayers influenced by the nature of the previously present counter-ion. Counter-ions significantly smaller (Na^+, Li^+) or larger than the ions of the ionic liquid used disrupt multilayer formation at the NP/ionic liquid interface. Finally, if the surface charge density is very large (200 - 300 $\mu C\ cm^{-2}$), the κ_{ion} has a value greater than 1, corresponding to the crowding regime, which does not allow stabilization in any case. In Figure 17, a schematic diagram summarizing the authors' conclusions is presented.

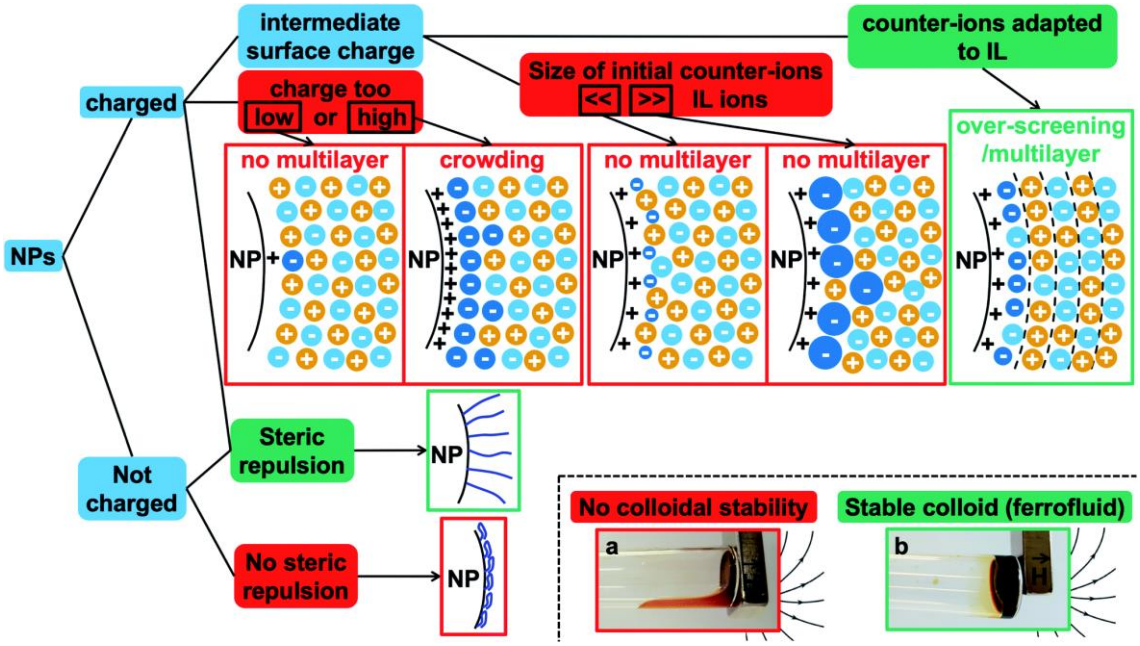

Figure 17. Different possibilities of ionic liquid structuring around charged and non-charged NPs (11).

Very recently, K. Bernardino (71) has used molecular dynamics simulations to investigate the long-range ordering in concentrated dispersions with several NPs dispersed in two types of ILs: 1-butyl-3-methyl-imidazolium tetrafluoroborate ([BMIM][BF_4]) and 1-octyl-3-methyl-imidazolium tetrafluoroborate ([OMIM][BF_4]). The results point out that the segregation between polar and apolar domains in ILs creates multiple activation barriers that prevent NP aggregation. These barriers, which can exceed 60 kJ/mol, provide kinetic stability to colloidal dispersions without additives, as shown in Figure 18. The distance between barriers depends on the size of the domains in the liquid, influenced by the alkyl group of the cation, while barrier height depends on NP properties and their interaction with the liquid.

The authors have also shown that NPs inducing stronger organization of the ions on their surfaces form more structured layers, leading to higher barriers and stronger dispersion stability. However, strong interactions between solvent ions and NPs do not always ensure better stability due to competition between the solvation of particles and ionic interactions within the solvent. These barriers not only stabilize dispersions but also slow NP dynamics, potentially leading to gel formation. The induced long-range NP organization can serve as a template for synthesizing complex materials, with nanocrystals dispersed in a matrix, controlled by domain segregation in the solvent.

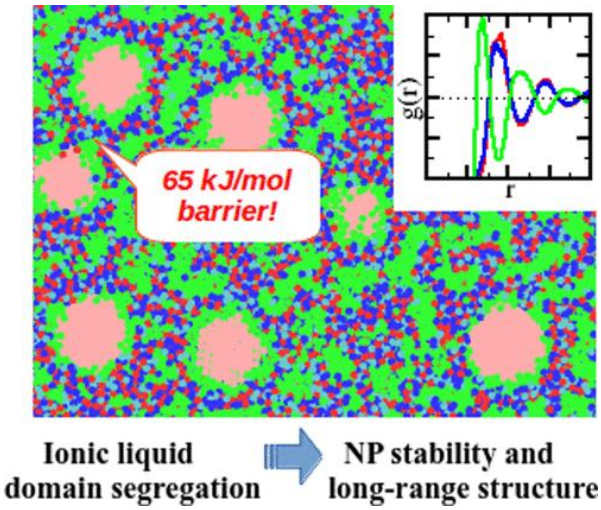

Figure 18. Snapshots of molecular dynamics simulations illustrating how domain segregation in ILs can stabilize NPs with high barrier energies (71).

As previously mentioned, the high viscosity of ILs can pose challenges for thermoelectric applications. To address this, the organic polar solvent PC is also utilized in this work for NP dispersion, as it exhibits highly favorable properties for such applications. Therefore, the following section will discuss the colloidal stability of FFs dispersed in organic polar solvents.

1.6.2. Organic Polar solvents

In polar organic solvents such as DMSO and PC, the mechanism of colloidal stabilization primarily involves electrostatic interactions. These solvents, with their high dielectric constants, enhance the solvation of NPs, promoting dispersion. Therefore, several studies have used DMSO as a stabilizing medium for various types of NPs with diverse surface functionalizations (72–76).

Studies with maghemite NPs, which have similar surface to the NPs studied in this work, have shown that in DMSO-based dispersions, colloidal stability is influenced by several factors, including the surface and effective charge of the NPs, as well as the arrangement of the solvent and counterions around them. The research confirms that electrostatic interactions are the primary factor, as DMSO's high dielectric constant enhances NP solvation. However, stabilization is more challenging than in water due to DMSO's lower dielectric constant compared to water, which leads to increased counterion condensation on NP surfaces, reducing their effective charge and resulting in

a shorter range of repulsive interactions. Nonetheless, electrostatic repulsion remains a significant stabilizing force in DMSO-based dispersions (62,77)

An interesting result was observed in a study on the colloidal stability of cobalt-based NPs sterically stabilized with a phthalocyanine macrocycle containing an amine group. When dispersed in ethanol, the NPs formed interconnected, pearl necklace-like structures due to magnetic dipolar attraction. However, in DMSO, the chain-like structures broke down, resulting in a dispersion of uniformly distributed spherical NPs (73).

With respect to PC, numerous studies have employed this solvent to achieve stable dispersions of various NPs for a wide range of applications (48,78–80). However, to date, there is no available literature on the colloidal stability of NPs similar to those investigated in this work. This gap highlights the importance of studying these dispersions, particularly as PC possesses even more attractive properties for thermoelectric applications than DMSO.

1.6.3. Mixtures of solvents

Another approach to selecting a solvent is to use solvent mixtures, allowing for the modulation of interactions between the NPs and the solvent. This strategy can lead to the development of a solvent with exceptional properties tailored for a specific application.

In mixtures of ILs with other solvents, most studies report colloidal aggregation, as seen in mixtures of hydrophilic ILs with water (81–84) or hydrophobic ILs with water (84). Fiuza *et al.* conducted a study on the dispersion of iron oxide NPs in ethylammonium nitrate (EAN)-water mixtures, demonstrating that these mixtures effectively stabilize NPs across a range of compositions and temperatures (13). The NPs are well dispersed due to sufficient repulsion facilitated by the solvent's organization at the interface. In this system a transition from hydrophilic to hydrophobic surface properties occurs around a 50% water to 50% EAN ratio.

In mixtures containing ILs, a critical factor is the intermediate salt concentration. When only a small amount of salt is present, the system is well-known and thoroughly studied. On the opposite end, where only ionic liquid is present, it is understood that the layering process plays a crucial role in stabilization. In the intermediate state, it is typically expected that adding salt would induce flocculation. However, in the case of

ILs, the large size of the ions challenges this assumption. In these systems, a solvation contribution, akin to a steric effect, can, in some cases, maintain stability. The main challenge in these systems is achieving surface organization at high salt concentrations.

Mixtures of DMSO and water were investigated to study the thermodiffusive properties of dispersions of hydroxyl-coated maghemite (γ–Fe_2O_3) NP (77). The study found that at low water fractions, the NPs exhibit thermophobic behavior, whereas at higher water fractions, they become thermophilic. The authors concluded that adjusting the ratio of DMSO to water could effectively tune the thermodiffusion properties, which is particularly useful for thermocell applications. On a molecular level, even the addition of a few DMSO molecules to water causes significant changes due to the strong hydrogen bonding interactions between the solvents (85).

Few studies have explored solvent mixtures for NP dispersions, but the potential for tuning their properties is significant. In this work, we aim to investigate the interactions in mixtures of two promising solvents: PC and the ionic liquid EMIM TFSI.

Chapter 2

This section will be divided into three main subsections: the synthesis of the precursor water-based FFs, the characterization techniques and equipment, which will include explanations of the methods used and the conditions for each measurement, and the sample preparation, where the production procedures for the various samples will be detailed.

2. Materials and methods

2.1. Synthesis of the precursor water-based ferrofluids

Three samples of FFs consisting of core@shell NPs ($CoFe_2O_4$@γ-Fe_2O_3) with different mean sizes dispersed in water were synthesized by coprecipitation in an alkaline medium, following the well-established method developed by Tourinho *et al*. (86,87). The syntheses were carried out at the Complex Fluids Laboratory of the Institute of Physics at UnB (LFC-UnB).

Bases with different strengths were used in each synthesis to obtain NPs with distinct mean sizes. As a general trend, the stronger the base, the greater the average NP size will be, keeping constant the other synthesis parameters. Higher pH values favor the hydrolysis of metal ion aquocations, increasing the efficiency of inorganic olation and oxolation polymerization reactions and, consequently, promoting crystalline growth.

The synthesized FFs samples were named APCo1, APCo2, and APCo3. For APCo1 and APCo2, solutions of 0.5 mol/L of $FeCl_2$ and $Co(NO_3)_2$ in a 2:1 ratio at room temperature were first mixed and heated to boiling temperature under constant stirring. Subsequently, the alkaline solution was quickly added, using ammonium hydroxide (NH_4OH) for APCo1 and methylamine (CH_3NH_2) for APCo2, as shown in Figure 19 – A. Regarding APCo3, solutions of $FeCl_2$ and $Co(NO_3)_2$ were previously heated to a warm temperature and rapidly added to the NaOH solution that was previously heated to boiling temperature under constant stirring, according to Figure 19 - B.

The coprecipitation process for the three syntheses is described by Equation 16, where the precipitated product corresponds to the core of cobalt ferrite.

$$Co^{+2}_{(aq)} + 2Fe^{+3}_{(aq)} + 8OH^{-}_{(aq)} \rightleftharpoons CoFe_2O_4 \downarrow + 4H_2O \qquad (16)$$

Following the coprecipitation step, the NPs were successively washed with ultrapure water to purify the samples from undesirable salts. Subsequently, the samples were treated with HNO_3 to remove byproducts and to slightly reduce the polydispersity of the NPs.

After washing and removing the supernatant, a solution of 0.5 mol/L of $Fe(NO_3)_3$ was slowly added to treat the surface of the cobalt ferrite NPs to make them stable at acidic pH. The system was boiled for 15 minutes and the expected result from

this step was the formation of an outer layer of maghemite (γ-Fe_2O_3). The excess of ferric nitrate was removed and successive washes with acetone were performed to control the ionic strength. Finally, acetone was removed and water was added to disperse the NPs.

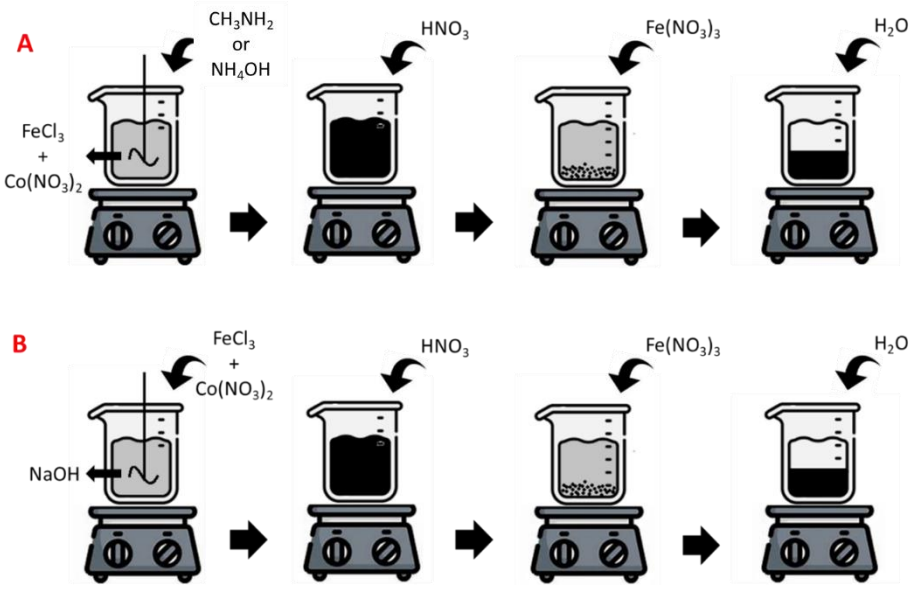

Figure 19. Water-based FFs synthesis.

Regarding the colloidal stability of the synthesized FFs, the NPs were stably dispersed mostly due to the repulsive forces induced by the electrostatic interactions. After synthesis, the FF's pH is around 2, which favors the presence of positively charged sites on the surface of the NPs. This phenomenon can be explained by the hydrolysis reactions that take place at the surface sites of the NPs occupied by transition metal ions (M), as presented in Equations 17 and 18.

$$\equiv MOH_2^+ + H_2O \rightleftharpoons \equiv MOH + H_3O^+_{(aq)} \quad (17)$$

$$\equiv MOH + H_2O \rightleftharpoons \equiv MO^- + H_3O^+_{(aq)} \quad (18)$$

In strongly acidic environments, most sites are positively charged, as shown in Figure 20 (a). In this case, the high density of positive surface charge ensures the stability of the FF. In pH values close to neutrality, the sites are mostly amphiphilic (Figure 20 (b)), and the low charge density may cause sample flocculation. Strongly basic environments also ensure the stability of FFs due to the high density of negatively charged surface sites (Figure 20 (c)).

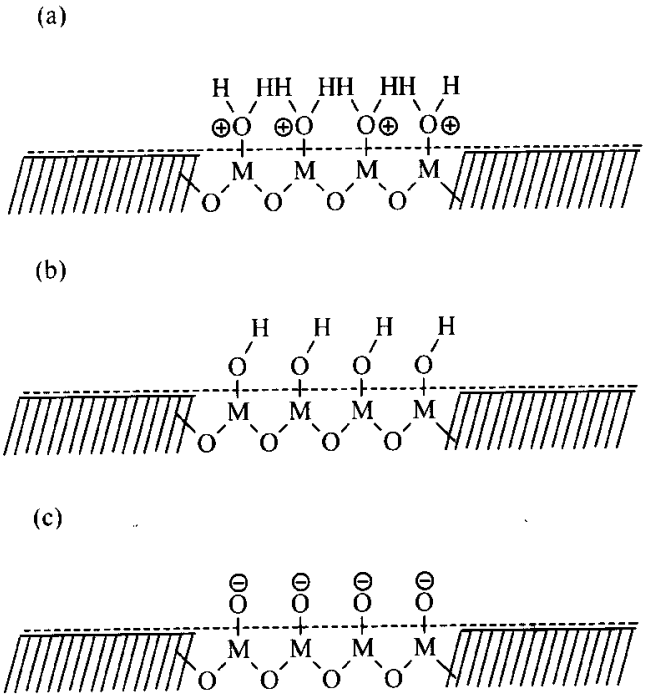

Figure 20. Influence of the pH in the charge of the NPs surface sites. Reproduced from (88).

2.2. Characterization techniques and equipment

This section will present the techniques used to characterize the synthesized FFs and the samples produced for the colloidal stability studies. Each discussed technique will include a brief explanation of its functioning, along with the presentation of the experimental conditions.

2.2.1. X-ray Diffraction (XRD)

An XRD experiment primarily provides information about their crystal structure and average crystallite size. In this technique, the sample is exposed to X-rays, which are diffracted by the orderly arrangement of atoms in the crystal lattice. The resulting diffraction pattern, with distinct peaks, is analyzed to determine the material's atomic structure, including lattice parameters and crystal orientation.

The crystal structure of the NPs was characterized by XRD measurements performed in a Bruker D8 Focus diffractometer, operated at 40 kV/30 mA with Cu-Kα radiation (λ = 0.1541 nm) in a 2θ range from 20° to 80°, with a scanning step of 0.05°

and a scanning rate of 0.1° min^{-1}. The measurements were performed at the Institute of Chemistry at UnB.

In addition to the characterization of the crystalline structure of the material, the XRD technique allows the calculation of the average particle diameter using the Scherrer Equation (Equation 19).

$$d_{rx} = \frac{\kappa\lambda}{\beta\cos\theta} \tag{19}$$

where d_{rx} is the average particle diameter, κ is a constant related to the form of the NP (0.94 for spheres), λ is the X-ray wavelength, β is line broadening at half the maximum intensity and θ is the Bragg angle.

2.2.2. Transmission Electron Microscopy (TEM)

TEM images provide information about the size and shape of the NPs. In TEM, a high-energy electron beam passes through an ultra-thin sample. As electrons interact with the sample, they are scattered or absorbed to varying degrees based on the density and composition of the sample. These interactions create detailed images that are captured on a screen or detector.

The morphology and size distribution of the NPs were obtained through TEM images. The microscope used was of the brand JEOL, model JEM-2100 with an acceleration voltage of 200 kV, located at the Multi-User High-Resolution Microscopy Laboratory (LabMic) at the University of Goiás.

The *ImageJ* software was employed to analyze the micrographs and to obtain the diameter of several NPs, aiming to determine the size distribution. A size histogram was fitted to the log-normal function, given by Equation 20, using the *Origin* software.

$$P(d) = \frac{1}{\sqrt{2\pi\sigma d}}\exp\left[-\frac{1}{(2\sigma^2)}\left(\ln\frac{d}{d_0}\right)^2\right] \tag{20}$$

where d_0 is the characteristic diameter and σ is the characteristic width of the polydispersity related to the distribution.

2.2.3. Flame Atomic Absorption Spectroscopy (FAAS)

FAAS is an analytical technique used to determine the composition of a sample by measuring the concentration of specific metal ions. In FAAS, a sample solution is aspirated into a flame, where it is atomized, creating free atoms. A light beam, typically from a hollow cathode lamp specific to the element of interest, passes through the flame. The atoms absorb light at characteristic wavelengths, reducing the light's intensity. This absorption is measured and related to the concentration of the metal in the sample.

The chemical composition of the synthesized precursors FFs was obtained through FAAS measurements performed on an Analyst 100 spectrometer from PerkinElmer at wavelengths of 248.3 nm and 240.7 nm for determining iron and cobalt concentrations, respectively. The FFs samples were previously digested with a concentrated HCl solution at boiling temperature and subsequently diluted with a 2% HNO_3 solution to ensure that the signal falls within the linear detection range. The assays were conducted at the Phenix Laboratory at Sorbonne Université.

2.2.4. Magnetic Characterization

Magnetometry experiments were conducted at 5 K and room temperature (300 K) using a Cryogenic S700X-R Superconducting Quantum Interference Device (SQUID) magnetometer, with applied magnetic fields up to 7 T, located at the Complex Fluids Laboratory of the Institute of Physiscs at UnB. The samples were prepared in Plexiglas® tubes sealed with tetrahydrofuran-based glue. Low-field measurements, used to determine the initial susceptibility, were performed in the ±10 mT range for samples APCo1 and APCo2, and in the ±5 mT range for sample APCo3.

2.2.5. Viscosity measurements

The viscosity measurements were obtained in collaboration with a Serbian group from the Department of Chemistry, Biochemistry, and Environmental Protection at the University of Novi Sad. A Brookfield Viscometer DV II + Pro was used to determine the viscosity values of pure EMIM TFSI and its binary mixtures with PC within a temperature range of 20 to 50 °C (with a fluctuation of ± 0.01 K). The Brookfield

Viscometer DV II+ Pro measures the viscosity of liquids by rotating a spindle within a sample and measuring the resistance to the spindle's rotation. A spindle type SC4-18 was immersed in an 8 cm^3 sample volume, and the appropriate speed was selected according to the expected viscosity. Ten measurements were taken for each experimental point.

For the pure PC sample, an Ubbelohde viscometer was used to measure the liquid's flow rate. This equipment measures the viscosity of a liquid by timing how long it takes for the liquid to flow through a capillary tube under the influence of gravity. The viscometer was calibrated, filled, thermostated, and cleaned following the procedure described in Vraneš *et al.* (89) . After achieving thermal equilibrium, a digital stopwatch (with an accuracy of ± 0.01 s) was used to record the flow time of the measured solutions. The relative standard uncertainty for both viscometers is approximately 1.5%.

2.2.6. Electrical Conductivity measurements

The electrical conductivity measurements were also conducted by the Serbian group. The measurements of the pure EMIM TFSI and its binary mixtures with PC were carried out in a Jenco 3107 conductivity meter, which is composed of a Pyrex cell containing platinum electrodes and operated within a temperature range of 20 to 50°C. The conductivity meter applies an alternating current through the electrodes and measures the resulting voltage drop.

The conductometric cell, with a total volume of 14 cm^3, was initially dried under a nitrogen atmosphere and then thermostated for 20 minutes using an external flow system (with an accuracy of ±0.01 K). Ten measurements were performed at intervals of 5 seconds to eliminate the self–heating and ionization in the electrodes (90). The experimental cell constant was determined to be 1.0353 cm^{-1} and the relative standard uncertainty for the measurements was 1.5%.

2.2.7. Inductively coupled plasma mass spectrometry (ICP-MS)

ICP-MS is a highly sensitive analytical technique used for detecting and quantifying trace elements and isotopes. In ICP-MS, the sample is introduced into a high-temperature plasma source, where it is ionized. The ions produced are then

directed into a mass spectrometer, which separates them based on their mass-to-charge ratios.

Information regarding the surface coverage, coating stability and nanoparticles leaching were obtained from the ICP-MS measurements. The equipment used for the measurements was an Agilent 7900 quadrupole ICP-MS. A scandium internal standard was introduced after inline mixing with the samples, to correct for signal drift and matrix effects. Calibration standards, spanning from 0.1 to 500 ppb, were analyzed to establish and verify the linear relationship between signal and concentration using simple linear regression, which was subsequently employed to translate the measured sample counts into concentrations. The measurements were conducted at the Institut de physique du globe de Paris.

2.2.8. Karl-Fisher Titration of Water

The water content for the pure solvents and mixtures was measured with Karl Fischer coulometric titration using a 831 Metrohm KF coulometer. In the case of the colloidal dispersions and the solvents used to prepare them, the water content was measured with an EcoCoulometer Metrohm coupled with a 860KF Thermoprep. The samples were sealed in a glass bottle under a nitrogen atmosphere and then placed in the Thermoprep furnace at 150°C. A needle pierces the cap, connecting the heated sample to the KF glassware via a heated pipe. The extracted water is titrated with the EcoCoulometer using Hydranal@Coulomat AG-Oven chemical. Initially, a bottle prepared under the same nitrogen atmosphere is measured as a blank.

2.2.9. Dynamic Light Scattering (DLS)

DLS measurements were performed at the Phenix Laboratory at the Sorbonne University with the equipment VascoKin from Cordouan Technologies. The laser operates at a wavelength of 638 nm and the detector is set in backscattering mode at a 170° angle. This equipment offers two significant advantages, enabling the examination of ionic liquid-based FFs. First, it allows measurements in any transparent container, enabling the use of minimal sample volumes and eliminating the risk of contamination from exposure to the atmosphere, as there is no need to open the sample bottle or transfer the sample to a holder in the equipment. Second, the backscattering mode

allows for the analysis of more concentrated samples, avoiding the need for dilution when using ionic liquid-based solvents (91).

The physics behind the DLS technique is based on the Brownian motion that results from collisions between stable colloidal particles and solvent molecules. In this interaction, energy is transferred, inducing motion in the particles, which move more rapidly the smaller they are, which indicates a higher diffusion coefficient. In the equipment, a laser with constant frequency is directed onto the sample, and the light scattered by the particles is detected at a specific angle over time.

The equipment measures the intensity correlation function $G(t)$, which can then be converted to the correlation function $G_1(t)$ using Equation 21

$$G_1(t) = \left[G(t)\right]^{1/2} - offset \tag{21}$$

The data are analyzed using the Frisken model, which is similar to the cumulants method, focusing on shorter time scales. This approach provides valuable insights into the sample behavior with a minimal number of parameters. Additionally, the shape of the correlation function at longer times reveals whether a significant fraction of larger objects is present.

In a scenario where interactions are negligible, the hydrodynamic diameter (d_h) can be obtained using the Stokes-Einstein Equation (Equation 22).

$$D = \frac{k_B T}{3\pi\eta d_h} \tag{22}$$

where D is the translational diffusion coefficient, k_B is the Boltzmann constant, T is the absolute temperature, and η is the solvent viscosity.

2.2.10. Small Angle X-ray Scattering (SAXS) Studies

SAXS studies were conducted in the Complex Fluids Laboratory at the Institute of Physics at UnB using the Xeuss 2.0 equipment from Xenocs with a Cu-Kα X-ray source (λ = 1.5406 Å). Samples of FFs dispersed in HNO_3 acidic medium with various NP volume fractions (ϕ_{NP}) were placed in polyimide tubes with an internal diameter of 700 μm.

For the other samples studied, SAXS measurements were performed in the Swing beamline of the Soleil synchrotron facility in Saint Aubin, from which a larger

range of scattering angles were obtained. The beam energy ranged between 12 and 16 keV, and two sample-detector distances were employed to cover a wide Q range extending from 0.001-0.003 to 0.4 Å. Flat capillaries of borosilicate of 100 μm of thickness were used.

In Figure 21, a representation of a SAXS measurement is shown, in which X-rays are scattered due to their interaction with the sample´s electrons. The scattering can be elastic (Rayleigh Scattering), in which the wavelength and energy of the scattered beam are equal to those of the incident beam, or inelastic (Compton Scattering), where there is a decrease in energy and an increase in the wavelength of the scattered beam. For SAXS, inelastic scattering can be neglected, and the focus is on elastic scattering, which implies defining the scattering vector (q) as Equation 23, where θ corresponds to the scattering angle between the incident and scattered beams.

$$q = \frac{4\pi}{\lambda}\sin\theta \tag{23}$$

Rearranging Bragg's Law with Equation 23, q can be rewritten as in Equation 24.

$$q = \frac{2\pi}{d} \tag{24}$$

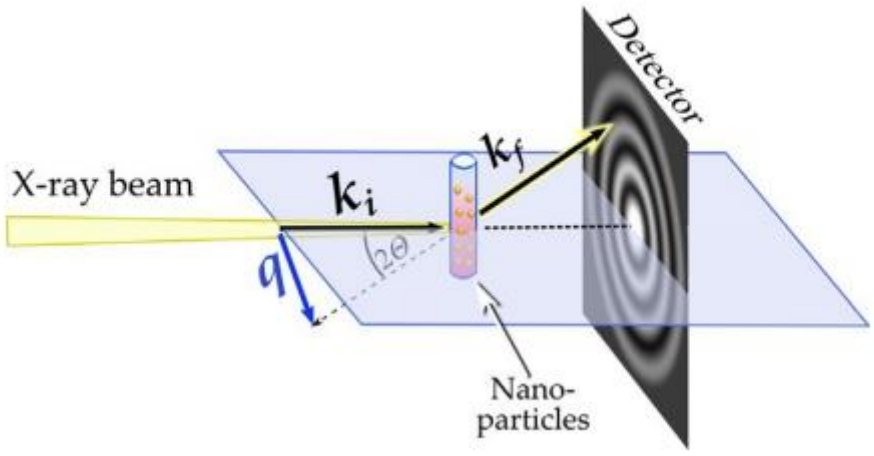

Figure 21. Schematic representation of the SAXS technique set-up. Reproduced from (92).

From Equation 24, it can be inferred that the interplanar distance (d) is inversely proportional to the scattering vector (q) and consequently to the scattering angle (θ). Thus, in SAXS experiment, decreasing the scattering angle enables the investigation of

longer length scales, which allows the study of the geometry and interparticle interactions in a dispersion. In contrast, the XRD technique provides data related to the atomic planes of the NPs, since larger angles are analyzed.

The scattering intensity for a monodisperse and diluted dispersion can be written as Equation 25, where N is the number of particles of average volume V_p per volume unit of solution, $\Delta\rho^2$ is the contrast between the particles and the solvent, and F(q) is the form factor (93,94).

$$I(q) = NV_p^2 \Delta\rho^2 \left|F(q)\right|^2 \tag{25}$$

The form factor represents the scattering contributions from individual domains and describes the shape or spatial distribution of a particle. It depends on the particle's size, shape, and internal structure and is essential for characterizing the morphology of NPs. The form factor for a spherical particle as a function of the radius can be expressed as Equation 26 (95).

$$F(q) = \frac{3\left[\sin(qR) - qR\cos(qR)\right]^2}{(qR)^3} \tag{26}$$

Thus, the scattering intensity for a dilute dispersion of monodisperse spheres can be written as Equation 27.

$$I(q,d) = N\Delta\rho^2 \left(\frac{\pi}{6}\right)^2 d^6 \left|F(q,d)\right|^2 \tag{27}$$

However, the FF samples studied in this work are polydisperse with a size distribution well-adjusted by a log-normal distribution (P(d)). Thus, the scattering intensity can be written as Equation 28.

$$I(q) = N\Delta\rho^2 \left(\frac{\pi}{6}\right)^2 \int_0^\infty d^6 \left|F(q,d)\right|^2 P(d)dd \tag{28}$$

In addition, N can be described as Equation 29:

$$N = \frac{\phi}{\langle V_p \rangle} \tag{29}$$

Finally, the scattering intensity for this system is expressed as Equation 30:

$$I(q) = \frac{\pi}{6}\phi\Delta\rho^2 \frac{\int_0^\infty d^6 \left|F(q,d)^2\right| P(d)dd}{\int_0^\infty d^3 P(d)dd} \quad (30)$$

Note that the solution to the Equations depends on the q range. Solving the equations in the low-q range yields what is known as the Guinier law, also referred to as the Guinier approximation. In contrast, at high-q values, the solution is known as Porod's law.

The different regions of a SAXS curve offer various insights into the studied sample. Figure 22 illustrates the structural information that can be obtained from each region of a SAXS curve. In the low-q region, known as the Guinier region, the scattering data allows for the determination of the radius of gyration (R_g) and provides information about aggregation, offering insights into the overall dimensions of the clusters. As the curve progresses into the intermediate-q region, the fractal dimension (DF) can be determined from the power-law behavior, $I(q) \sim q^{-DF}$, revealing how densely the primary particles are packed within the aggregate. Finally, in the high-q Porod region, the sharp decrease in scattering intensity provides information about the surface structure and interface sharpness of the primary particles. This multi-region analysis allows for a comprehensive understanding of the hierarchical structure, from large-scale aggregates to the surface characteristics of individual particles. A more detailed analysis of each region of the curve will be discussed in the Appendix.

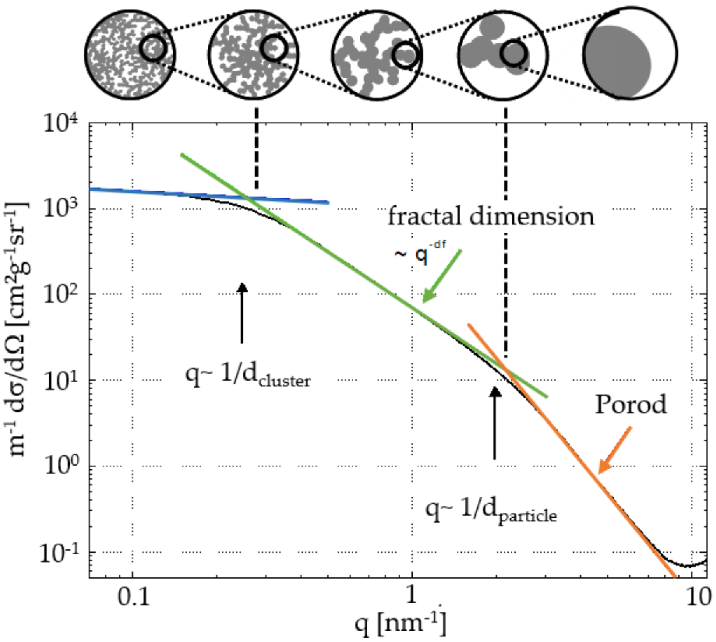

Figure 22. Scattering curve of a supercritical drying (SCD)-dried silica aerogel, used here to highlight the distinct regions of the curve and the observations from each region. Reproduced from (96).

The discussion above does not consider the possible interactions between the scattering objects due to the dilute consideration. However, for the colloidal dispersions studied, it may be important to include the Structure Factor S(q) to account for NP interactions that influence the scattering intensity, as this factor reflects the scattering caused by the spatial position of the particles. This is illustrated in Equation 31 for spherical objects, where $I_{ff}(q)$ represents the scattering intensity based solely on the form factor.

$$I(q) = I_{ff}(q).S(q) \tag{31}$$

For high values of q, the Structure Factor S(q) approaches 1, indicating that there is little information about the correlation between particles in this range. As q approaches zero, the interactions within the system become more evident. An S(q) value less than 1 suggests a repulsive system, while a value greater than 1 indicates an attractive system and/or the presence of aggregates. In attractive systems, an increase in S(q) near q = 0 (over significant distances) may reflect considerable heterogeneities and potential aggregate formation (97).

2.2. Samples preparation

In this section, the synthesized NPs undergo various procedures to produce samples for evaluating the influence of different parameters. The NP surfaces are functionalized with imidazolium-based ligands in aqueous media. Adsorption experiments are conducted to assess adsorption capacity and the effect of temperature, while pH influence assays evaluate the coating stability. Additionally, the process of dispersing the NPs in pure EMIM TFSI, PC, and their mixtures is discussed in detail. The ionic liquid-dispersed samples are also subjected to heating to assess its impact on colloidal stability.

2.2.1. Tuning the surface of nanoparticles

To disperse the NPs in EMIM TFSI, PC and their mixtures, their surface charge density was previously adjusted in the water-based FFs, through a wet route previously proposed by Riedl *et al*. (11) for maghemite NPs. In this method, the nitrate counter-ions, which balance the positive surface charge of the NPs, were replaced with imidazolium-based ligands. These ligands and their molecular structures are shown in Table 3 and Figure 23, respectively.

Table 3. Imidazolium-based ligands

Abbreviation	IUPAC name	Origin
$SBMIM^{\pm}/TFSI^{-}$	1-Methyl-3-(4-sulfobutyl)imidazolium bis(trifluoromethanesulfonyl)imide	Solvionic, France
$PAC_4MIM^{\pm}Br^{-}$	1-methyl-3-(butylphosphonic acid) imidazolium bromide	Sikemia, France
$PAC_6MIM^{\pm}Br^{-}$	1-methyl-3-hexylphosphonic acid) imidazolium bromide	Sikemia, France, special synthesis on demand

SBMIM$^{\pm}$/TFSI^{-}

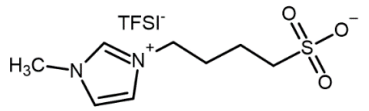

PAC$_4$MIM$^{\pm}$Br^{-}

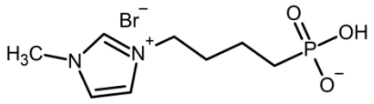

PAC$_6$MIM$^{\pm}$Br^{-}

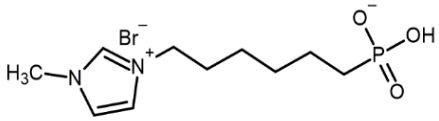

Figure 23. Molecular structure of the ligands.

The choice of these ligands is based on previous results obtained for maghemite NPs and also because it allows the evaluation of the influence of both the nature of the attaching negative group and the side-chain length. SBMIM$^{\pm}$/TFSI^{-} adsorbs on the positive surface site of the NP via its negative sulfonic group, while PAC$_4$MIM$^{\pm}$Br^{-} and PAC$_6$MIM$^{\pm}$Br^{-} via their negative phosphonic group.

To tune the NP's surface based on the method proposed by Riedl *et al.* (11), a 0.1 mol/L NaOH solution is gradually added until the point of zero charge is reached (pH ≈ 7). The NPs are then magnetically separated and washed several times with ultrapure water to remove all ions. Following this, the ligands in their acidic form are added until the pH reaches approximately 2 (with a ligand concentration ≈ 75 mmol/L).

2.2.2. Impact of pH on sample stability

Studies on the influence of pH were conducted for the APCo2 NPs dispersed in water. After coating the surface with PAC$_6$MIM$^{\pm}$Br^{-}, according to the procedure outlined in section 2.2.1. The influence of the pH was performed only for the APCo2 NPs because of the successful results previously obtained for maghemite NPs with a similar size to APCo2 (11,28). Regarding the chosen ligand, based on the functionalization results obtained from the experiments outlined in Section 2.2.1, only the ligand PAC$_6$MIM$^{\pm}$Br^{-} was used for this the study of the influence of the pH. In this investigation, the pH was increased by gradually adding a 0.1 mol/L NaOH solution. The d_h was then obtained through DLS.

2.2.3. Adsorption isotherms

To obtain the adsorption curves for the ligands, 300 μL of the water-based FF at Φ_{NP} = 0.4% were mixed with 300 μL of PAC_6MIMBr solutions from 10 to 100 mmol/L for 3 hours under magnetic stirring of 400 rpm at 80 °C and pH ≈ 2, which was set with a HNO_3 solution to maintain the same counter-ion as the original FF. These experimental conditions were adapted from Djaniš *et al* (2022) (98). After the contact time, the samples were left to cool to room temperature and centrifuged to separate the NPs using an ultracentrifugation Optima 70 from Beckman Coulter, at 30.000 rpm for 4 hours at 20 °C. The concentration of $PAC_6MIM^{\pm}$ (as phosphorous content) and Br^- were determined in the supernatant phase by ICP-MS.

To check the influence of the temperature on the coating process, an adsorption test at room temperature was conducted using a sample prepared following the conditions described in Section 2.2.3, comprising 400 μL of FF at ϕ_{NP} =1.0 %, pH = 2.2, and $PAC_6MIM^{\pm}Br^-$concentration approximately 88 mmol/L. The sample was centrifuged with the same conditions as the adsorption procedure described above. The concentration of Fe^{3+} and Co^{2+} was also quantified by ICP-MS.

2.2.4. Dispersions in pure IL

To obtain the dispersions in pure IL, an equivalent volume of EMIM TFSI was mixed with the water-based FFs produced as described in Section 2.2.1. After that, the water was removed by pumping at 0.0031 mbar for 24h at room temperature.

A different methodology was also employed to study the coating stability in ionic liquid. Following the procedure of Section 2.2.1 and after adding the IL, the aqueous phase was removed with a pipette. The NPs were then separated from the IL by ultracentrifugation at 30.000 rpm for 16 hours at 20°C, and the EMIM TFSI supernatant was removed with a pipette. The amount of $PAC_6MIM^{\pm}$ and Br^- in each phase was determined ICP-MS. For the analysis of the NPs, they were first digested with 37% HCl and appropriately diluted before analysis. Figure 24 shows a diagram of the phases obtained in this procedure.

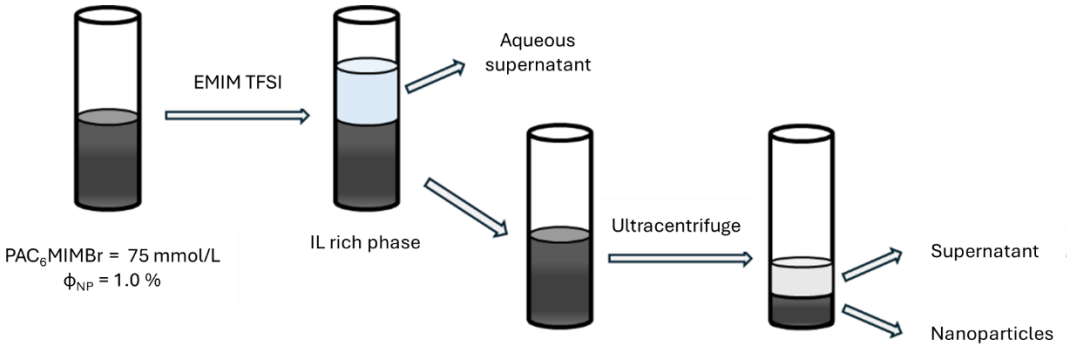

Figure 24. Diagram of the methodology for study of the coating stability.

2.2.5. Dispersions in pure PC

After coating the NPs as described in Section 2.2.1, the pure PC dispersions cannot be pumped after adding the solvent because it vaporizes. Another option is heating; however, heating the mixture of PC and water in the presence of NPs destroys the solvent, making it very viscous. This effect is likely due to the carbon ring opening, a characteristic observed in this type of cyclic molecules (99), and is further enhanced by the presence of oxide NPs. Therefore, after coating the NPs with the ligand, the water is removed by vacuum pumping (0.0031 mbar, 24 hours, room temperature). PC is then added, and the NPs are redispersed by heating at 80°C for a few minutes.

2.2.6. Dispersions in mixtures of EMIM TFSI and PC

Several composition mixtures of EMIM TFSI and PC were produced with a NP volume fraction of ϕ_{NP} = 1%, specifically at χ_{IL} = 0.14, 0.25, 0.35, and 0.67. These compositions were chosen based on conductivity and viscosity measurements as a function of temperature. For these samples, a concentrated dispersion of APCo2 NPs coated with $PAC_6MIM^{\pm}$ in EMIM TFSI with ϕ_{NP} = 3% was produced following the procedure in Section 2.2.4. Subsequently, PC and EMIM TFSI were added to achieve the target χ_{IL} and a ϕ_{NP} of 1%.

2.2.7. Heating cycles up to 200 °C

Studies on the thermal stability of the dispersions were conducted for the APCo1 and APCo2 NPs samples coated with $PAC_6MIM^{\pm}Br^{-}$ and dispersed in EMIM TFSI. The

samples were heated to a specific temperature (50, 100, 150 and 200 °C) for two hours, then allowed to cool to room temperature to measure the d_h using the VascoKin DLS Particle Analyzer from Cordouan Technologies. Subsequently, the same sample was heated to a higher temperature and d_h was measured again. Figure 25 provides a schematic diagram to illustrate the procedure. After exposing the sample to the heating cycles, a measurement after one month was also taken.

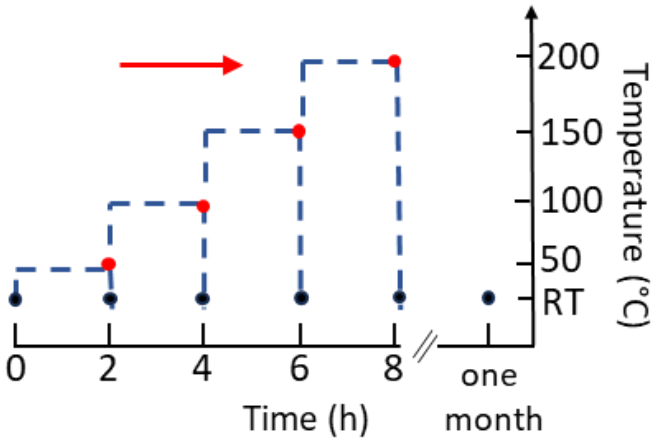

Figure 25. Methodology for study of the temperature influence.

Chapter 3

This chapter will begin by characterizing the crystal structure and mean diameter of the NPs using XRD measurements, followed by an analysis of size and size distribution from TEM micrographs for the three synthesized samples. The chemical composition of the FFs and the volumetric fraction of NPs will be evaluated using FAAS. Additionally, the magnetic properties of the samples will be characterized. The chapter will conclude with a solvent characterization, presenting measurements of the viscosity and electrical conductivity of EMIM TFSI and PC mixtures as a function of temperature, with varying EMIM TFSI mole fractions. Finally, a summary of the chapter will be presented at the end.

3. Characterization of the initial aqueous dispersions and the solvents

3.1. Structural morphology and composition

The crystal structure and mean diameter of the NPs is obtained from XRD measurements. In Figure 26, the diffractograms with characteristic peaks for the three studied samples are shown. The displayed peak pattern corresponds to the spinel-type structure, as indicated by the reference peaks for cobalt ferrite and maghemite provided by the International Center of Diffraction Data – ICDD, depicted in the figure by the black (ICDD-PDF: 022-1086) and red lines (ICDD-PDF: 39-1346) at the bottom, respectively.

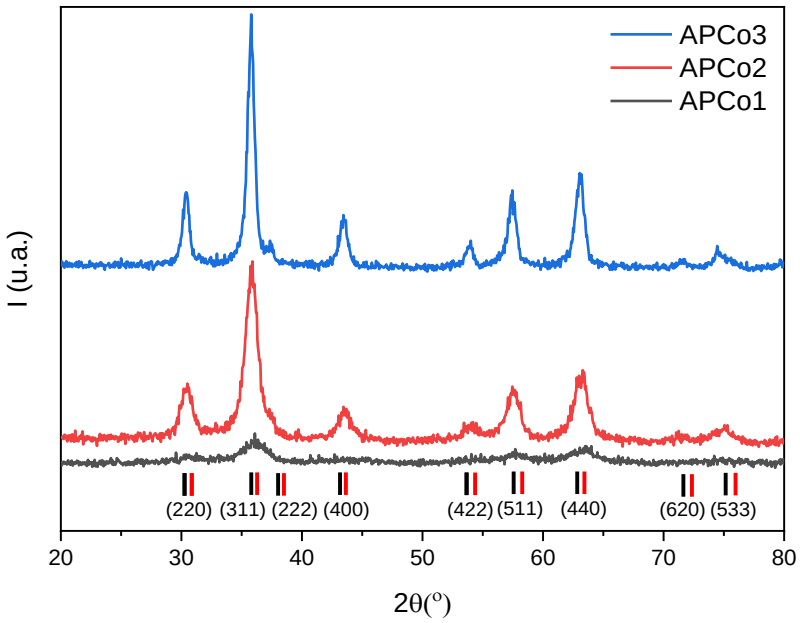

Figure 26. X-ray diffractograms for APCo1, APCo2 and APCo3 with their respective Miller indexes.

The calculated lattice parameters are 0.826, 0.830, and 0.832 nm for APCo1, APCo2, and APCo3, respectively. These values validate the spinel-type crystal structure presented by both cobalt ferrite and maghemite, which have lattice parameters of 0.839 and 0.834 nm, respectively.

The Scherrer equation (Equation 19) is employed to determine the d_{rx}, where the parameters θ and λ are obtained from the fitting performed in the *Origin* software for

the most intense peak of the diffractogram. The d_{rx} values are 3.9, 7.4, and 13.4 nm for APCo1, APCo2, and APCo3, respectively.

Figure 27 shows examples of micrographs obtained from TEM, in which it can be observed that the NPs exhibit approximately a spherical shape.

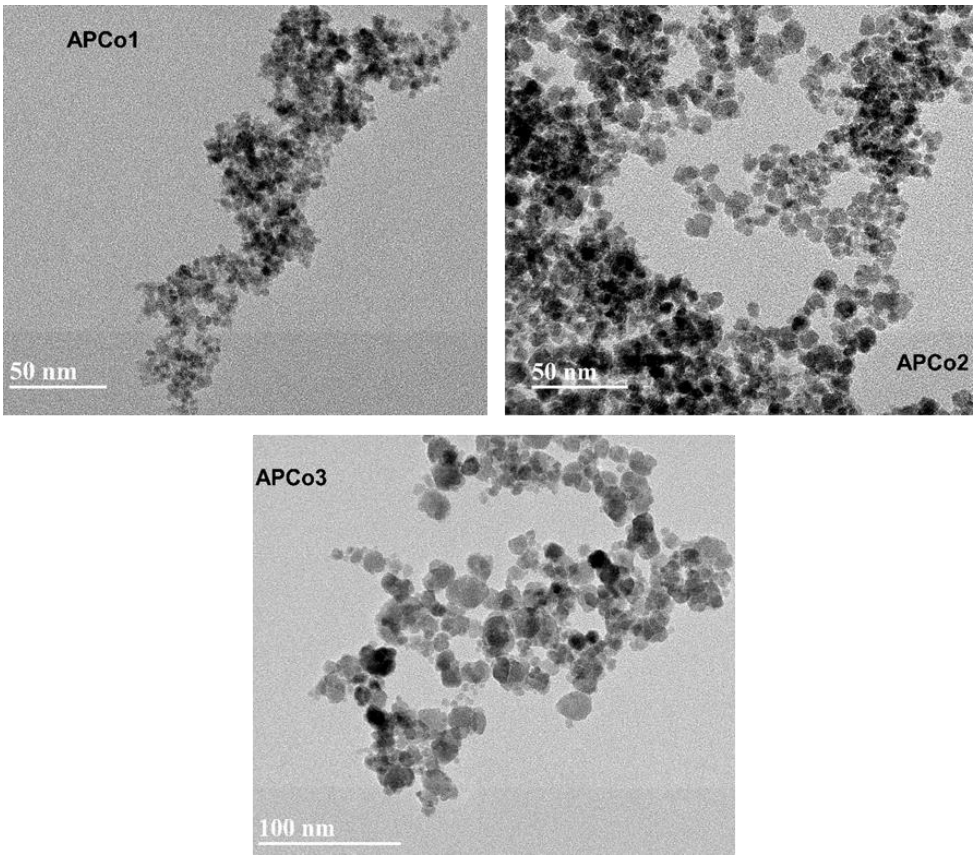

Figure 27. TEM micrographs for APCo1, APCo2 and APCo3, respectively.

Figures 28, 29 and 30 show the histogram of size distribution fitted to the log-normal function, for APCo1, APCo2 and APCo3, respectively.

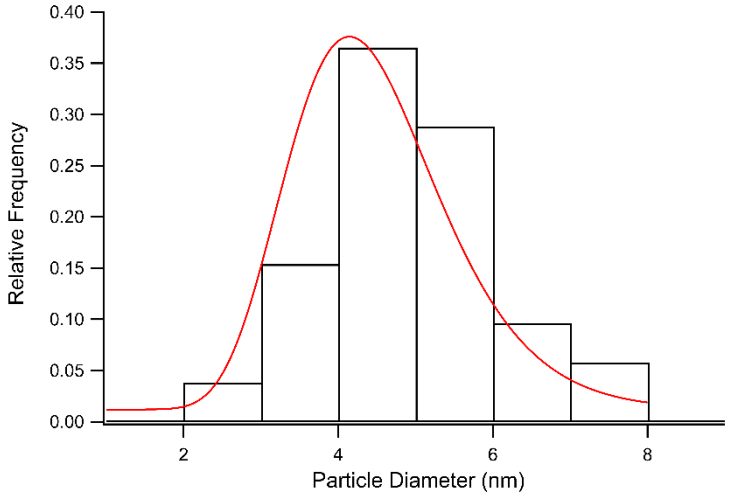

Figure 28. Histogram of size distribution adjusted to the log-normal function for APCo1.

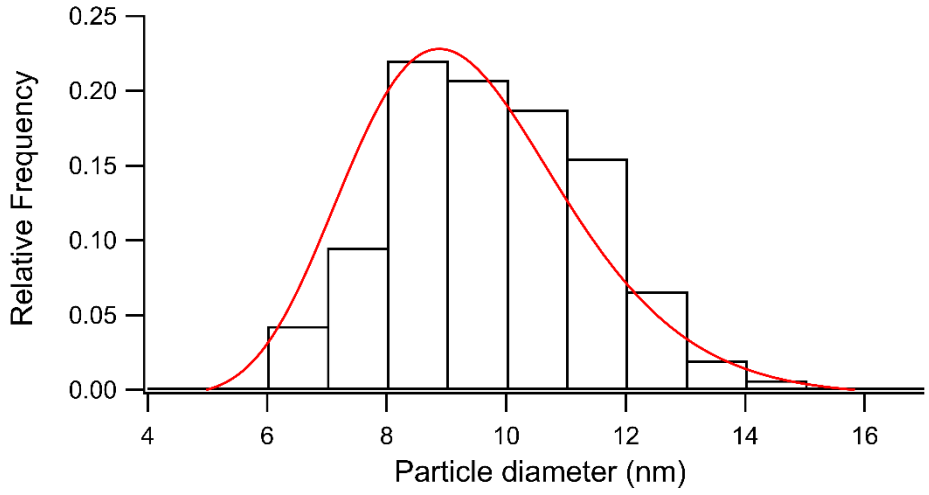

Figure 29. Histogram of size distribution adjusted to the log-normal function for APCo2.

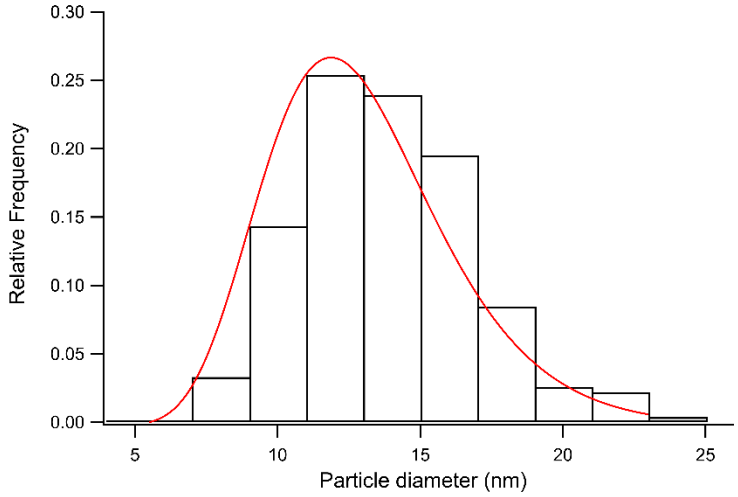

Figure 30. Histogram of size distribution adjusted to the log-normal function for APCo3.

The average diameter values obtained from TEM (d_0) and XRD (d_{rx}), as well as the polydispersity of the NPs, are presented in Table 4. Significant variations in average diameters across the three syntheses (APCo1, APCo2, and APCo3) were observed with both techniques, confirming the effectiveness of using bases with different strengths to control the mean NP size.

Table 4. Data obtained from XRD and TEM.

Samples	***d_{rx}* (nm)**	***d_0* (nm)**	***s***
APCo1	4.0	4.1	0.33
APCo2	7.4	8.9	0.28
APCo3	13.4	11.9	0.35

From the concentration data of Fe and Co obtained from FAAS measurements, the volumetric fraction of the NPs (ϕ_{NP} (%)) is calculated for the analyzed FF samples. Given the core@shell consideration, ϕ_{NP} is the sum of the volumetric fraction of the core ϕ_{core} and the surface $\phi_{surface}$ (Equation 32).

$$\phi_{NP} = \phi_{core} + \phi_{surface} \tag{32}$$

The volumetric fraction can be expressed by dividing the molar concentration by the molar volume, and considering the 2:1 ratio ([Fe]:[Co]) employed in the synthesis of the FFs, Equation 32 can be rewritten as follows (Equation 33):

$$\phi = [Co]V_m^{core} + \frac{[Fe]-2[Co]}{2}V_m^{surface} \quad (33)$$

where V_m^{core} is the molar volume of the cobalt ferrite core (V_m^{core} = 43,53 cm^3/mol) and $V_m^{surface}$ is the molar volume of the maghemite surface ($V_m^{surface}$ = 32,00 cm^3/mol).

Another parameter that can be calculated from FAAS measurements is the thickness of the shell of the NPs, according to Equation 34 (87).

$$e = \frac{d_{rx}}{2}\left\{1-\left[\left(\frac{\phi_{NP}}{\phi_{surface}}-1\right)\frac{n_{core}}{n_{surface}}+1\right]^{1/3}\right\} \quad (34)$$

where *e* is the thickness, n_{core} is the number of atoms per unit cell in the cobalt ferrite core (n_{core} = 24), and $n_{surface}$ is the number of atoms per unit cell in the maghemite core ($n_{surface}$ = 21).

Table 5 presents the results from FAAS measurements, showing that the shell fraction decreases as the NP size increases. This can be explained by the nanoscale characteristics of the material, where smaller NPs have a larger surface-to-volume ratio. The corresponding shell thickness is on the order of the lattice size of the spinel oxide.

Table 5. Flame Absorption Spectroscopy Data

Samples	ϕ_{NP} **(%)**	$\phi_{surface}$ **(%)**	ϕ_{core} **(%)**	$\frac{\phi_{surface}}{\phi_{NP}}$	***e*** **(nm)**
APCo1	3.84	2.14	1.70	0.56	0.44
APCo2	3.65	1.04	2.61	0.28	0.35
APCo3	3.21	0.47	2.74	0.15	0.31

3.2. Magnetic Characterization

Hysteresis loops are obtained at 5 K (Figure 31) to magnetically characterize the precursor FF samples dispersed in water with NO_3^- counter-ions. Key parameters derived from the curve include the saturation magnetization (m_s), which represents the maximum magnetization achievable when all magnetic moments are fully aligned with the external magnetic field; the remanent magnetization (m_r), indicating the magnetization that remains after the external field is removed; and the coercivity (H_c),

which is the strength of the external magnetic field needed to reduce the magnetization to zero after saturation. Additionally, magnetic anisotropy, which reflects the directional dependence of a material's magnetic properties, is typically quantified by the anisotropy constant (K) and can be calculated using the Stoner and Wohlfarth model (100), as given by Equation 35. This model assumes uniaxial anisotropy and disregards thermal fluctuations.

$$H_c = 0.48\frac{2K}{\mu_0 m_s} \tag{35}$$

where μ_0 is the magnetic permeability of the vacuum. Table 6 presents the magnetization data for the three samples.

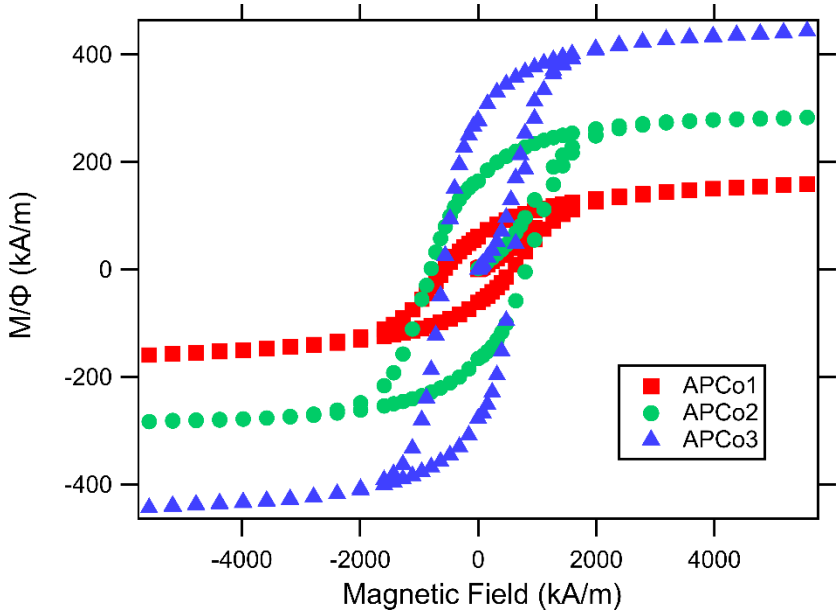

Figure 31. Magnetization versus applied field curve, normalized by the volume fraction, for the APCo1, APCo2 and APCo3 FFs in HNO_3 acidic medium at 5K.

Table 6. Magnetization data of APCo1, APCo2 and APCo3 for the precursor´s FFs at 5K.

Sample	H_c **(kA/m)**	m_s **(kA/m)**	m_r **(kA/m)**	m_r/m_s	K **(J/m^3)**
APCo1	636.6	159.2	61	0.38	1.3 x 10^5
APCo2	795.8	282.8	164.6	0.58	2.9 x 10^5
APCo3	636.5	443.4	276.3	0.62	3.7 x 10^5

Additionally, the critical diameter $d_c(T)$, below which NPs with uniaxial anisotropy enter the superparamagnetic state, is calculated at room temperature using Equation 36 (101), based on the magnetic anisotropy determined from the hysteresis loop at 5 K. Figure 32 presents the size distribution (TEM) of the three samples, indicating the threshold below which the NPs exhibit superparamagnetic behavior at 300 K.

$$d_c(T) = \sqrt[3]{\frac{150K_BT}{\pi K}} \tag{36}$$

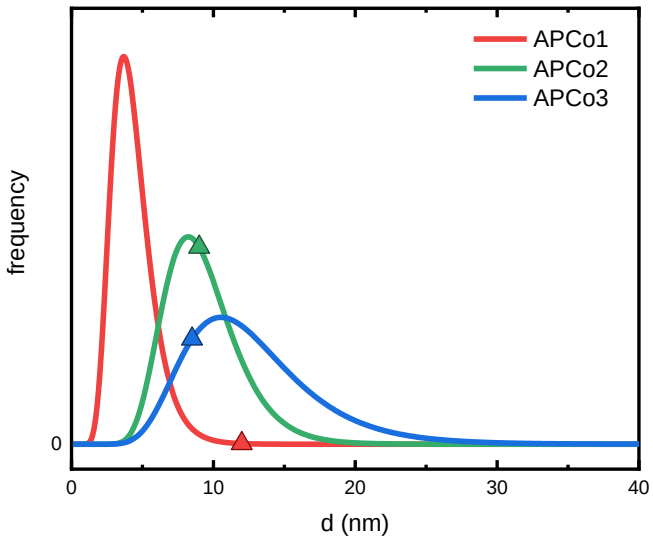

Figure 32. Size distribution of each cobalt ferrite sample, where the highlighted point in each distribution marks the diameter below which samples arein the superparamagnetic state at room temperature (300 K)

As shown in Table 6, larger NPs sizes correspond to higher m_s values. This expected behavior can be attributed to the structural organization of the NP surface and the proportion of surface atoms. Surface atoms are more disordered compared to those in the core, disrupting the alignment of their magnetic moments. As NP size decreases, the surface-to-volume ratio increases, resulting in a greater fraction of atoms with weakened magnetic alignment. Consequently, smaller nanoparticles exhibit lower m_s values due to these surface effects. The ratio m_r/m_s and K also decrease with particle size, as expected, with *K* values for the samples ranging from 1.0×10^5 to 3.0×10^6 J/m^3 as predicted in the literature for cobalt ferrite NPs (102).

Magnetization measurements at room temperature are also performed for water-based samples with ϕ_{NP} around 1.0% after functionalization of the NPs surface with $PAC_6MIM^{\pm}$. The magnetization curve is presented in Figure 33.

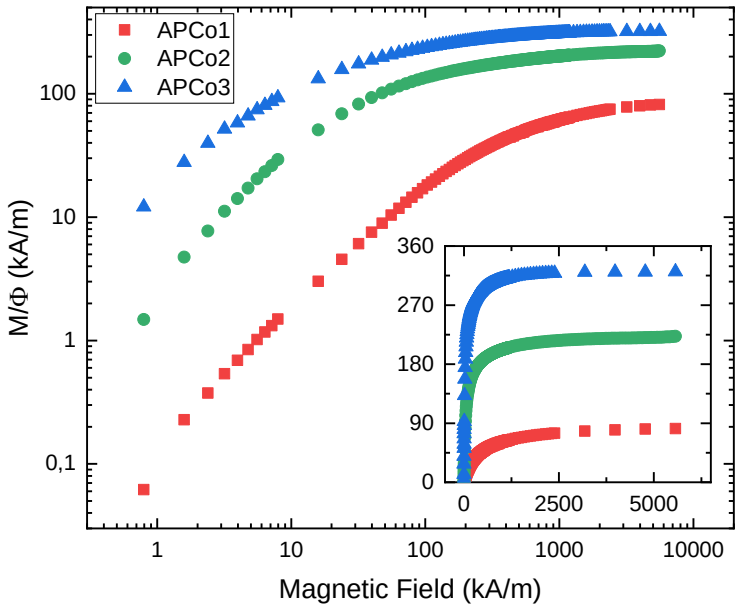

Figure 33. Magnetization versus applied field at room temperature, normalized by the volume fraction, for APCo1, APCo2 and APCo3 in dilute regime in water. The surface is coated with $PAC_6MIM^{\pm}$ ligands.

The main graph presents the data on a log-log scale for enhanced visualization, while the inset shows the curves on a linear scale. As observed in the main graph, m_s is more easily reached as the NP size increases. Table 7 summarizes the m_s values, which are obtained by extrapolating to infinite magnetic field value, as well as the dipolar parameter, ψ_{dd}, which is expressed by Equation 37 (where *d* is the diameter of the NPs). This parameter is determined from the initial susceptibility (χ) in the linear region of the low-field magnetization (< 800 A/m or 100 Oe), as expressed by Equation 38. For individually dispersed NPs or clusters, ψ_{dd} serves as a measure of their size distribution. Its value indicates their potential to form chains through dipolar magnetic interactions: a value of $\psi_{dd} >> 8\pi$ indicates possible chain formation, whereas $\psi_{dd} << 8\pi$ indicates no chain formation (97).

$$\psi_{dd} = \frac{\mu_o m_s^2 \pi d^3}{6kT} \qquad (37)$$

$$\psi_{dd} = \frac{3\chi}{\phi} \tag{38}$$

Table 7. Magnetization data of APCo1, APCo2 and APCo3 for the samples with the surface functionalized.

Sample	m_s (kA/m)	ψ_{dd}
APCo1	82	0.58
APCo2	229	12
APCo3	323	70

Once again, the significant difference in magnetic properties due to NP size becomes evident. The dipolar interaction parameter characterizes the NPs in APCo1, where magnetic interactions between NPs are negligible compared to thermal energy (k_BT). For APCo2 and APCo3, it represents an effective value for dispersed clusters, with interactions respectively comparable to and greater than k_BT. No chain formation is expected in APCo1 or APCo2, while in APCo3, the larger NPs are predicted to form chains, as indicated by $\Psi_{dd} >> 8$ (101). In APCo3, the much larger NPs can produce chains and loops due to the strong dipolar magnetic interaction (97), resulting in a markedly different behavior.

3.3. Colloidal Stability

DLS and SAXS measurements are obtained for the synthesized FFs to provide a first analysis regarding colloidal characterization. Figure 34 shows the correlation function curves for the three synthesized dispersions at a ϕ_{NP} = 1.0%. The apparent d_h is presented in Table 8.

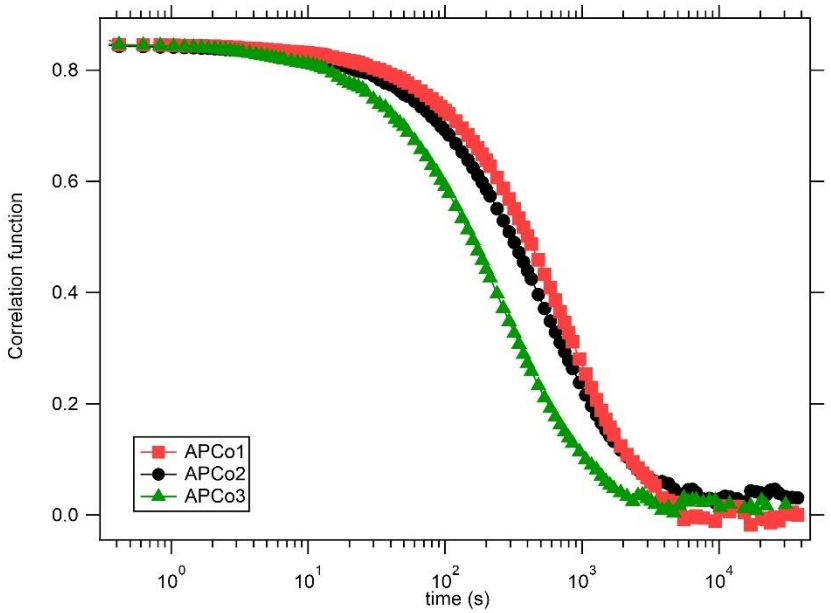

Figure 34. Correlation function curves for the three NPs sizes dispersions in water with NO_3^- as a counter-ion, at ϕ_{NP} = 1.0%.

Table 8. Hydrodynamic diameter for the three samples of synthesized FFs at ϕ_{NP} = 1.0%.

Sample	d_h (nm)
APCo1	210
APCo2	160
APCo3	80

To further support the DLS data, SAXS measurement curves are obtained at varying ϕ_{NP} for the three nanoparticle sizes as presented in Figure 35, 36 and 37 for samples APCo1, APCo2, and APCo3, respectively.

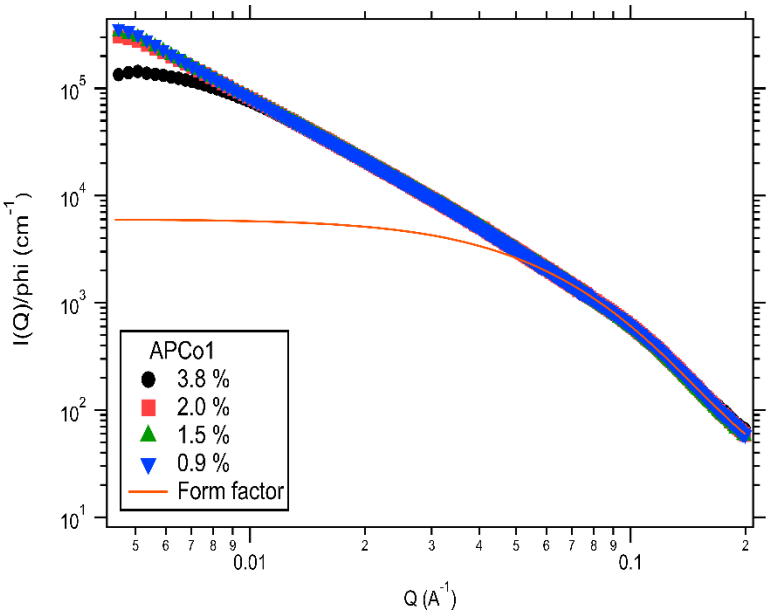

Figure 35. Scattering profile in absolute scale normalized by the volume fraction of nanoparticles for APCo1 dispersed in water with NO_3^- as a counter-ion. Form factor using a lognormal distribution with d_0 = 2.6 nm and sigma = 0.45.

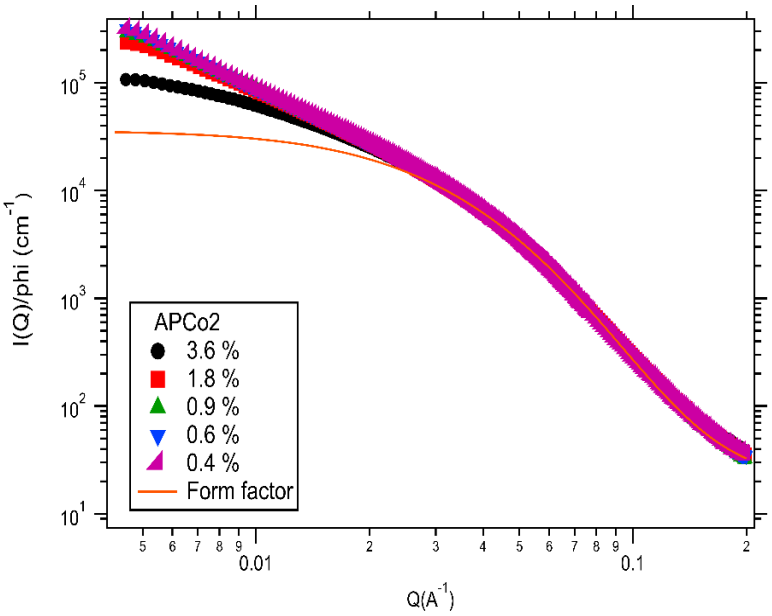

Figure 36. Scattering profile in absolute scale normalized by the volume fraction of nanoparticles for APCo2 dispersed in water with NO_3^- as a counter-ion. Form factor using a lognormal distribution with d_0 = 4.7 nm and sigma = 0.45.

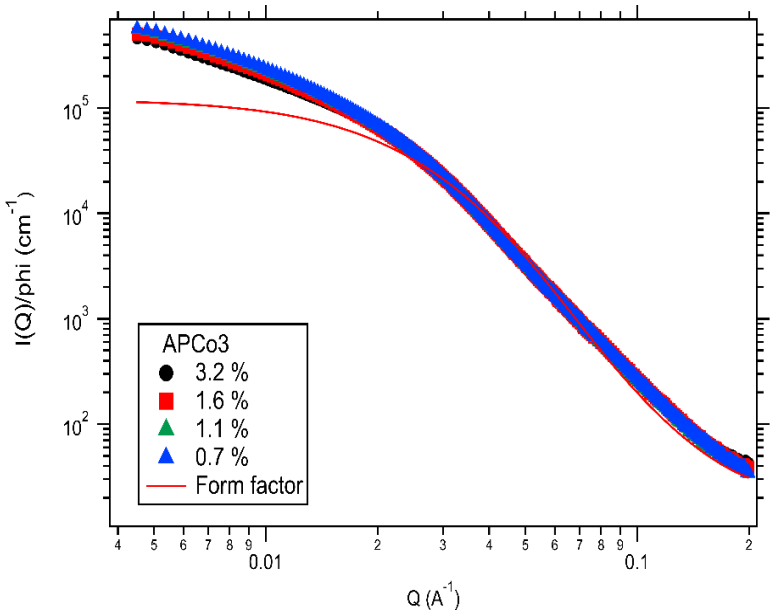

Figure 37. Scattering profile in absolute scale normalized by the volume fraction of nanoparticles for APCo3 dispersed in water with NO_3^- as a counter-ion. Form factor using a lognormal distribution with d_0 = 7.9 nm and sigma = 0.40.

Based on the DLS and SAXS measurements, it can be inferred that the samples are primarily composed of clusters of nanoparticles, which are stable in the long run and cannot be broken by changes in the ionic strength resulting from dialysis or washing the nanoparticles several times.

In the SAXS data, attempts were made to fit a form factor to the high-q region. However, due to the presence of aggregates, it was not possible to obtain a reasonable form factor that accurately models any of the samples. These clusters are a result of Reaction Limited Colloidal Aggregation (RLCA) (103), a universal process that occurs independently of the specific chemical composition of the colloidal system. The data indicate a trend where smaller nanoparticles tend to form larger clusters, as evidenced by the values in Table 8. This is further supported by the widening gap between the experimental intensity curve for the more diluted samples, which exhibit fewer interaction effects, and the form factor curves. This gap increases as the nanoparticle size decreases. This behavior may be explained by the reduction of the saturation structural charge with the average nanoparticle size due to the spatial confinement at the nanoscale, as reported by Campos *et al.* in similar nanoparticles (104). As the nanoparticle size decreases, the number of potentially chargeable sites also diminishes, which is attributed to the increase of hydroxo-bonded sites with very low acidity and an

unusual coordination environment for surface atoms. Consequently, smaller nanoparticles are more prone to agglomeration due to the reduced electrostatic repulsion between them. Additionally, the increased tendency of smaller nanoparticles to cluster may be linked to their elevated surface energy, which drives agglomeration to reduce it (104).

For the APCo1 and APCo2 samples, a decrease in intensity is observed in the low q range as the volumetric fraction increases, suggesting the presence of repulsive interactions between the clusters.

3.4. Solvents characterization

Regarding the solvents used in this work, there is no data regarding the viscosity and electrical conductivity of EMIM TFSI/ PC mixtures. The primary goal of measuring these properties is to determine an optimal solvent composition that balances low viscosity with high electrical conductivity. This balance is essential for enhancing the thermoelectric properties of the FF. In Figures 38 and 39, the viscosity and electrical conductivity as a function of temperature are presented.

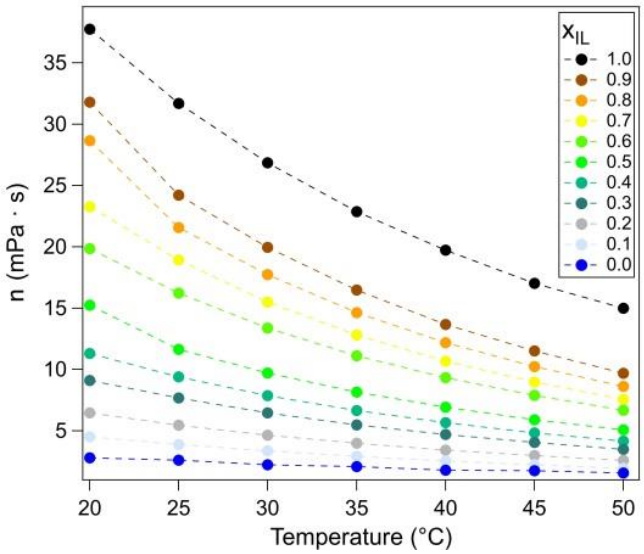

Figure 38. Viscosity of the EMI TFSI + PC mixtures as a function of temperature, varying EMIM TFSI mole fractions (χ_{IL})

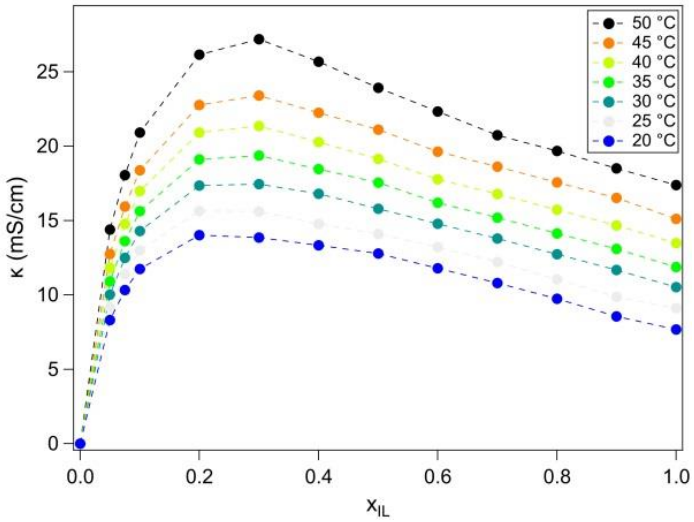

Figure 39. Electrical conductivity of the EMIM TFSI/PC mixtures as a function of temperature, varying EMIM TFSI mole fractions (χ_{IL})

Analyzing Figure 38, the viscosity decreases with increasing temperature for all compositions. This outcome is expected, as thermal energy allows solvent molecules to move more freely. In terms of solvent composition, viscosity decreases with an increasing mole fraction of PC. This is because PC molecules disrupt the ordered structure of the ionic liquid by inserting themselves between the EMIM TFSI molecules (52,105)

Regarding Figure 39 increasing the PC mole fraction initially leads to a rise in electrical conductivity, peaking at x_{IL} values between 0.2 and 0.3 across all temperatures. This is because PC molecules solvate the EMIM TFSI ions, loosening them as some cation-anion interactions are replaced by strong hydrogen bonds between the $EMIM^+$ cations and PC molecules (106,107). However, further increasing the PC mole fraction beyond the peak causes a sharp decrease in electrical conductivity, eventually reaching zero, due to the non-ionic nature of PC.

3.5. Summary

The primary conclusion drawn from the synthesized FFs in this chapter is that all techniques indicate significant property differences among the three samples, attributed to size variations, confirming the successful synthesis. As for the EMIM TFSI and PC mixtures, their characterization reveals that while the addition of PC reduces the

viscosity of the ionic liquid, the electrical conductivity reaches a maximum at $x_{IL} \sim 0.2-0.3$ depending on the temperature, which corresponds to a composition of 4−2.3 PC molecules for 1 EMIM TFSI, respectively. These findings will guide the selection of x_{IL} values for the mixtures that will be studied in the next chapter.

Chapter 4

This chapter will explore various aspects of tuning NP surfaces with different ligands to prepare them for transfer into solvents relevant to thermoelectric applications. The first section presents a preliminary study evaluating different ligands, providing a foundation for subsequent analyses of pH effects on the coating and adsorption experiments to study surface coverage. Additionally, the chapter will examine the effects of temperature offering preliminary insights into the mechanisms of agglomerate formation.

4. Choice of the surface ligand and properties of the modified dispersions

4.1. Preliminary tests with ligands

After tuning the NP´s surface as discussed in Section 2.2.1 with three different ligands (Table 3), chosen to evaluate the influence of both the nature of the attaching negative group and the side-chain length, the samples are transferred to EMIM TFSI, following the procedure discussed in Section 2.2.4. The colloidal stability of the samples is then evaluated through visual inspection, optical microscopy, and DLS measurements.

The samples with the ligand $SBMIM^{\pm}TFSI^{-}$ are not stable, regardless of the NP size. This outcome is unexpected, as previous research (11) demonstrated stable samples with maghemite NPs up to 200°C and over the long term for particles similar in size to APCo2. As the NPs tested in this study have a maghemite surface, the instability may be due to the cobalt ferrite core of the NPs. The Hamaker constant for cobalt ferrite ($\approx 4\times10^{-19}$ J) (108,109) is slightly higher than that for maghemite ($\approx 2.3 \times 10^{-19}$ J) (55), resulting in stronger attractive van der Waals interactions. This difference could compromise the stabilization of the core@shell NPs compared to maghemite. Additionally, cobalt ferrite NPs exhibit much higher magnetic anisotropy, potentially increasing the strength of overall attractive magnetic dipolar interactions.

While the ligand with the sulfonic attaching group fails to stabilize the NPs in EMIM TFSI, the ligand $PAC_6MIM^{\pm}Br^{-}$ successfully produces stable dispersions for all three NP sizes. However, the APCo3 sample forms a small amount of precipitate at the bottom of the flask over time. The amount of precipitate remained constant in the long run, and the supernatant was used for the DLS measurements. These dispersions consist of stable clusters of NPs with a d_H significantly smaller than that of the synthesized water-based FFs with the nitrate counter-ion.

The ligand $PAC_4MIM^{\pm}Br^{-}$ is also tested to identify the origin of the differing results, as $SBMIM^{\pm}TFSI^{-}$ and $PAC_6MIM^{\pm}Br^{-}$ differ in both their negative group that adsorbs on the NPs and their side-chain length. Stable samples are also obtained using $PAC_4MIM^{\pm}Br^{-}$ for APCo1 and APCo2. The APCo3 sample was not tested due to the time evolution discussed above. As shown in Table 9, the obtained d_H is very similar to the results for $PAC_6MIM^{\pm}Br^{-}$, suggesting that the nature of the surface-attaching group

is the most important parameter for stabilizing the NPs, rather than the side-chain length for the tested ligands.

Table 9. Hydrodynamic diameter for the three samples of NPs with different ligands dispersed in water or EMIM TFSI with ϕ_{NP} = 1.0%.

Samples	Solvent	Counter-ion/Ligand	d_h (nm)
APCo1	Water	NO_3^-	210
	EMIM TFSI	$PAC_6MIM^{\pm}Br^-$	58
		$PAC_4MIM^{\pm}Br^-$	58
APCo2	Water	NO_3^-	160
	EMIM TFSI	$PAC_6MIM^{\pm}Br^-$	58
		$PAC_4MIM^{\pm}Br^-$	67
APCo3	Water	NO_3^-	80
	EMIM TFSI	$PAC_6MIM^{\pm}Br^-$	49

A possible explanation for why the phosphonic ligand works while the sulfonic ligand does not is that the phosphonic group interacts more strongly with the oxide surface compared to the sulfonic group. In a study by Lisjak et al. (98), a ligand containing both sulfonic and phosphonic groups is tested on barium hexaferrite platelets, and it is found that the phosphonic group is the one that is effectively attached to the surface.

4.2. Influence of the pH after coating

The effect of pH on the APCo2 NPs, after coating them with the ligand $PAC_6MIM^{\pm}Br^-$, is assessed by analyzing the d_h from DLS measurements. Figure 40 presents the d_h values as a function of pH. It is important to note that the ϕ_{NP} was not constant throughout the experiment. The experimental setup involved gradually adding NaOH solution to a dispersion with an initial ϕ_{NP} = 1.0%, with d_h measurements taken from the same flask.

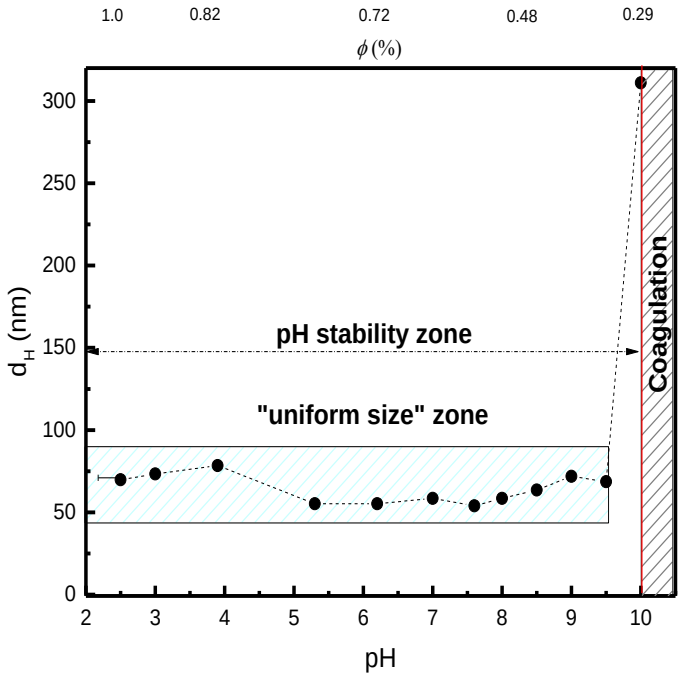

Figure 40. Hydrodynamic diameter as a function of pH for an aqueous dispersion of APCo2 NPs coated with $PAC_6MIM^{\pm}$.

As shown in Figure 40, the sample remains colloidally stable with minimal variation in d_h until approximately pH 9. This stability cannot be achieved with the precursor water-based FF. As illustrated in Figure 20, at near-neutral pH, the surface sites are mostly amphiphilic, resulting in insufficient charge density to ensure repulsive interactions between the NPs, leading to sample flocculation. The stability observed after the $PAC_6MIM^{\pm}$ coating is likely due to the positive charge introduced by the imidazolium moiety of the ligand, which does not have acid-base properties and remains unaffected by changes in pH. This suggests that a significant amount of $PAC_6MIM^{\pm}$, if not all, remains adsorbed even when highly diluted with NaOH solution. This is indicative that the surface coverage is robust and stable.

The flocculation observed in the sample shown in the figure can be attributed to two factors: the drastic increase in ionic strength, which compresses the electric double layer and promotes agglomeration phenomena, and the possible desorption of the $PAC_6MIM^{\pm}$ groups from the NP surface, potentially caused by the excess of OH^- ions. Although desorption experiments were not performed in this study, the primary cause of the flocculation is probably the significant increase in ionic strength as the pH rises from ~2 to 9. The literature reports that the linkage of phosphonic groups with iron

oxide surfaces is strong, primarily forming through chemisorption (110). Consequently, it is improbable for hydroxide ions, even in excess, to displace the phosphonic group.

4.3. Adsorption experiments

The results obtained from the preliminary ligands study and the influence of the pH suggest that the ligands adsorb onto the NP surface. Thus, adsorption isotherms for $PAC_6MIM^{\pm}$ and Br^- are obtained following the procedure described in Section 2.2.3.

The amounts of $PAC_6MIM^{\pm}$ and Br^- adsorbed on the NPs at equilibrium (Q_e mmol/g) are calculated from their initial (C_0) and equilibrium (C_e) concentrations (mmol/L) through the Equation 39.

$$Q_e = \frac{(C_0 - C_e)}{m} V \tag{39}$$

Where V is the volume of the dispersion and m is the mass NPs, calculated from the density and volume fraction of the FF.

Considering the NPs as hard spheres, the number of ions per unit of NPs surface is obtained by the surface coverage calculation presented in the Appendix.

In Figure 41, the equilibrium adsorption curves for $PAC_6MIM^{\pm}$ and Br^- at 80 °C are depicted, where a maximal adsorption capacity of approximately 0.5 mmol/g for $PAC_6MIM^{\pm}$ and 2.25 mmol/g for Br^- is obtained. It corresponds to a surface coverage of ≈ 2.3 $PAC_6MIM^{\pm}/nm^2$ and ≈ 10.5 Br^-/nm^2. This saturation regime is reached for an initial ligand concentration ≥ 50 mmol/L.

For the unheated sample, the surface coverage is approximately 1.7 $PAC_6MIM^{\pm}/nm^2$, indicating that temperature has a minimal impact on $PAC_6MIM^{\pm}$ adsorption within the studied range. In contrast, the coverage for Br^- is about 1.1 Br^-/nm^2 without heating. This reduction may be due to bromide ions primarily forming outer-sphere complexes with oxide surfaces, making the adsorption process more sensitive to temperature changes (111).

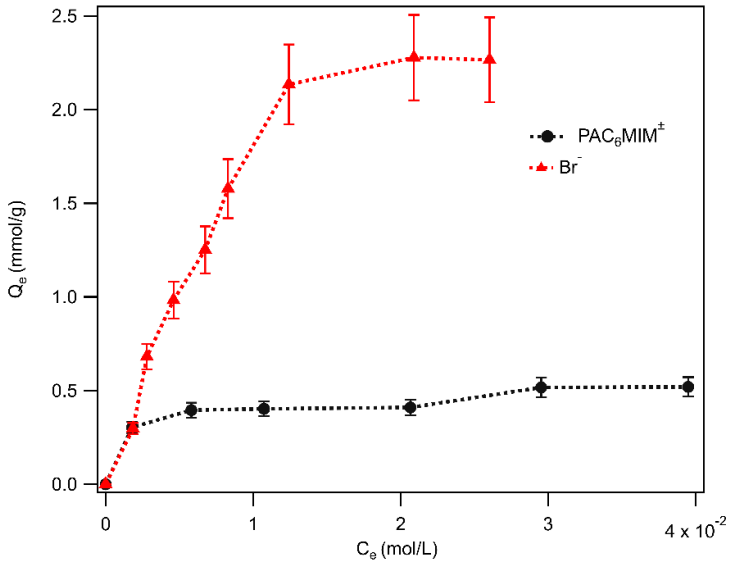

Figure 41. Adsorption curves isotherms of $PAC_6MIM^{\pm}$ and Br^- onto the APCo2 NPs dispersed in water.

Regarding the results of the leaching tests, Figure 42 shows the mass fraction percentage of leached iron and cobalt ions as a function of the initial $PAC_6MIM^{\pm}Br^-$ concentration for the heated samples and one unheated. The ratio $PAC_6MIM^{\pm}Br^-$/Fe is the same in the two red squares.

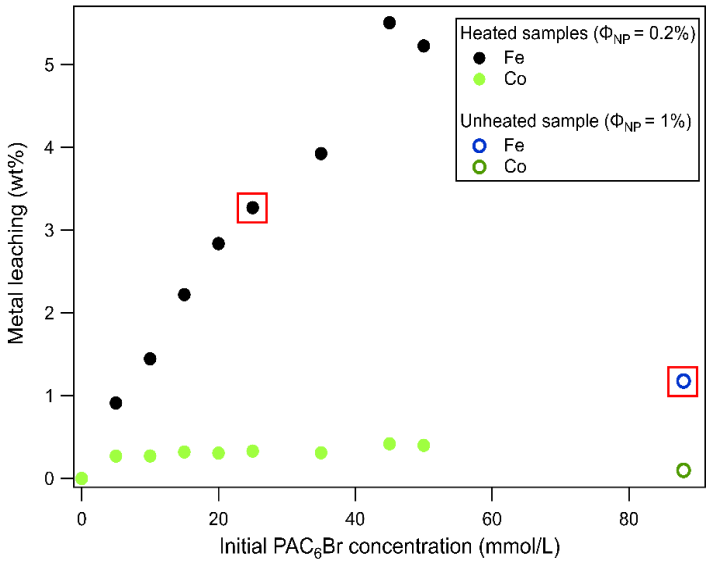

Figure 42. Mass fraction percentage of leached iron and cobalt ions per NP as a function of the initial $PAC_6MIM^{\pm}Br^-$ concentration.

As shown in Figure 42, overall, the leaching of iron rises with increasing $PAC_6MIM^{\pm}Br^{-}$ concentration. At lower ligand concentrations, this relationship is linear. Thus, the functionalization of iron oxide-based NPs with phosphonic ligands in acidic media can lead to partial dissolution of the particle surface. This phenomenon is primarily due to the strong chemical interaction between surface iron ions and phosphonate groups (110), and it can be influenced by the temperature at which the coating process is conducted.

For cobalt, leaching is significantly lower than that of iron across all samples and remains relatively constant as $PAC_6MIM^{\pm}Br^{-}$ concentration increases. This behavior may be due to cobalt being less accessible, as it is situated in the core of the particles beneath the iron-rich outer layer.

Comparing the heated and unheated samples with the same ratios of $PAC_6MIM^{\pm}Br^{-}$ concentration and NP mass (red squares), the impact of the temperature is evaluated. The findings indicate that NPs coated at 80°C release approximately three times more iron than those coated at room temperature. From these results, it can be concluded that coating NPs at higher temperatures increases leaching but does not significantly enhance surface coverage with $PAC_6MIM^{\pm}Br^{-}$. Therefore, in subsequent experiments involving the preparation of samples in EMIM TFSI, PC, and their binary mixtures, the functionalization of the NPs is conducted at room temperature following Riedl's method (11) to minimize iron leaching.

To assess the coating stability post-transfer to the IL, the amounts of $PAC_6MIM^{\pm}$ and Br^{-} are determined around the APCo2 NPs after ultracentrifugation of the dispersions as presented in Section 2.2.4, resulting in a concentration of 0.52 and 0.06 mmol/g, respectively for $PAC_6MIM^{\pm}$ and Br^{-}. This surface coverage corresponds to ≈ 2.4 $PAC_6MIM^{\pm}/nm^2$ and ≈ 0.3 Br^{-}/nm^2, which is very close to the limit adsorption capacity for $PAC_6MIM^{\pm}$ in water at 80°C, but much lower for Br^{-}, which seems to desorb from the solid/liquid interface in the IL. These results indicate that the coating with $PAC_6MIM^{\pm}$ is robust and improves in EMIM TFSI medium.

In summary, the $PAC_6MIM^{\pm}Br^{-}$ concentration used in Riedl's method (~75 mmol/L) is sufficient to achieve a surface coverage in EMIM TFSI that closely approaches the maximum value obtained at 80°C, with minimal impact from iron leaching.

4.4. Thermal stability of IL-based samples

The effect of the thermal stability of the samples is evaluated for APCo1 and APCo2 dispersed in EMIM TFSI NPs with the ligands $PAC_6MIM^{\pm}Br^-$ and $PAC_4MIM^{\pm}Br^-$, following the procedure presented in Section 2.2.7. The d_h are presented in Table 10.

Table 10. Hydrodynamic diameter as a function of the temperature for APCo1 and APCo2 coated with $PAC_4MIM^{\pm}$ and $PAC_6MIM^{\pm}$ dispersed in EMIM TFSI at a ϕ_{NP} = 1.0%.

Temperature (ºC) ligand	d_h (nm)			
	APCo1		**APCo2**	
	$PAC_4MIM^{\pm}$	$PAC_6MIM^{\pm}$	$PAC_4MIM^{\pm}$	$PAC_6MIM^{\pm}$
Room Temperature	85	94	67	57
50	81	84	62	55
100	65	72	59	52
150	57	44	48	44
200	49	39	43	40

The samples maintain colloidal stability as the temperature increases, and a decrease in d_h is observed for all samples. While the samples still consist of aggregates, these become smaller at higher temperatures. Notably, the d_h of the APCo1 and APCo2 samples converge at elevated temperatures, despite differences in their individual NPs.

These results suggest that thermal energy effectively breaks up agglomerates, indicating that the formation of these aggregates is likely governed by a reversible mechanism.

4.5. Summary

This chapter evaluates NP surface tuning using three different ligands. The ligand $SBMIM^{\pm}TFSI^-$ fails to stabilize dispersions, even though it has successfully stabilized similarly sized maghemite NPs in previous studies. In contrast,

$PAC_6MIM^{\pm}Br^{-}$ successfully stabilizes NPs across all sizes in EMIM TFSI, with only some precipitation in the largest sample. These dispersions consist of stable clusters of NPs with a d_h significantly smaller than that of the synthesized water-based FFs. $PAC_4MIM^{\pm}Br^{-}$ also stabilizes APCo1 and APCo2 NPs, highlighting the importance of the attaching group over side-chain length. $PAC_6MIM^{\pm}$ maintains stability up to pH ≈ 9 in water and provides robust surface coverage. Higher coating temperatures increase iron leaching without significantly improving coverage. Finally, thermal stability studies for APCo1 and APCo2 NPs dispersed in the ionic liquid indicated that the samples remained colloidally stable, with agglomerates breaking up as the temperature increased.

Chapter 5

In this chapter, the discussion will focus on the behavior of NPs in different solvents. The analysis will begin with dispersions in water, followed by those in pure EMIM TFSI and PC, and conclude with dispersions in a mixture of these two solvents. A complementary discussion will address the impact of residual water in these systems on NP behavior. Finally, the chapter will examine the effects of pumping and heating across the different solvents.

5. Colloidal stability and nanostructure: from water to ionic liquid-based solvents

5.1. Dispersions in water

The dispersions in water are the initial state of the NPs after their synthesis in aqueous media. The acidic NPs with nitrate counterions of these precursor samples (see section 2.1) are then modified by adsorption of the $PAC_6MIM^{\pm}$ molecule (section 2.2.1), which leads to positively charged NPs in acidic aqueous medium, with bromide counterions. These dispersions look stable by eye and the nanostructure is firstly studied by DLS. The d_h results are summarized in Table 11.

Table 11. Hydrodynamic diameter for the three sizes of NPs coated with $PAC_6MIM^{\pm}$ and dispersed in water with a ϕ_{NP} = 1.0%.

Sample	**d_h (nm)**
APCo1	101
APCo2	72
APCo3	47

Similar to the precursor samples, the $PAC_6MIM^{\pm}$-coated NPs consist of clusters, with cluster size increasing as the diameter of the NPs decreases, for the same reasons discussed in Section 3.3. However, the size of these clusters is significantly smaller compared to the precursor samples (see Table 8). This suggests that the $PAC_6MIM^{\pm}$ functionalization improves colloidal stability, likely due to steric contribution to stabilization provided by the molecular structure of the ligands.

To further support the DLS data, SAXS measurement curves are obtained at varying ϕ_{NP} from 0.1% to 3% for the three NP sizes, as shown in Figures 43, 44 and 45 for APCo1, APCo2 and APCo3, respectively. The aim is to get information both on the size of the dispersed objects and their interactions.

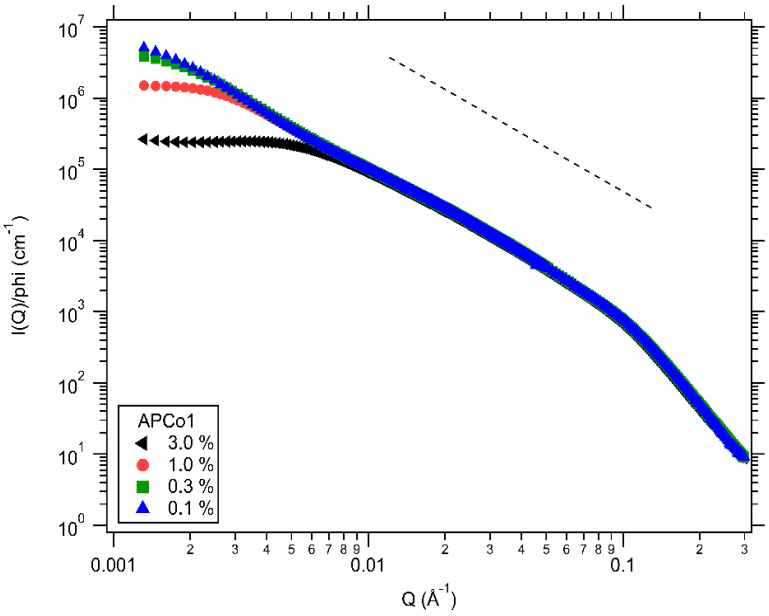

Figure 43. Scattering profile in absolute scale normalized by the volume fraction of NPs for APCo1 dispersed in water with $PAC_6MIM^{\pm}$ coating. The dotted line indicates a Q^{-2} law.

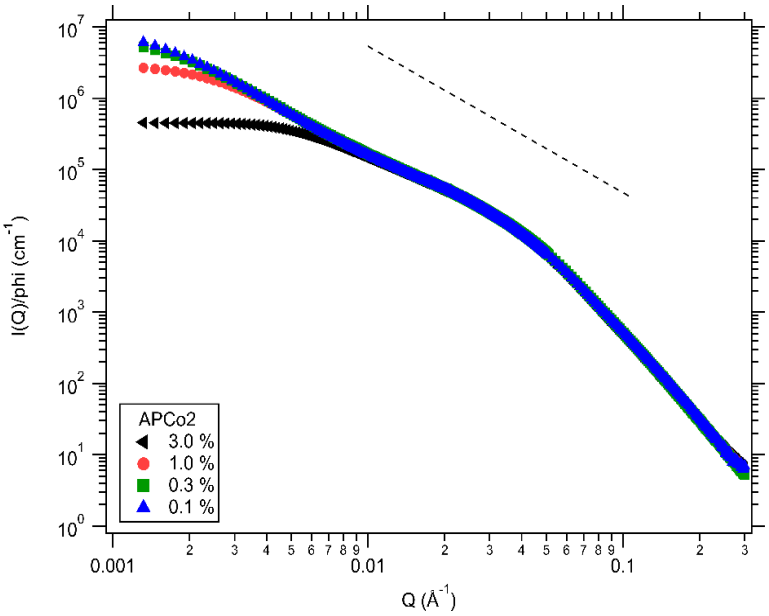

Figure 44. Scattering profile in absolute scale normalized by the volume fraction of NPs for APCo2 dispersed in water with $PAC_6MIM^{\pm}$ coating. The dotted line indicates a Q^{-2} law.

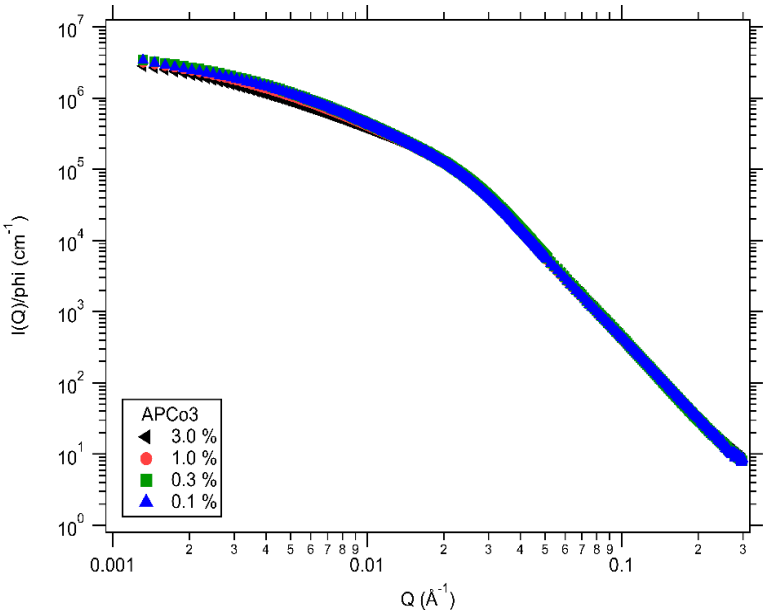

Figure 45. Scattering profile in absolute scale normalized by the volume fraction of NPs for APCo3 dispersed in water with $PAC_6MIM^{\pm}$ coating.

APCo1 and APCo2 have rather close behaviours in terms of shape of the curves as well as influence of the volume fraction. However APCo3 differs. Nevertheless, whatever the mean size of the NPs, the intensities for the lowest volume fraction, for which the interobjects interaction is negligible, cannot be fitted by a lognormal distribution. The R_g determined from these dilute samples (see calculation details in the Appendix) are given in Table 12. It evidences aggregates, larger for the smaller particles, corroborating the findings obtained from the DLS measurements at ϕ_{NP} =1%.

Table 12. R_g for the three NPs sizes dispersed in water with $PAC_6MIM^{\pm}$ as ligand, determined on dilute dispersions (ϕ_{NP}=0.1%) and aggregation number deduced from R_g and Figure 46.

Sample	**Rg (nm)**	**N_{agg}**
APCo1	61	~25
APCo2	55	~20
APCo3	36	

In samples APCo1 and APCo2, the scattered intensities vary as Q^{-2} in the intermediate Q range, which indicates fractal aggregates with a fractal dimension of 2.

Such clusters have already been observed in aqueous dispersions rather similar to these samples while varying the pH and the salt concentration (112). They were issued from the Reaction Limited Colloidal Aggregation (RLCA), a universal process independent on the detailed nature of the system.

In the case of APCo3 samples, the NPs are significantly larger, which allows them to form chains and loops due to the high value of the dipolar magnetic interaction parameter (113). This results in a markedly different behavior compared to the other samples.

The Figure 3 left of the previous study (112) is reproduced in Figure 46: it plots the R_g as a function of the aggregation number N_{agg}, both determined from SAXS intensities. The N_{agg} values determined with this graph and the R_g determined are given in Table 12 and show aggregates of a few dozen of NPs.

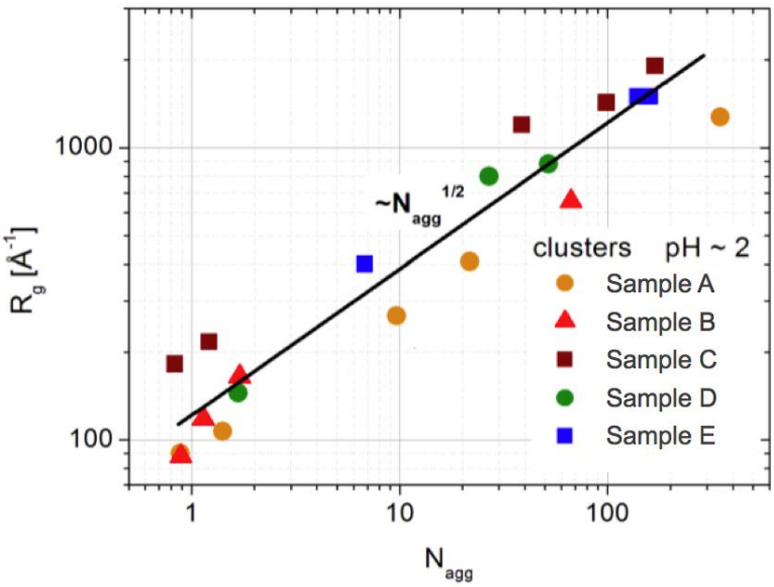

Figure 46. Rg as a function of Nagg at approximately pH 2. Samples A, B, and C represent maghemite NPs, while samples D and E correspond to cobalt ferrite NPs.

When the NPs' volume fraction is increased, the intensity scattered at low Q decreases, which indicates repulsive interaction between the clusters, within the hypothesis that these clusters do not depend on dilution.

These modified dispersions are thus qualitatively similar to the precursor ones however the clusters' sizes are reduced during the modification process.

5.2. Dispersions in pure EMIM TFSI

The samples in the ionic liquid EMIM TFSI are produced by a transfer without drying: water is added, the particles move through the interface towards the ionic liquid and water is removed by pumping. The composition is thus kept after transfer. The same type of analysis is applied, beginning with DLS before performing SAXS.

The size of the clusters further decreases compared with the samples in water and it decreases more significantly as the individual NPs become smaller, as confirmed by both DLS (see the d_h in Table 13) and SAXS measurements, shown on Figure 47, 48 and 49 for APCo1, APCo2 and APCo3, respectively. The R_g determined from the dilute measurements are also gathered in Table 13, showing very similar sizes across the different samples. According to Figure 46, these R_g correspond to small aggregates of few particles, as reported in Table 13.

Table 13. Sizes obtained either from DLS (d_h) on Φ_{NP} = 1% dispersions or from SAXS (R_g) on Φ_{NP} = 0.1% EMIM TFSI dispersions with $PAC_6MIM^{\pm}$ coating.

Sample	**d_h (nm)**	**R_g (nm)**	**Nagg**
APCo1	59	29	~4
APCo2	50	26	~3
APCo3	45	28	

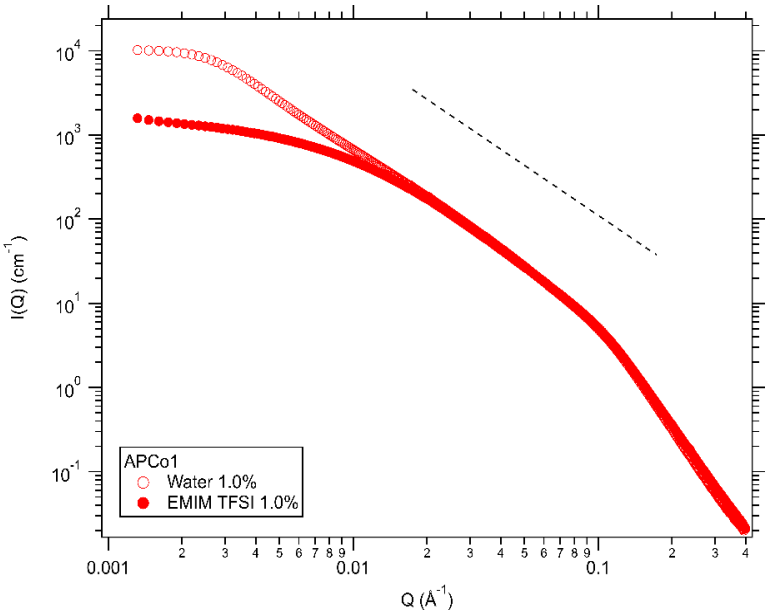

Figure 47. Scattering profile in absolute scale normalized by the volume fraction of APCo1 NPs with $PAC_6MIM^{\pm}$ coating dispersed in water and EMIM TFSI for ϕ_{NP}=1.0%.

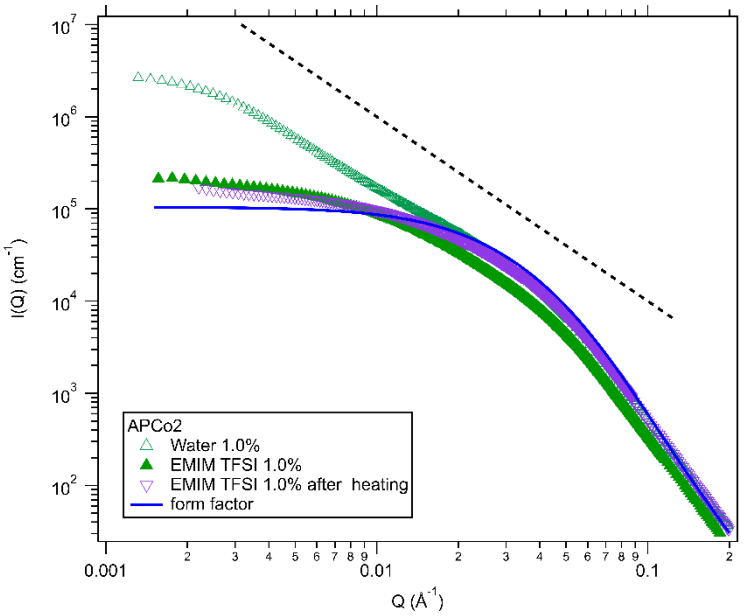

Figure 48. Scattering profile in absolute scale normalized by the volume fraction of APCo2 NPs with $PAC_6MIM^{\pm}$ coating dispersed in water, EMIM TFSI, and EMIM TFSI sample after heating for ϕ_{NP}=1%. Possible form factor (see text for details).

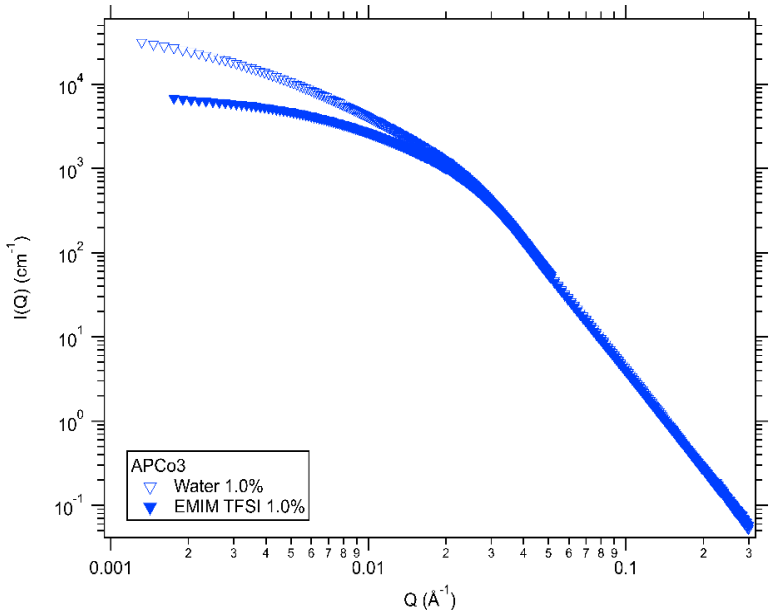

Figure 49. Scattering profile in absolute scale normalized by the volume fraction of APCo3 NPs with $PAC_6MIM^{\pm}$ coating dispersed in water and EMIM TFSI for ϕ_{NP}=1.0%.

Although the clusters are much smaller than in water, the scattered intensities do not correspond to the form factor of the NPs. As the tests done in DLS showed a decrease of d_h in the ionic liquid after a heating step of the dispersions, SAXS measurements were conducted on the APCo2 sample after heating it at 150°C for two hours in a closed vessel (purple inverted triangles in Figure 48). The results indicate that heating contributes to the breaking of NP clusters reducing further the Rg from 26 nm to 13 nm (obtained from diluted samples at ϕ_{NP} = 1.0%), making this sample the closest to yielding a form factor. It corresponds to N_{agg} less than 2 and the sample is stable at least for one year according to SAXS repeated over time (not shown).

Therefore, a possible form factor can be proposed based on the intensities at large q values and producing lower intensities at low Q than the heated sample in EMIM TFSI (see Figure 48). It is calculated with a lognormal distribution with d_0 = 5 nm and sigma = 0.45. By comparing the intensities at low q of this form factor with the most dilute sample in water, an approximate aggregation number (N_{agg}) of 40 to 50 can be estimated for APCo2. This value is reasonable compared with the values extracted thanks to previous data and reported in Table 12.

Figure 50, 51 and 52 show the scattered intensities for a range of volume fractions for the ionic liquid dispersions. The curves are very close, which means that

the interobjects interaction appear to be very weak. It is important to note that APCo3 dispersions are not fully stable at ϕ_{NP} = 1%, as a small precipitate gradually forms over time. This is consistent with previous studies that showed the difficulty of stabilizing larger particles at large concentrations (114). For APCo2, the interobjects interation appear slightly repulsive within the hypothesis on clustering independent of the volume fraction.

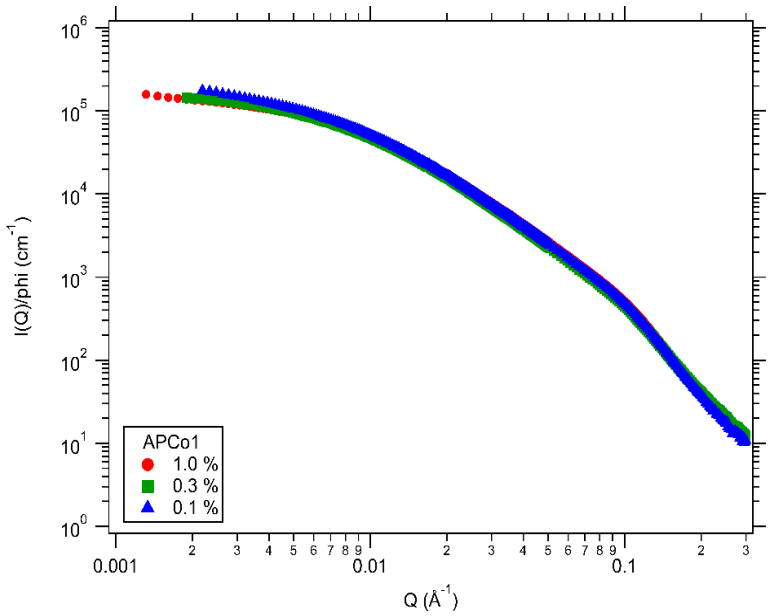

Figure 50. Scattering profile in absolute scale normalized by the volume fraction of NPs for APCo1 dispersed in EMIM TFSI with $PAC_6MIM^{\pm}$ coating at several volume fractions.

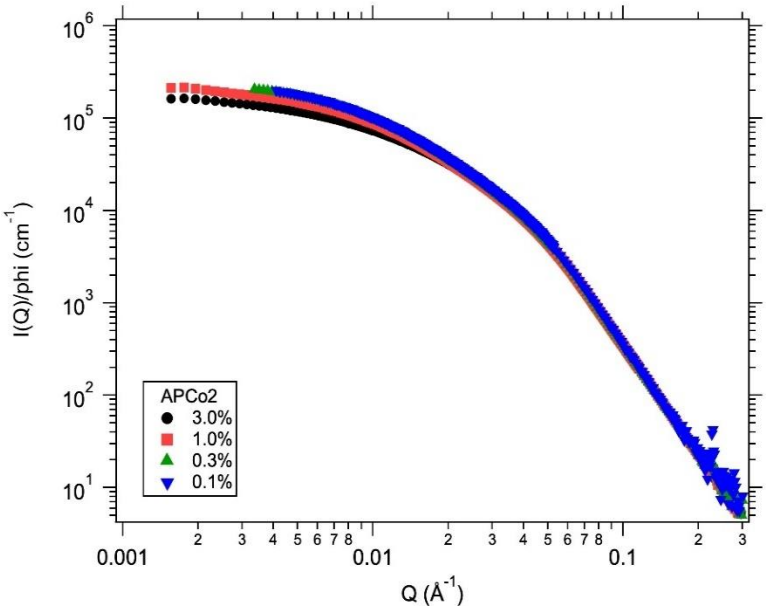

Figure 51. Scattering profile in absolute scale normalized by the volume fraction of NPs for APCo2 dispersed in EMIM TFSI with $PAC_6MIM^{\pm}$ coating at several volume fractions.

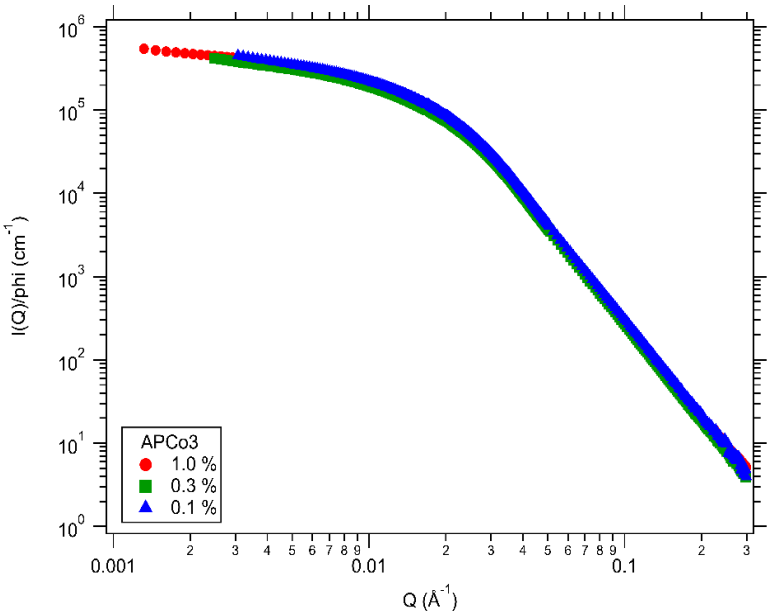

Figure 52. Scattering profile in absolute scale normalized by the volume fraction of NPs for APCo3 dispersed in EMIM TFSI with $PAC_6MIM^{\pm}$ coating at several volume fractions.

5.3. Dispersions in pure PC

Dispersions in pure PC cannot be produced as in EMIM TFSI because PC is removed by pumping contrary to EMIM TFSI. Two different routes can be used to transfer the particles from water to PC and were tested on APCo2 NPs on samples with ϕ_{NP} = 1.0%.

Route 1 Following the $PAC_6MIM^{\pm}$ coating process, PC is directly added to the NP water dispersion, and the water is then slowly evaporated at a temperature above 100°C. This method is initially attempted as a wet route to keep the particles always dispersed. However, this route failed therefore a second approach was attempted.

Route 2: Following the the $PAC_6MIM^{\pm}$ coating process, water is removed through vacuum pumping. PC is then added to the dried state obtained, and the NPs are redispersed in PC by heating the sample at 80°C for a few minutes, as detailed in Section 2.2.4.

According to DLS, Route 1 produces very big clusters close to 1 micron although Route 2 produces much smaller ones around 50 nm. SAXS, shown in Figure 53, evidences more agglomerates with Route 1 than Route 2 but not as big as DLS. This is due to a change in viscosity following Route 1, likely due to the opening of the carbon ring, as observed in this family of molecules (99), and further exacerbated by the presence of oxide NPs. Therefore, only route 2 can be used. The quality of the sample can be further enhanced by heating it at 150 °C for two hours, as shown in Figure 53.

As for the transfer to EMIM TFSI, the clusters are highly reduced compared with the initial sample in water, nevertheless the remaining clusters are bigger than in the dispersions in EMIM TFSI heated in the same way.

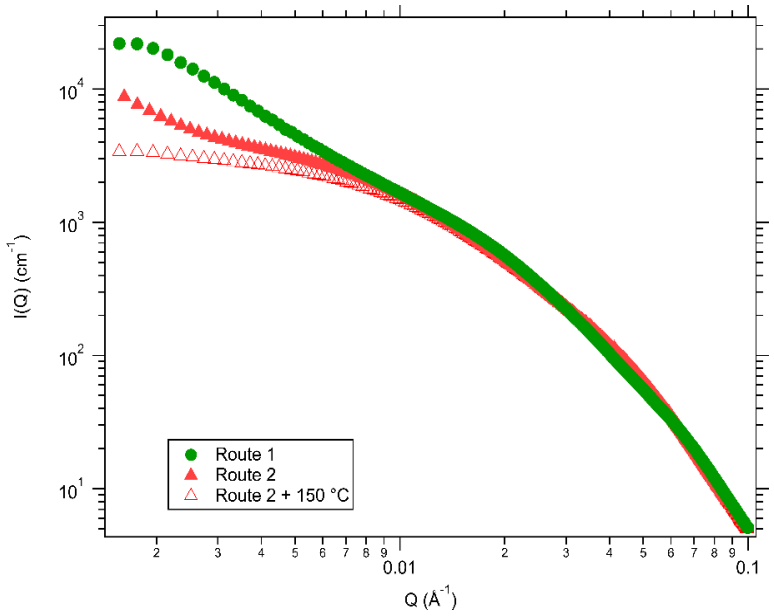

Figure 53. Scattering profile in absolute scale for different routes preparation of the pure PC dispersions for APCo2 NPs at ϕ_{NP}=1.0%.

5.4. Dispersions in mixtures of EMIM TFSI and PC

To avoid a drying step, the mixtures were not produced by a simple mixing of dispersions at the same volume fraction in the pure solvents but by a mixture of a concentrated EMIM TFSI dispersion at ϕ_{NP} = 3.0% with PC and EMIM TFSI in order to reach a ϕ_{NP} = 1.0% with the chosen composition, at room temperature. The proportions of the solvent mixtures were chosen according to the conductivity measurements (see Figure 39). The mole fraction of ionic liquid x_{IL} =0.25 is chosen because it is close to the maximum of the conductivity. One lower fraction and two higher fractions are added to explore the range of compositions. The composition in different units are given in Table 14.

Table 14. Compositions of the mixtures of EMIM TFSI (IL) and PC used, in different units. Mole fraction x_{IL}, Volume fraction ϕ_{IL}, mass fraction w_{IL}, concentration of IL c_{IL}, concentration of PC c_{PC}, number of molecules of PC for one molecule of IL PC:IL.

x_{IL}	**0**	**0.14**	**0.25**	**0.35**	**0.67**	**1**
ϕ_{IL}	0	0.32	0.5	0.62	0.85	1
w_{IL}	0	0.38	0.56	0.66	0.88	1
c_{IL} **(mol/L)**	0	1.27	1.95	2.4	3.34	3.88
c_{PC} **(mol/L)**	11.7	7.9	5.8	4.5	1.65	0
PC:IL		5.9:1	3:1	1.9:1	1:1	0:1

The lowest x_{IL} already corresponds to a high salt concentration of 1.27 mol/L in the solvent. The maximum conductivity is obtained for 3 molecules of solvent for one ion pair. The 1:1 situation is also explored.

All the FF samples prepared from mixtures of EMIM TFSI and PC appeared visually stable across the full range of tested x_{IL} values. In Figure 54, the correlation functions from DLS are plotted as a function of $t \cdot q^2/\eta$, where q is the scattering vector and η the viscosity of the solvent. This approach removes the influence of refractive index and viscosity differences across solvents. Consequently, any shifts between the curves reflect differences in the apparent sizes of the particles. Two series of data are plotted: the samples as prepared at room temperature and the same samples after a heating step of 2 hours at 150°C. The results indicate a decrease in the apparent d_h after the heating step whatever the composition, as the correlation functions with empty symbols consistently appear to the left of those with full symbols, with the largest shift observed for pure PC. Additionally, the long-time tail of the correlation function for pure EMIM TFSI, which suggests the presence of larger clusters, disappears after heating. However the shift after heating is random, which is consistent with the apparent sizes observed before heating. No trend appears with the composition. On the contrary, after heating, the apparent size increases with the amount of PC in the mixture (see d_h values in Table 14).

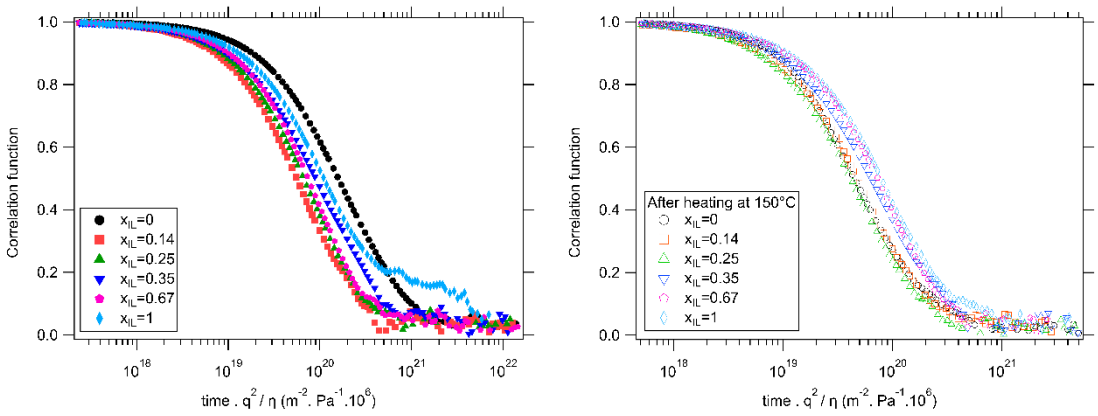

Figure 54. Correlation function for all samples in the mixtures EMIM TFSI/PC with APCo2 NPs, before and after heating, for ϕ_{NP}=1.0%, with a rescaled X-axis in order to compare the different solvents removing the effect of the variation of refractive index and viscosity.

These observations are further supported by SAXS data showing the same two series of samples as in DLS. In Figure 55, the rescaled SAXS scattered intensities are superimposed on large q's, which shows that the individual NPs are not modified. Interestingly, adding PC in EMIM TFSI creates some clusters, evidenced by the low q upturn, as in pure PC obtained with the dried NPs. The curves evidence the presence of agglomerates at low q´s, which are decreased in size after heating at 150 °C for 2 hours, as shown more clearly in the zoomed-in view of the low q region (Figure 56). As with the pure solvents, the heating step enhances the dispersion of the NPs by breaking up small clusters.

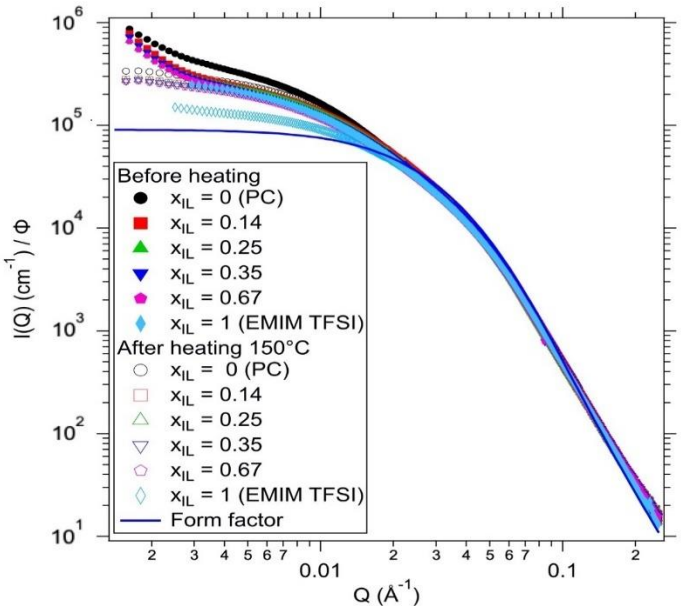

Figure 55. Scattered intensity profile in absolute scale rescaled with the contrast of PC for all samples in the mixtures EMIM TFSI/PC with APCo2 NPs, before and after heating, for ΦNP=1%. *x*IL is the mole fraction of ionic liquid in the mixture.

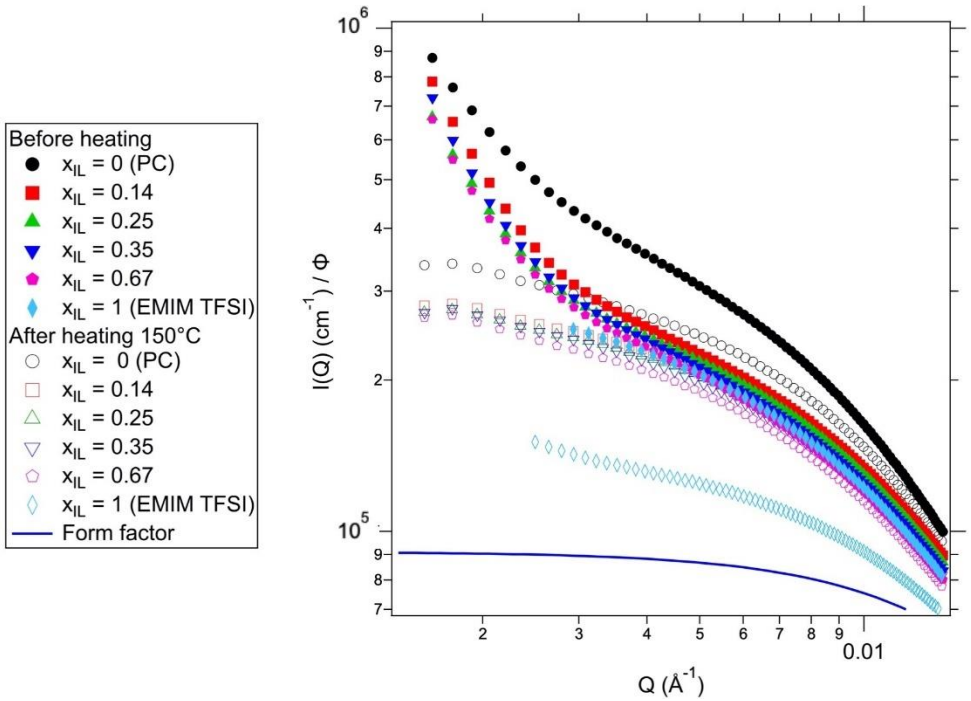

Figure 56. compares SAXS intensities at NP concentrations of 1 vol% and 0.1 vol%, evidencing repulsive interactions between the NPs, assuming that the clusters remain unchanged by dilution.

Figure 57 compares the scattering profiles for different mixture compositions at two dilution levels. The higher intensity of the more diluted sample curves suggests

that, if the clusters remain unchanged by dilution, the interparticle interactions are likely repulsive. However the R_g determined from the dilute samples in the mixures are not consistent with the apparent d_h determined from DLS (see Table 15). D_h increases with the IL fraction while R_g decreases. These two sizes are not determined at the same volume fraction, as d_h is obtained with ϕ_{NP}=1.0% while R_g is obtained with ϕ_{NP}=0.1%, therefore interparticle interaction can have some influence. For repulsive interaction, the apparent d_h would indeed be larger at lower concentration. To reconcile d_h and R_g, interactions in pure PC should be much larger than in pure EMIM TFSI. Another explanation could be a change of the clusters upon dilution. Separating the two effects cluster size and interactions is not an easy task and would need more investigations.

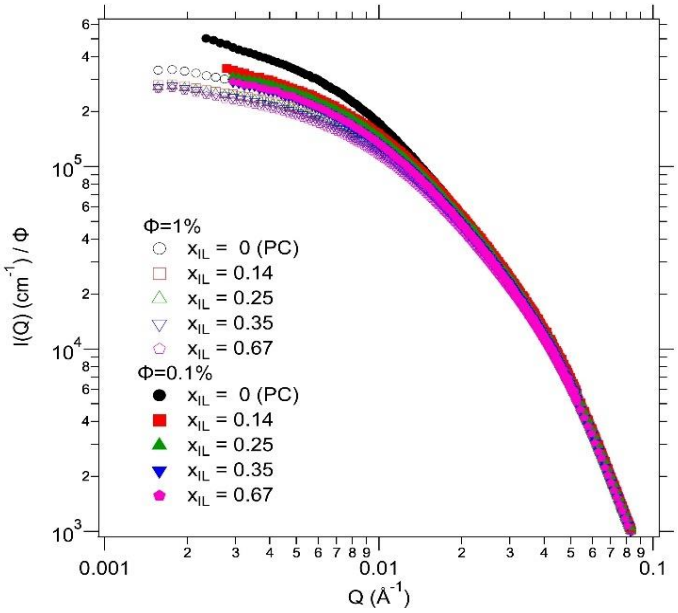

Figure 57. Scattering profiles normalized by the volume fraction, for APCo2 NPs coated with PAC_6MIM coating in the different mixtures of solvents.

Table 15. Hydrodynamic diameter determined with ϕ_{NP}=1%, and R_g determined with ϕ_{NP}=0.1%, for the dispersions in the different solvent compositions after heating at 150°C.

χ_{IL}	d_h (nm)	R_g (nm)
0 (pure PC)	25	19
0.14	26	17
0.25	23	14
0.35	33	14
0.67	41	14
1 (pure EMIM TFSI)	43	13

These experiments have shown that stable dispersions of rather small clusters of few particles can be obtained in all tested mixtures of EMIM TFSI and PC, which was not obvious. The reduction of the clusters' sizes after heating suggests that these dispersions are compatible with high-temperature application conditions.

5.5. Remaining water in the non aqueous solvents

One possible explanation for cluster formation upon adding PC to EMIM TFSI before heating could be the presence of residual water in the samples. Even a small amount of water can significantly impact the properties, especially at the solid/solvent interface (115). Although EMIM TFSI is relatively hydrophobic, it can still dissolve some water, whereas PC is much more hygroscopic (116).

The water content is determined by heating the sample at 150°C in a furnace connected to a Karl Fischer electrochemical cell, as described in Section 2.2.8. Only the water is introduced in the electrochemical cell, which suppresses the interactions with the other components, in particular the NPs. The results, presented in Table 16, are provided in ppm (a classical unit), weight percentage, and volume percentage to allow for comparison between different solvents while accounting for density differences.

Table 16. Results from the Karl-Fisher titrations of the water extracted in a furnace at 150°C.

Sample	ppm	Weight %	Vol %
PC	10	0.001	0.0012
EMIM TFSI	43	0.0043	0.0065
EMIM TFSI H_2O saturated	7500	0.75	1.13
EMIM TFSI H_2O saturated redried	744	0.074	0.112
NPs+$PAC_6MIM^{\pm}$ in EMIM TFSI (after pumping)	800	0.08	0.12
Dried NPs+ $PAC_6MIM^{\pm}$ in PC	1800	0.23	0.27

The first section of the table lists the raw solvents. In the second, pure EMIM TFSI is mixed with water for 24 hours, and the sample labeled "EMIM TFSI H_2O saturated redried" refers to this saturated ionic liquid after being pumped to remove water (0.0031 mbar, 24 hours, room temperature). The third section presents the water content in the IL dispersions with $PAC_6MIM^{\pm}$ as ligand after pumping, and the PC dispersion, produced as described in Section 2.2.4.

The original solvents are rather dry. However, after 24 hours of stirring with water, EMIM TFSI absorbs 1.13 vol% of water, equivalent to 0.63 mol/L or approximately one water molecule for every six EMIM TFSI molecules. When this mixture is subsequently pumped, the water content decreases to 0.112 vol%, corresponding to about one water molecule for every sixty EMIM TFSI molecules, much less than in the original ionic liquid. During the transfer of particles to the ionic liquid, EMIM TFSI is also mixed with a water phase, the acidic aqueous dispersion of coated NPs. The water is removed by pumping in the same conditions as for the experiment described above without NPs. The final water content of 0.12 vol% in the obtained dispersion is very close to the latter value, indicating that the water remaining

in the dispersion primarily originates from the solvent, with minimal water retention by the NPs. In contrast, when the particles are transferred to PC, they are first dried before adding the solvent. In this case, the final water content is higher, mainly originating from the NPs, as the PC itself is very dry. It also means that this water trapped around the NPs and not removed by drying is removed in the ionic liquid. In other words, if the dried NPs were dispersed in the pure ionic liquid redried, the volume fraction of water would be 0.39%.

For the solvent mixtures, adding PC and EMIM TFSI to the concentrated EMIM TFSI-based colloidal dispersion reduces the water content because the pure solvents contains very little water. Thus, it is unlikely that water is the cause of aggregation in the mixtures, especially since the water content in the dispersion in pure PC is higher than in the dispersions in the mixtures. Although heating at 150°C improves dispersion, the samples are heated in sealed bottles, preventing water from escaping. Therefore, the observed changes after heating cannot be attributed to water content. Instead, these changes likely result from a reorganization of the solid/liquid interface at high temperatures, whether or not water is involved.

5.6. More insights into the clustering

Based on the experiments and results presented in this work, it can be concluded that the core@shell cobalt ferrite NPs consistently form clusters, with two distinct types identified. The larger clusters, consisting of a few dozen NPs, are reversible, while the smallest clusters observed in the best samples could not be broken down by any of the methods used in this study. This is rather different from maghemite NPs in the same range of sizes, treated with the same processes and methods (see Riedl *et al*. (11)). Given that the surface of the core@shell NPs is iron oxide, this difference is quite surprising. Van der Waals interactions can nevertheless differ as the Hamaker constant is higher for cobalt ferrite and the magnetic interaction can also differ due to the higher anisotropy constant of cobalt ferrite.

Several treatments seem to reduce cluster size, including the adsorption of $PAC_6MIM^{\pm}$ ligands, the transfer to solvents with water removal via pumping, and a heating step at high temperatures. Notably, the ability to redisperse the dried NPs in PC, with fewer clusters than in water, was unexpected, especially when compared to results

with maghemite and other oxides, where removing water typically led to a powder that could not be redispersed. The influence of this pumping step was thus explored more precisely.

5.6.1 Pumping in water

A pumping step similar to the one used for the transfer to EMIM TFSI or to PC was used to produce powders from water dispersions that were later rehydrated. This was applied to the NPs coated by $PAC_6MIM^{\pm}$ and to the precursor samples. The data from DLS are plotted for APCo1, APCo2 and APCo3 on the Figures 58, 59 and 60 respectively. For both APCo1 and APCo2, the dried NPs can be redispersed and the pumping significantly reduces the apparent sizes seen, for both types of water based dispersions. The difference appears when heating the dried powders: $PAC_6MIM^{\pm}$ coated NPs can be redispersed after the KF titration, that removes water at 150°C, while the precursor NPs (bare particles with nitrate counterions) cannot be redispersed. Note that these latter NPs can also not be redispersed after several weeks in the dry state, contrary to the coated ones. For these coated NPs, the apparent size further decreases after heating the powder (Dried $PAC_6MIM^{\pm}$ coated NPs after KF titration in the figures), and after pumping a second time to remove the water again (Dried $PAC_6MIM^{\pm}$ coated NPs after KF titration and 2^{nd} drying in the figures). For the biggest NPs, i.e. APCo3, the results are similar except for the first pumping with no heating treatment, which only very slightly decreases the clusters' size (Figure 60). This points towards a different origin of the clusters in this latter sample.

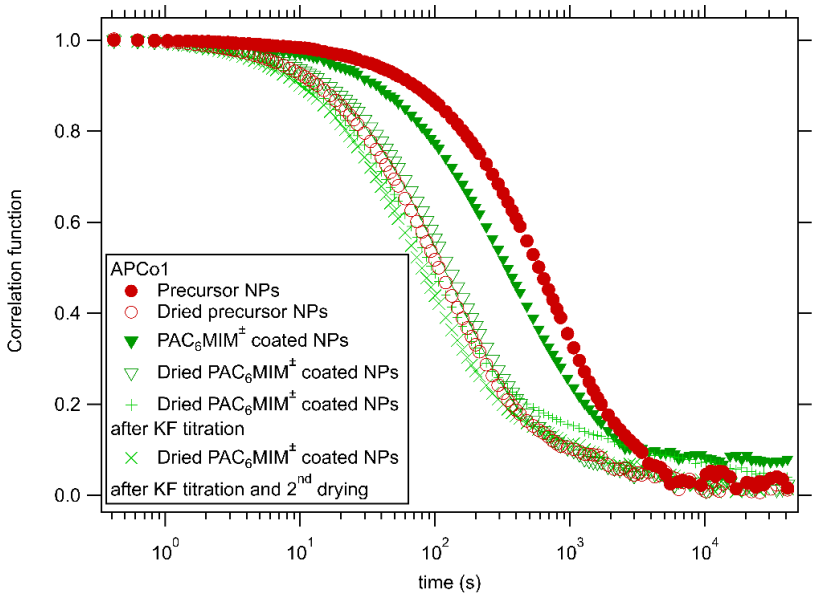

Figure 58. DLS curves for APCo1 NP samples before and after drying. All dried samples were redispersed in water at a ϕ_{NP} = 1.0%. The $PAC_6MIM^{\pm}$-coated NPs were additionally subjected to Karl Fischer titration and a second pumping cycle.

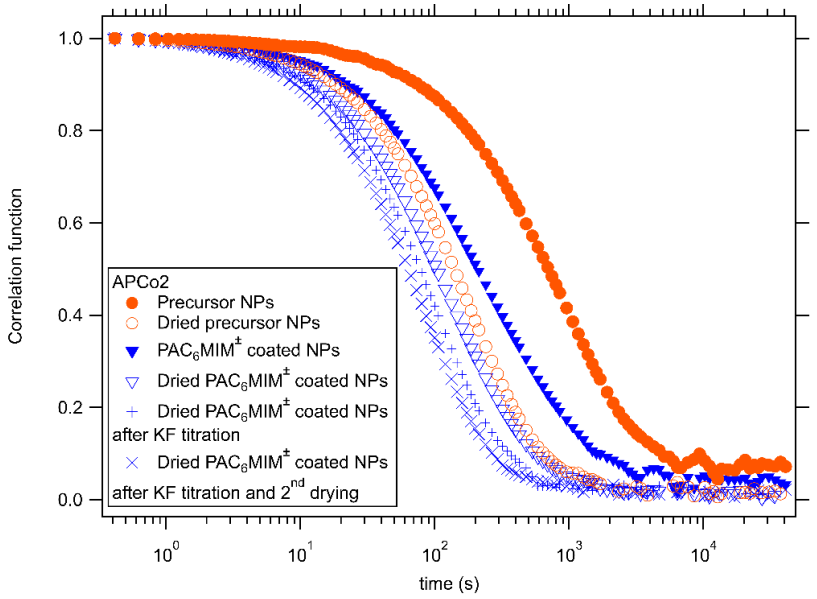

Figure 59. DLS curves for APCo2 NP samples before and after drying. All dried samples were redispersed in water at a ϕ_{NP} = 1.0%. The $PAC_6MIM^{\pm}$-coated NPs were additionally subjected to Karl Fischer titration and a second pumping cycle.

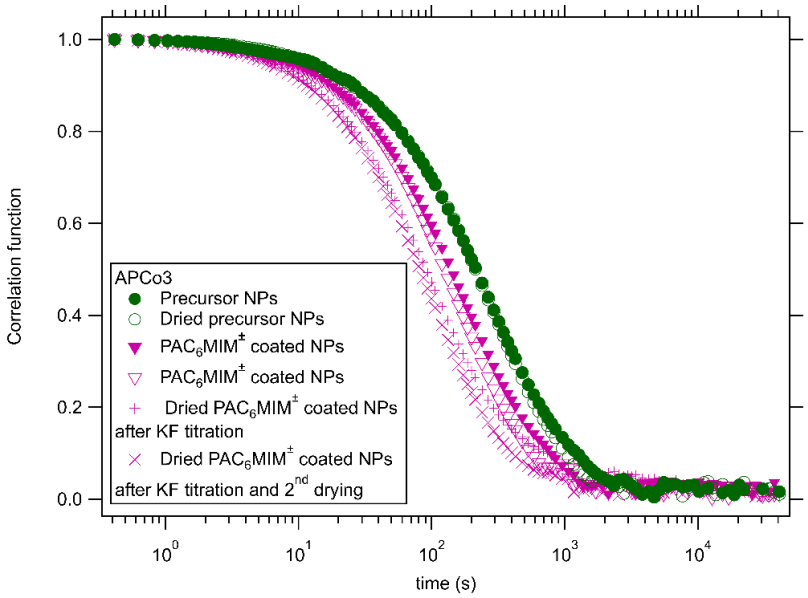

Figure 60. DLS curves for APCo3 NP samples before and after drying. All dried samples were redispersed in water at a ϕ_{NP} = 1.0%. The $PAC_6MIM^{\pm}$-coated NPs were additionally subjected to Karl Fischer titration and a second pumping cycle.

These results were confirmed by SAXS, shown in Figures 61, 62 and 63. The scattered intensity was measured for the coated NPs in water and their dispersion in water after drying by pumping and removing the water during the KF titration (150°C). For the three sizes of NPs, the scattered intensity is much lower after the pumping/heating process, the difference increasing while decreasing the NPs' size. On the contrary, with maghemite precursor samples (in nitric acid), the same process enables redispersion, however clusters are formed after redispersion, although no clusters were present at the beginning in these dispersions.

The cause of cluster breakage in the APCo1 and APCo2 samples after pumping at room temperature is not immediately clear. One possibility is that the low-pressure step may remove residual components from the synthesis that are not eliminated by dialysis under acidic conditions, which was also tested, nor by the washing steps during the NP coating process. Another possible cause is that the clusters could break apart due to increased ionic strength during the intermediate concentrated states in the drying process. This explanation is supported by literature suggesting that particles can sometimes be redispersed after drying (117). However, dispersibility is not always systematic or predictable and often requires additives to facilitate redispersion. While dispersions similar to the initial state post-drying have been reported, we are not aware of improvements in dispersion quality as observed in this case.

These results suggest new possibilities for these samples, such as using multiple cycles of drying and redispersion to break up clusters and improve their dispersion state. It raises the question of the transfer process: should all transfers be performed using the dried state as intermediate for example? We will examine these questions in the next sections.

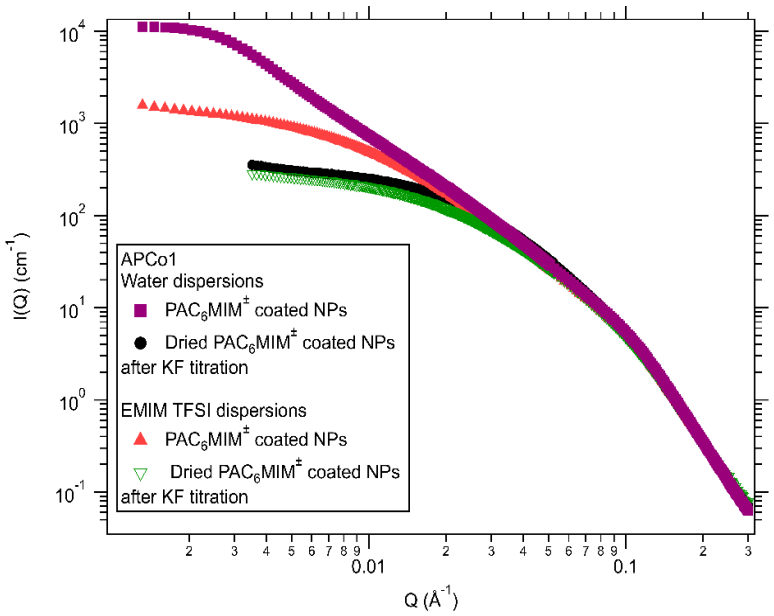

Figure 61. Scattering profile in absolute scale for APCo1 NPs dispersions in water and EMIM TFSI at ϕ_{NP} = 1.0 % varying the sample preparation.

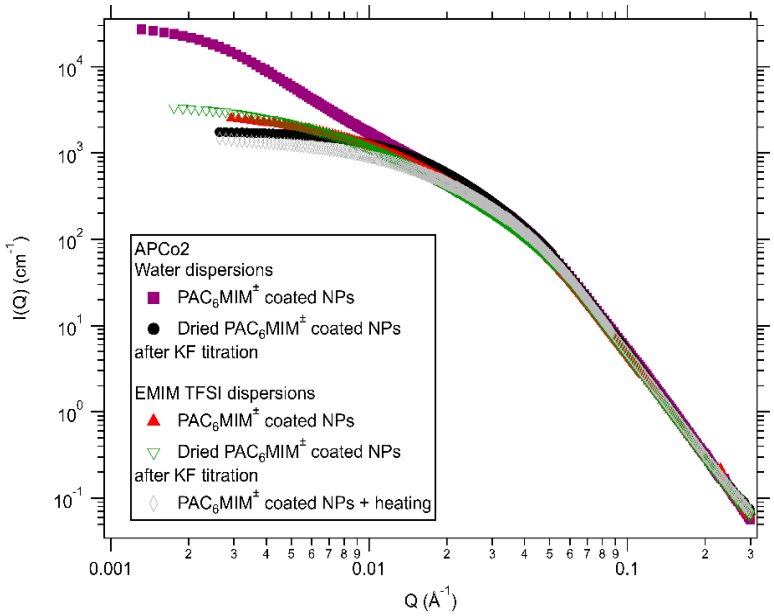

Figure 62. Scattering profile in absolute scale for APCo2 NPs dispersions in water and EMIM TFSI at ϕ_{NP} = 1.0 % varying the sample preparation.

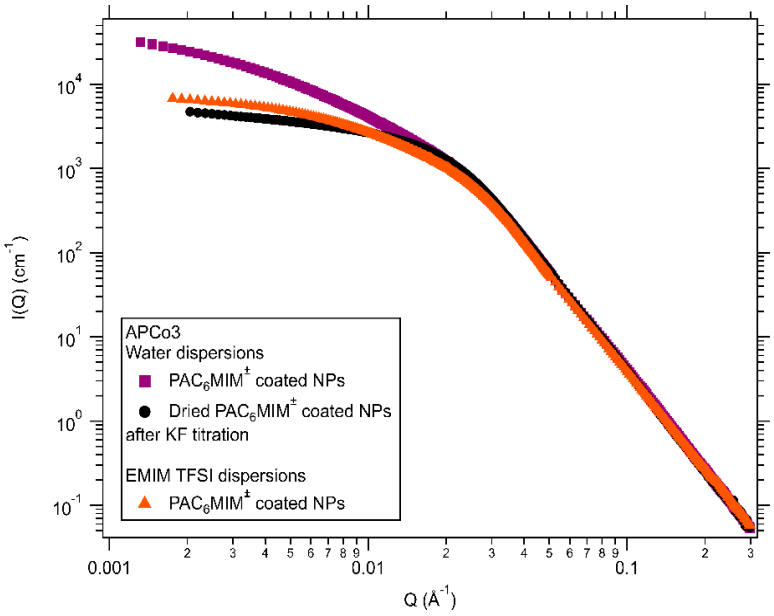

Figure 63. Scattering profile in absolute scale for APCo3 NPs dispersions in water and EMIM TFSI at ϕ_{NP} = 1.0 % varying the sample preparation.

5.6.2. Wet routes towards EMIM TFSI

In the usual route of transfer to EMIM TFSI, the water dispersion is mixed with EMIM TFSI. The NPs move from the aqueous phase to the ionic liquid phase and the water is then removed by pumping. A second route was tested replacing the initial water dispersion by the dispersions obtained after one cycle of pumping and heating at 150°C. The SAXS data are plotted in Figures 61, 62 and 63. For APCo1, the second route is much better than the usual one, clusters are reduced (Figure 61). The clusters in water and EMIM TFSI are nearly similar after this drying step. For APCo2, the second route produces clusters similar to the usual route (Figure 62), however the heating step in the ionic liquid reduces the clusters' size. Note that the experiments done in APCo2 were a little different as the NPs stayed during several weeks in the dried state before transfer to the IL. If this waiting time has some influence, it could explain the result for APCo2. This should be tested in the future. For APCo3, the second route does not produce a stable sample contrary to the usual route. However, for the three sizes of NPs, the scattered intensity of the dried sample redispersed in water is close to the intensity in the ionic liquid with the best process.

If pumping in this wet process reduces clusters, the explanation of increasing salt concentration during drying cannot apply, since the NPs are already in the ionic

liquid before pumping due to a phase transfer, and the salt concentration is already high. However, a residual component inducing aggregation can be removed. A large part of the water dissolved in the ionic liquid, either in the solvent or drawn by the NPs surface from the water phase, is also removed by the pumping step, which can also modify the clusters. Only some additional studies on the water location could help to improve our understanding.

5.6.3. The case of PC

The dispersions in PC could only be obtained from the dried NPs coated with $PAC_6MIM^{\pm}$. This was initially performed on APCo2 and later tested on APCo1 and APCo3 to assess the influence of NP size. Figure 64 shows the DLS after redispersion of the powders in PC and after heating these dispersions. The behaviour is qualitatively the same for the three samples: redispersion is possible in PC, with larger clusters for the smallest NPs, and these clusters are reduced by the heating step at 150°C. These conclusions are confirmed by the SAXS measurements of the heated samples (not shown).

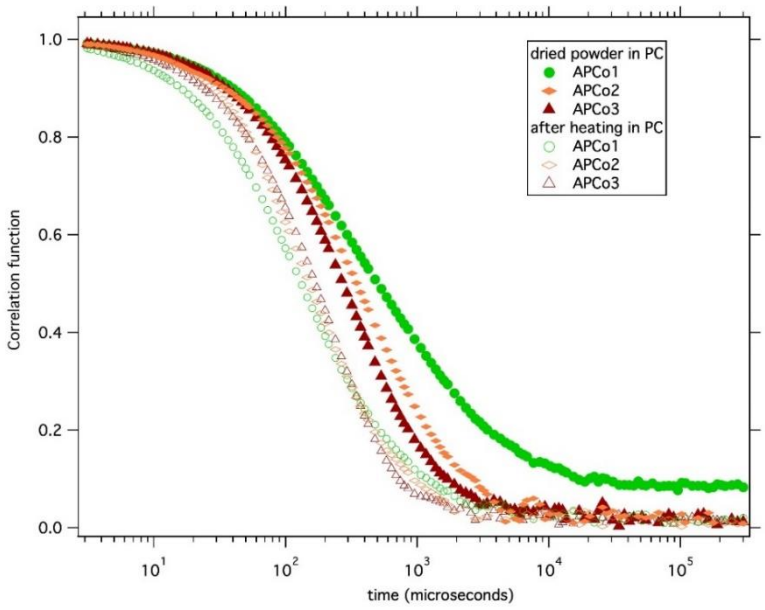

Figure 64. DLS curves for APCo1, APCo2 and APCo3 NPs after redispersion of the NPs powders in PC at ϕ_{NP} = 1.0% and after heating these dispersions at 150 °C.

5.6.4. Dispersions in EMIM TFSI of the dried NPs

The process used for PC was tested with the ionic liquid: EMIM TFSI was added to the dried powders. Figure 65 shows big clusters producing a large tail in the correlation curves. The heating of the dispersion destroys a large part of the clusters and the drying of the dispersions by pumping further improves the quality of the dispersion for APCo3. Comparing these last dispersions with the normal route shows that the clusters are smaller. The normal route with the dried/heated NPs is however better for APCo1 while it is similar for APCo3 (Figure 66).

If the origin of the clustering is not fully understood, it is clearly validated that the pumping step has a large impact, heating adding a second contribution to break the clusters. This opens new routes for the transfer to non aqueous solvents, depending on the sample. The observed differences seem to be related to the NP diameter, with APCo3 standing out, likely due to its larger NP size and stronger magnetic interactions.

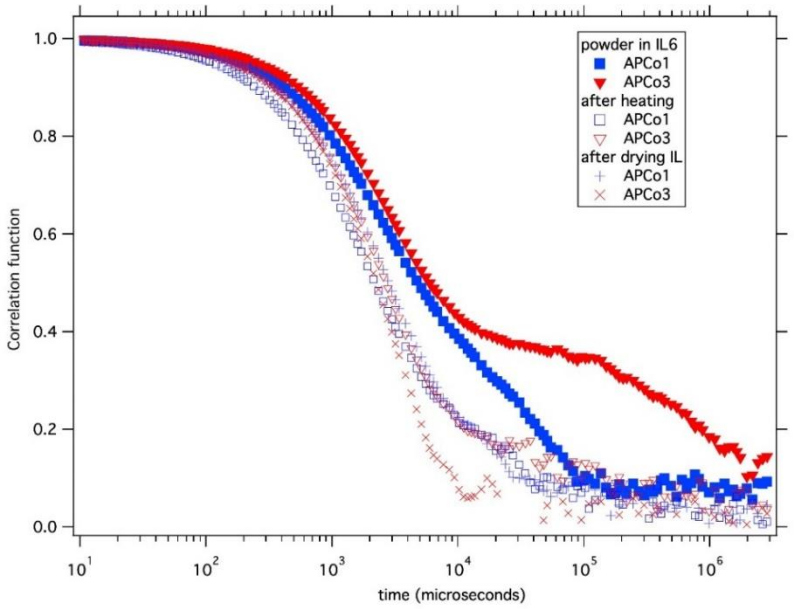

Figure 65. DLS curves for APCo1 and APCo3 NPs after redispersion of the NPs powders in EMIM TFSI at ϕ_{NP} = 1.0%, after heating these dispersions at 150°C and after drying the dispersion by pumping.

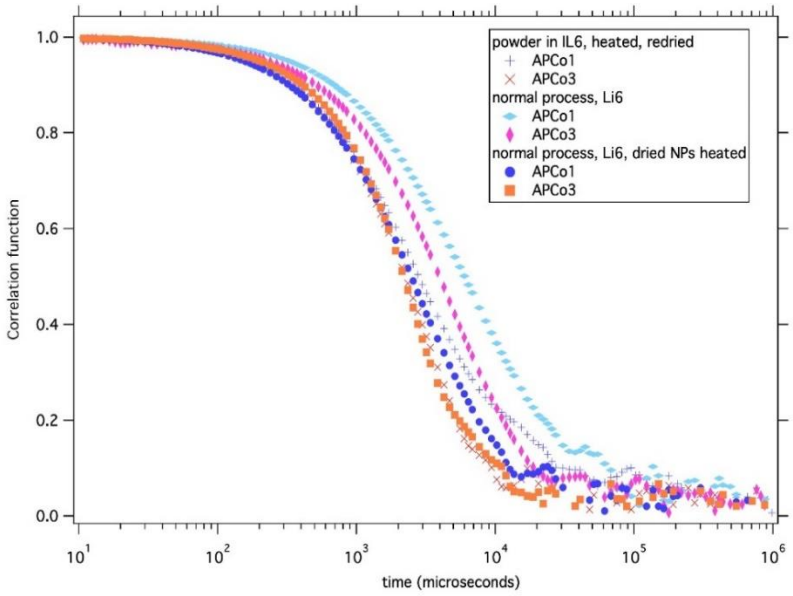

Figure 66. DLS curves for APCo1 and APCo3 NPs after redispersion of the NPs powders in EMIM TFSI at ϕ_{NP} = 1.0% followed by heating and drying by pumping, comparing to the usual route of transfer to EMIM TFSI, and to the usual route of transfer with the previously dried and heated NPs.

5.7. Summary

This chapter analyzes the colloidal stability of NPs in water, pure EMIM TFSI, pure PC, and their mixtures using DLS and SAXS. In water, $PAC_6MIM^{\pm}$-coated NPs formed clusters, with smaller NPs agglomerating more due to a reduction in saturation structural charge as their size decreases. SAXS confirmed clustering, showing fractal-like structures for APCo1 and APCo2, while APCo3 NPs formed chains and loops due to a high dipolar magnetic interaction parameter. In EMIM TFSI, cluster sizes decreased when compared to the water dispersions, with further reduction after heating. Two dispersion methods were tested to prepare NPs in pure PC. The route in which the NPs were dried before redispersion in PC plus heating for a few minutes at 80°C produced better results. Mixtures of EMIM TFSI and PC resulted in visually stable FF samples. Heating reduced the size of the clusters across all compositions. Although residual water was present, it was not the primary cause of cluster formation. Heating likely caused a reorganization of the solid-liquid interface, contributing to the improved dispersion observed in the solvents. The cause of cluster breakage in the APCo1 and APCo2 samples after pumping remains unclear, but potential explanations include the removal of residual synthesis components during the low-pressure step or increased

ionic strength during drying, both of which may enhance redispersibility. In conclusion, the results regarding the influence of pumping and heating suggest that the transfer process can be optimized by modifying or adding steps to reduce cluster size. This opens new possibilities for the samples studied in this work.

6. Conclusion and perspectives

The main conclusion of this work is that stable dispersions of core@shell ($CoFe_2O_4$@γ-Fe_2O_3) nanoparticles were successfully obtained in solvents relevant to thermoelectric applications, including pure EMIM TFSI and pure PC, two solvents at opposite ends of the ionic character spectrum. More notably, stable colloidal dispersions were also achieved in various mixtures of these two solvents, opening new possibilities for thermoelectric applications by enabling the modulation of solvent properties.

In addition to studying nanoparticle dispersions in mixtures of a selected ionic liquid and an organic polar solvent, this work also provided new insights into the influence of the nature and size of the nanoparticles. Three synthesis processes were successfully carried out, resulting in water-based ferrofluids consisting of nanoparticles with a high magnetic anisotropy due to the cobalt ferrite core, surrounded by a chemically stable thin shell of maghemite. The characterization of the ferrofluids revealed significant differences in material properties among the samples, largely due to size variations, which affect the magnetic properties, as well as the surface organization of the nanoparticles, which in turn influenced the interactions between them. Regarding colloidal stability, all ferrofluids appeared visually stable both immediately after synthesis and one year later. DLS and SAXS measurements indicated that all three ferrofluid samples were composed of stable nanoparticle clusters, with a trend showing that smaller nanoparticles tended to form larger clusters.

Regarding the nanoparticle coating for transfer to the non-aqueous solvents, the ligands with the phosphonic attaching group were effective, regardless of the carbon side-chain length. In contrast, the sulphonic-based ligand failed to produce stable dispersions, differing from previous studies with maghemite nanoparticles. This discrepancy may be related to the stronger binding affinity of the phosphonic group to the nanoparticle surface and to the composition of the NPs themselves, as cobalt ferrite has a slightly higher Hamaker constant and significantly higher magnetic anisotropy. Importantly, the dispersions showed a significant reduction in cluster size compared to the precursor FFs. Additionally, a thermal stability test for the dispersions in EMIM TFSI with the coated NPs demonstrated that the system is thermally stable, with preliminary evidence suggesting that thermal energy may break up nanoparticle clusters.

In the mixtures of EMIM TFSI and PC, stable colloidal dispersions were achieved across all tested compositions, regardless of salt concentration. This is particularly significant, as most studies on ionic liquid/solvent mixtures report flocculated dispersions. By contrast, the colloids in this work remained stable for several months, as demonstrated with a nanoparticle volume fraction of 1.0%.

In non-aqueous solvents, the nanoparticles formed smaller clusters compared to their dispersion in water, with each cluster containing only a few nanoparticles. This reduction in aggregation was experimentally achieved through a low-pressure pumping step (0.0031 mbar) to remove water, followed by a heating step at 150°C. Both steps altered the organization of the solid/liquid interface, resulting in an equilibrium state not attainable at room temperature.

The dispersions at optimal electrical conductivity and reduced viscosity (χ_{IL} = 0.20–0.3) show potential as complex liquids for studying thermoelectricity in liquid thermocells. Future research should prioritize key factors such as residual water content and its localization, as water impacts the behavior of the redox couples that will be added in the liquid in a thermoelectric cell. The interactions of the NPs with the thermocell electrode surface also need to be addressed. Additionally, optimizing nanoparticle transfer by modifying or adding steps, such as multiple cycles of drying and redispersion, could help break clusters and enhance dispersion, expanding the applications of these materials. Further studies are essential to investigate nanoparticle cluster behavior, aiming to develop a model that accurately describes both form and structure factors to deepen the understanding of the colloidal stability.

Ultimately, exploring alternative ionic liquid/solvent combinations and optimized particle compositions can expand thermoelectric applications. In particular, nanoparticles based on Co-Cu-Zn mixed ferrites hold great potential due to their tunable magnetic anisotropy and magnetization. Recent findings from our research group indicate that these types of nanoparticles can be successfully dispersed in EMIM TFSI, opening new possibilities for nanoparticle compositions with enhanced properties that could drive further advancements in the field.

Appendix

Calculation of surface coverage

To determine the surface coverage of NPs by ligands, the surface area of the NPs for each colloidal dispersion must first be calculated. This requires the calculation of the number of particles, which is determined using the particle concentration (C_{NP}) and the volume of the FF (V_{FF}) through the Equation 40:

$$N_P = C_{NP} V_{FF} \tag{40}$$

The C_{NP} can be expressed in function of ϕ by Equation 41:

$$C_{NP} = \frac{Total\ volume\ of\ np / Volume\ of np}{Volume\ of\ the\ dispersion} = \frac{6\phi}{\pi d^3} \tag{41}$$

Where d is the NP diameter, obtained from the XRD and considering the NPs as spheres.

Replacing the Equation 40 in the equation 41, the number of particles can be calculated using the Equation 42:

$$N_P = \frac{6\phi}{\pi d^3} V_{FF} \tag{42}$$

Using N_p and the area of the surface of the NP, the total area for surface coverage can be obtained by Equation 43.

$$Area = N_p \frac{\pi d^2}{4} \tag{43}$$

Finally, considering that the mass balance is maintained, the total amount of ligand added to the dispersion, subtracted by the amount obtained from the ICP-MS measurements of the supernatant provides the amount of ligand surrounding the NP. Dividing this total amount by the available area yields the surface coverage.

Low-q regime: Guinier law

As discussed in Section 2.2.10, the scattered intensity depends on q, and the analysis of the SAXS data can be divided into different regions. For the low-q region, the Guinier approximation states that the scattered intensity can be written as:

$$\ln I(q) = \ln I(0) - \frac{q^2 R_g^2}{3} \quad (44)$$

Where R_g is the radius of gyration and I(0) is the intensity at q = 0.

The R_g measures the distribution of a particle's mass around its center of mass. In the context of NPs, R_g represents the average root-mean-square distance from the center of density. It provides insight into the overall size and shape of the particle.

By plotting ln I(q) vs q^2, the resulting linear region can be fitted to obtain the slope and consequently R_g., within the range $qR_g<<1$.

Moreover, the use of diluted samples in this analysis is essential to minimize the effects of interparticle interactions, allowing the Guinier approximation to more accurately reflect the true size and shape of the particles without interference from neighboring particles.

The nonlinear behavior of the Guinier plot can result from the measured q range not being sufficiently low for a given particle size, as well as from interference effects between neighboring particles. In a system with concentrated particles, the relative distance between scattering objects may be comparable to their size. In such cases, incorporating a structure factor is necessary for a more accurate analysis.

Figure 67 illustrates the impact of particle size and agglomeration on the Guinier region.

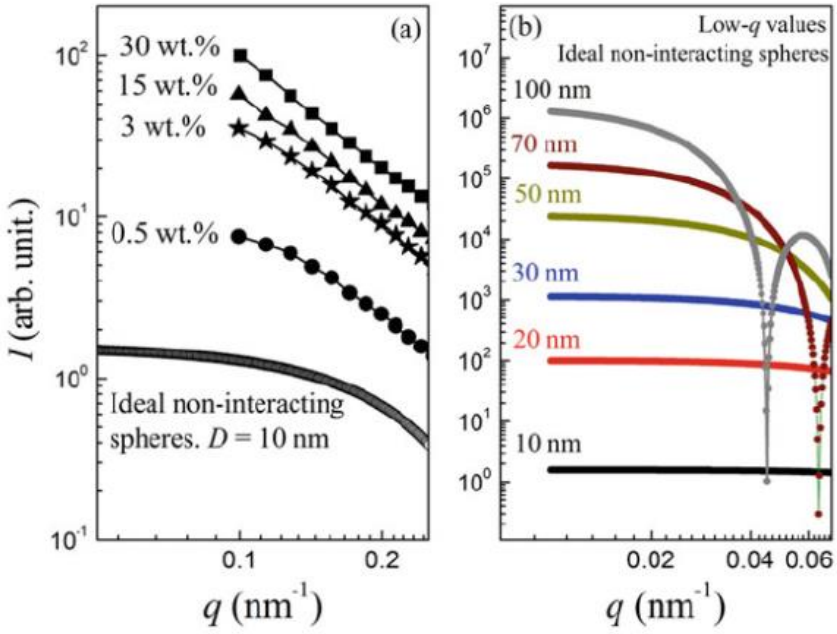

Figure 67. (a) A comparison of SAXS curves at low-q for 10 nm NPs dispersed in a non-conductive polymer matrix at four different concentrations, alongside the simulated SAXS curve for noninteracting, monodisperse 10 nm NPs. (b) Simulated SAXS curves for ideal systems of spherical NPs with varying diameters. Reproduced from (118).

In part "a" of the figure, the effect of NP concentration is evaluated. The SAXS curves correspond to experimental measurements of NPs approximately 10 nm in size dispersed in a polymer matrix, alongside a simulated curve for ideal non-interacting spheres of the same size. As NP concentration increases, the deviation from the linear behavior predicted by the Guinier law becomes more pronounced. In part "b," simulated SAXS curves for non-interacting spheres of different diameters are presented. It can be observed that the deviation from the Guinier law increases as the size of the objects grows. Therefore, for an accurate analysis of the Guinier region, it is essential to consider the effects of particle size and agglomeration, depending on the sample.

High-q regime: Porod law

For the high-q region, The Porod law describes the behavior of the scattering intensity. Assuming that both the electron densities of the particles and the medium are isotropic, the Porod law can be written as Equation 45.

$$I(q \to \infty) = 2\pi\Delta\rho^2 \frac{S}{q^4} \tag{45}$$

Where S is the specific surface of the scattering particle and $\Delta\rho^2$ is the contrast between the particles and the solvent.

The Porod region offers insights into the surface characteristics and interface properties of particles. According to the law, the scattering intensity I(q) decays as q^{-4} in this high-q region. This characteristic decay reflects the presence of sharp interfaces between different regions, such as particles and surrounding media, and provides insight into the surface-to-volume ratio of the particles or structures in the system. The slope of −4 indicates smooth, sharp boundaries, and deviations from this behavior suggest surface roughness or fractal-like structures.

Intermediate-q regime

The intermediate-q region of the SAXS curve offers valuable insights into the structural properties of the sample, particularly in the context of fractal aggregates. In this region, information about the size and arrangement of particles can be extracted, including the fractal dimensions of the system. According to the Fractal Aggregate model, aggregates are formed by N primary NPs, each with a radius r_0, that cluster together to form larger structures with mass M and an overall size ξ (the correlation length). These parameters are interrelated through Equation 46, which expresses the relationship between the mass of the aggregate and its spatial extent, taking into account the fractal dimension (D_f), a measure of how densely the particles are packed within the aggregate. The slope observed in the intermediate-q region provides direct information about the fractal dimension.

$$M \sim \xi^{D_F} \tag{46}$$

Figure 68 presents a series of representative SAXS curves for fractal structures composed of spherical primary particles with a radius of r_0 = 5 nm. The simulated curves were generated by keeping two structural parameters, r_0 and ξ, constant while varying the fractal dimension D_F. In part (a), the NP distribution is monodispersed,

while in part (b), a Gaussian size distribution was introduced to account for polydispersity in the system.

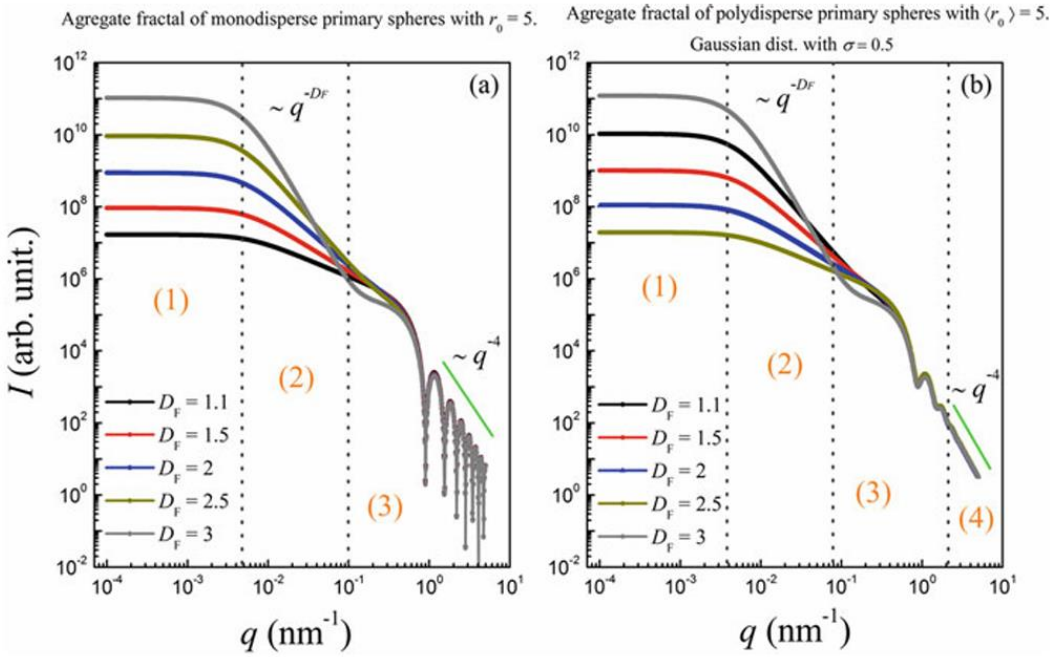

Figure 68. Simulated SAXS curves based on the FA model for (a) monodisperse and (b) polydisperse NPs. In each case, five SAXS curves were generated by varying the fractal dimension. Reproduced from (118).

In both cases, the intermediate-q region reveals a clear power-law behavior, where the scattering intensity follows $I \sim q^{-DF}$, allowing direct extraction of the fractal dimension from the slope of the curve. This power-law scaling highlights the self-similar nature of the fractal aggregates.

References

1. EIA. EIA energy outlook 2020. 2020;58(12):7250–7.
2. Biswas K, He J, Blum ID, Wu CI, Hogan TP, Seidman DN, et al. High-performance bulk thermoelectrics with all-scale hierarchical architectures. Nature. 2012;489(7416):414–8. Available from: http://dx.doi.org/10.1038/nature11439
3. Dupont MF, MacFarlane DR, Pringle JM. Thermo-electrochemical cells for waste heat harvesting-progress and perspectives. Chem Commun. 2017;53(47):6288–302. Available from: http://dx.doi.org/10.1039/C7CC02160G
4. Riffat SB, Ma X. Thermoelectrics: A review of present and potential applications. Appl Therm Eng. 2003;23(8):913–35.
5. Zheng JC. Recent advances on thermoelectric materials. Front Phys China. 2008;3(3):269–79.
6. Würger A. Transport in charged colloids driven by thermoelectricity. Phys Rev Lett. 2008;101(10):5–8.
7. Salez TJ, Huang BT, Rietjens M, Bonetti M, Wiertel-Gasquet C, Roger M, et al. Can charged colloidal particles increase the thermoelectric energy conversion efficiency? Phys Chem Chem Phys. 2017;19(14):9409–16.
8. Bonetti M, Nakamae S, Roger M, Guenoun P. Huge Seebeck coefficients in nonaqueous electrolytes. J Chem Phys. 2011;134(11).
9. Laux E, Uhl S, Jeandupeux L, López PP, Sanglard P, Vanoli E, et al. Thermoelectric Generators Based on Ionic Liquids. J Electron Mater. 2018;47(6):3193–7.
10. Prince BD, Tiruppathi P, Bemish RJ, Chiu YH, Maginn EJ. Molecular Dynamics Simulations of 1-Ethyl-3-methylimidazolium Bis[(trifluoromethyl)sulfonyl]imide Clusters and Nanodrops. J Phys Chem A. 2015;119(2):352–68.
11. Riedl JC, Akhavan Kazemi MA, Cousin F, Dubois E, Fantini S, Loïs S, et al. Colloidal dispersions of oxide nanoparticles in ionic liquids: Elucidating the key parameters. Nanoscale Adv. 2020;2(4):1560–72.
12. Fiuza T, Sarkar M, Riedl JC, Beaughon M, Torres Bautista BE, Bhattacharya K, et al. Ion specific tuning of nanoparticle dispersion in an ionic liquid: a structural, thermoelectric and thermo-diffusive investigation. Phys Chem Chem Phys. 2023;25(42):28911–24. Available from: https://xlink.rsc.org/?DOI=D3CP02399K
13. Fiuza T, Sarkar M, Riedl J, Cousin F, Demouchy G, Depeyrot J, et al. Dispersions of magnetic nanoparticles in water/ionic liquid mixtures. Faraday Discuss. 2024;253:441–57. Available from: https://xlink.rsc.org/?DOI=D4FD00028E
14. Vasilakaki M, Chikina I, Shikin VB, Ntallis N, Peddis D, Varlamov AA, et al. Towards high-performance electrochemical thermal energy harvester based on ferrofluids. Appl Mater Today. 2020;19:100587. Available from: https://doi.org/10.1016/j.apmt.2020.100587

15. Vasilakaki M, Chikina J, Shikin VB, Ntallis N, Peddis D, Varlamov AA, et al. Enhancement of the Seebeck coefficient in ferrofluid based thermoelectric materials: A numerical study. Mater Today Proc. 2019;44(xxxx):3483–8. Available from: https://doi.org/10.1016/j.matpr.2020.05.811

16. Zhu X, Yu Y, Li F. A review on thermoelectric energy harvesting from asphalt pavement: Configuration, performance and future. Constr Build Mater. 2019;228:116818. Available from: https://doi.org/10.1016/j.conbuildmat.2019.116818

17. Subramanian V, Varade D. Thermoelectric Properties of Biopolymer Composites. Biopolymer Composites in Electronics. Elsevier Inc.; 2017. 155–183 p. Available from: http://dx.doi.org/10.1016/B978-0-12-809261-3/00005-X

18. Disalvo FJ. Thermoelectric cooling and power generation. Science (80-). 1999;285(5428):703–6.

19. Hicks L, Dresselhaus MS. Thermoelectric figure of merit of a one-dimensional conductor. Phys Rev B. 1993;47(24):8–11.

20. Al-Masri D, Dupont M, Yunis R, MacFarlane DR, Pringle JM. The electrochemistry and performance of cobalt-based redox couples for thermoelectrochemical cells. Electrochim Acta. 2018;269:714–23. Available from: https://doi.org/10.1016/j.electacta.2018.03.032

21. Salez TJ, Kouyaté M, Filomeno C, Bonetti M, Roger M, Demouchy G, et al. Magnetically enhancing the Seebeck coefficient in ferrofluids. Nanoscale Adv. 2019;1(8):2979–89.

22. Sani E, Martina MR, Salez TJ, Nakamae S, Dubois E, Peyre V. Multifunctional magnetic nanocolloids for hybrid solar-thermoelectric energy harvesting. Nanomaterials. 2021;11(4).

23. Papell Solomon Stephen. Low viscosity magnetic fluid obtained by the colloidal suspension of magnetic particles. 1963;4.

24. Raj K, Moskowitz R. Commercial applications of ferrofluids. J Magn Magn Mater. 1990 Apr;85(1–3):233–45. Available from: https://linkinghub.elsevier.com/retrieve/pii/030488539090058X

25. Pankhurst QA, Connolly J, Jones SK, Dobson J. Applications of magnetic nanoparticles in biomedicine. J Phys D Appl Phys. 2003 Jul 7;36(13):R167–81. Available from: https://iopscience.iop.org/article/10.1088/0022-3727/36/13/201

26. Philip J. Magnetic nanofluids (Ferrofluids): Recent advances, applications, challenges, and future directions. Adv Colloid Interface Sci. 2023;311(November 2022):102810. Available from: https://doi.org/10.1016/j.cis.2022.102810

27. Joseph A, Mathew S. Ferrofluids: Synthetic Strategies, Stabilization, Physicochemical Features, Characterization, and Applications. Chempluschem. 2014;79(10):1382–420.

28. Riedl JC, Sarkar M, Fiuza T, Cousin F, Depeyrot J, Dubois E, et al. Design of concentrated colloidal dispersions of iron oxide nanoparticles in ionic liquids: Structure and thermal stability from 25 to 200 °C. J Colloid Interface Sci. 2022 Feb;607:584–94. Available from:

https://linkinghub.elsevier.com/retrieve/pii/S0021979721012467

29. Marsh K., Boxall J., Lichtenthaler R. Room temperature ionic liquids and their mixtures—a review. Fluid Phase Equilib. 2004 May;219(1):93–8. Available from: https://linkinghub.elsevier.com/retrieve/pii/S0378381204000962

30. Greaves TL, Drummond CJ. Protic Ionic Liquids: Properties and Applications. Chem Rev. 2008 Jan 1;108(1):206–37. Available from: https://pubs.acs.org/doi/10.1021/cr068040u

31. Angell CA, Byrne N, Belieres JP. Parallel Developments in Aprotic and Protic Ionic Liquids: Physical Chemistry and Applications. Acc Chem Res. 2007 Nov 20;40(11):1228–36. Available from: https://pubs.acs.org/doi/10.1021/ar7001842

32. Baker GA, Baker SN, Pandey S, Bright F V. An analytical view of ionic liquids. Analyst. 2005;130(6):800. Available from: https://xlink.rsc.org/?DOI=b500865b

33. Li Q, Wang S, Zhou M, Lu X, Qiao G, Li C, et al. A review of imidazolium ionic liquid-based phase change materials for low and medium temperatures thermal energy storage and their applications. Green Energy Resour. 2023;1(2).

34. He Z, Alexandridis P. Nanoparticles in ionic liquids: Interactions and organization. Phys Chem Chem Phys. 2015;17(28):18238–61. Available from: http://dx.doi.org/10.1039/C5CP01620G

35. MacFarlane DR, Tachikawa N, Forsyth M, Pringle JM, Howlett PC, Elliott GD, et al. Energy applications of ionic liquids. Energy Environ Sci. 2014;7(1):232–50. Available from: https://xlink.rsc.org/?DOI=C3EE42099J

36. Werner S, Haumann M, Wasserscheid P. Ionic liquids in chemical engineering. Annu Rev Chem Biomol Eng. 2010;1:203–30.

37. Awad WH, Gilman JW, Nyden M, Harris RH, Sutto TE, Callahan J, et al. Thermal degradation studies of alkyl-imidazolium salts and their application in nanocomposites. Thermochim Acta. 2004;409(1):3–11.

38. Xu C, Cheng Z. Thermal Stability of Ionic Liquids: Current Status and Prospects for Future Development. Processes. 2021 Feb 12;9(2):337. Available from: https://www.mdpi.com/2227-9717/9/2/337

39. Rocha MAA, Neves CMSS, Freire MG, Russina O, Triolo A, Coutinho JAP, et al. Alkylimidazolium based ionic liquids: Impact of cation symmetry on their nanoscale structural organization. J Phys Chem B. 2013;117(37):10889–97.

40. Bejaoui YKJ, Philippi F, Stammler HG, Radacki K, Zapf L, Schopper N, et al. Insights into structure–property relationships in ionic liquids using cyclic perfluoroalkylsulfonylimides. Chem Sci. 2023;14(8):2200–14. Available from: https://xlink.rsc.org/?DOI=D2SC06758G

41. GmbH proionic. Safety Data Sheet - proionic. 2023;2006(1907):1–12. Available from: www.proionic.com

42. Harris KR, Kanakubo M, Woolf LA. Temperature and Pressure Dependence of the Viscosity of the Ionic Liquids 1-Hexyl-3-methylimidazolium Hexafluorophosphate and 1-Butyl-3-methylimidazolium Bis(trifluoromethylsulfonyl)imide. J Chem Eng Data. 2007 May 1;52(3):1080–5.

Available from: https://pubs.acs.org/doi/10.1021/je700032n

43. Hauk DB, Torres RB, Dangelo JVH. Measurement and correlation of high-pressure volumetric properties of binary mixtures of 1-Ethyl-3-methylimidazolium bis(trifluoromethylsulfonyl)imide ([EMIM][NTf2]) with alcohols. J Chem Thermodyn. 2023 Oct;185:107122. Available from: https://linkinghub.elsevier.com/retrieve/pii/S0021961423001192

44. Arosa Y, Algnamat BS, Rodríguez CD, Lago EL, Varela LM, De La Fuente R. Modeling the Temperature-Dependent Material Dispersion of Imidazolium-Based Ionic Liquids in the VIS-NIR. J Phys Chem C. 2018;122(51):29470–8.

45. Chaabene N, Ngo K, Turmine M, Vivier V. New hydrophobic deep eutectic solvent for electrochemical applications. J Mol Liq. 2020 Dec;319:114198. Available from: https://linkinghub.elsevier.com/retrieve/pii/S0167732220341015

46. Al-Barghouti KS, Scurto AM. Thermal Conductivity of 1-Alkyl-3-methylimidazolium [Tf 2 N] Ionic Liquids and Compressed 1,1,1,2-Tetrafluoroethane (R-134a). J Chem Eng Data. 2022 Aug 11;67(8):1796–809. Available from: https://pubs.acs.org/doi/10.1021/acs.jced.2c00054

47. Płowaś I, Świergiel J, Jadżyn J. Electrical Conductivity in Dimethyl Sulfoxide + Potassium Iodide Solutions at Different Concentrations and Temperatures. J Chem Eng Data. 2014 Aug 14;59(8):2360–6. Available from: https://pubs.acs.org/doi/10.1021/je4010678

48. Schütte K, Meyer H, Gemel C, Barthel J, Fischer RA, Janiak C. Synthesis of Cu, Zn and Cu/Zn brass alloy nanoparticles from metal amidinate precursors in ionic liquids or propylene carbonate with relevance to methanol synthesis. Nanoscale. 2014;6(6):3116. Available from: https://xlink.rsc.org/?DOI=c3nr05780a

49. Haynes WM, Lide DR, Bruno TJ, editors. CRC Handbook of Chemistry and Physics. CRC Press; 2016. Available from: https://www.taylorfrancis.com/books/9781498754293

50. Daubert TE, Danner RP. Physical and thermodynamic properties of pure chemicals : data compilation. Washington, DC: Taylor & Francis; 1989.

51. Levy NR, Lifshits S, Yohanan E, Ein-Eli Y. Hybrid Ionic Liquid Propylene Carbonate-Based Electrolytes for Aluminum-Air Batteries. ACS Appl Energy Mater. 2020;3(3):2585–92.

52. Lam PH, Tran AT, Walczyk DJ, Miller AM, Yu L. Conductivity, viscosity, and thermodynamic properties of propylene carbonate solutions in ionic liquids. J Mol Liq. 2017;246:215–20. Available from: http://dx.doi.org/10.1016/j.molliq.2017.09.070

53. Belloni L. Colloidal interactions. J Phys Condens Matter. 2000;12(46).

54. Pashley RM, Karaman ME. Applied Colloid and Surface Chemistry. Appl Colloid Surf Chem. 2004;1.

55. Faure B, Salazar-Alvarez G, Bergström L. Hamaker constants of iron oxide nanoparticles. Langmuir. 2011;27(14):8659–64.

56. Hamaker HC. The London—van der Waals attraction between spherical

particles. Physica. 1937 Oct;4(10):1058–72. Available from: https://linkinghub.elsevier.com/retrieve/pii/S0031891437802037

57. Park SJ, Seo MK. Intermolecular Force. In 2011. p. 1–57. Available from: https://linkinghub.elsevier.com/retrieve/pii/B9780123750495000013

58. Prakash S, Yeom J. Fundamentals for Microscale and Nanoscale Flows. In: Nanofluidics and Microfluidics. Elsevier; 2014. p. 9–38. Available from: https://linkinghub.elsevier.com/retrieve/pii/B9781437744699000020

59. Baalousha M. Effect of nanomaterial and media physicochemical properties on nanomaterial aggregation kinetics. NanoImpact. 2017;6:55–68. Available from: http://dx.doi.org/10.1016/j.impact.2016.10.005

60. Dukhin AS, Goetz PJ. Fundamentals of interface and colloid science. Stud Interface Sci. 2010;24(C):21–89.

61. Piacenza E, Presentato A, Turner RJ. Stability of biogenic metal(loid) nanomaterials related to the colloidal stabilization theory of chemical nanostructures. Crit Rev Biotechnol. 2018;38(8):1137–56. Available from: https://doi.org/10.1080/07388551.2018.1440525

62. Cousin F, Dubois E, Cabuil V. Tuning the interactions of a magnetic colloidal suspension. Phys Rev E. 2003 Aug 15;68(2):021405. Available from: https://link.aps.org/doi/10.1103/PhysRevE.68.021405

63. Cullity BD. Introduction to Magnetic Materials. Addison-Wesley Publishing Company: Reading; 1972.

64. Landau LD, Lifshitz EM. Statistical Physics. Oxford; 1980.

65. Li X, Xu J. 6.5 Metal Matrix Nanocomposites. In: Comprehensive Composite Materials II. Elsevier; 2018. p. 97–137. Available from: https://linkinghub.elsevier.com/retrieve/pii/B9780128035818100281

66. Nikolov AD, Wasan DT, Wu P. Solvation forces versus the nano-colloidal structural forces under the film confinement: Layer to in-layer structural transition in wetting solids. Curr Opin Colloid Interface Sci. 2022 Feb;57:101539. Available from: https://linkinghub.elsevier.com/retrieve/pii/S1359029421001230

67. Zhang H, Dasbiswas K, Ludwig NB, Han G, Lee B, Vaikuntanathan S, et al. Stable colloids in molten inorganic salts. Nature. 2017;542(7641):328–31. Available from: http://dx.doi.org/10.1038/nature21041

68. Bazant MZ, Storey BD, Kornyshev AA. Double layer in ionic liquids: Overscreening versus crowding. Phys Rev Lett. 2011;106(4):6–9.

69. Kislenko SA, Moroz YO, Karu K, Ivaništšev VB, Fedorov M V. Calculating the Maximum Density of the Surface Packing of Ions in Ionic Liquids. Russ J Phys Chem A. 2018;92(5):999–1005.

70. V. Ivanistsev V, Kirchner K, Kirchner T, O'Connor, Fedorov M V. Modelling and Analysis of Interfacial Structural Transitions in Ionic Liquids at Charged Interfaces. 2015;(October):107–27.

71. Bernardino K. How Domain Segregation in Ionic Liquids Stabilizes

Nanoparticles and Establishes Long-Range Ordering─A Computational Study. ACS Nano. 2024;18(31):20389–400.

72. Francis R, Joy N, Aparna EP, Vijayan R. Polymer grafted inorganic nanoparticles, preparation, properties, and applications: A review. Polym Rev. 2014;54(2):268–347.

73. Imadadulla M, Nemakal M, Koodlur Sannegowda L. Solvent dependent dispersion behaviour of macrocycle stabilized cobalt nanoparticles and their applications. New J Chem. 2018;42(14):11364–72.

74. Chakraborty S, Sahoo B, Teraoka I, Gross RA. Solution properties of starch nanoparticles in water and DMSO as studied by dynamic light scattering. Carbohydr Polym. 2005;60(4):475–81.

75. Sarkar B, Venugopal V, Bodratti AM, Tsianou M, Alexandridis P. Nanoparticle surface modification by amphiphilic polymers in aqueous media: Role of polar organic solvents. J Colloid Interface Sci. 2013;397:1–8.

76. Kirillov VL, Yakushkin SS, Balaev DA, Dubrovskiy AA, Semenov S V., Knyazev Y V., et al. Dimethylsulfoxide as a media for one-stage synthesis of the Fe 3 O 4 -Based ferrofluids with a controllable size distribution. Mater Chem Phys. 2019;225(December 2018):292–7.

77. Sarkar M, Riedl JC, Demouchy G, Gélébart F, Mériguet G, Peyre V, et al. Inversion of thermodiffusive properties of ionic colloidal dispersions in water-DMSO mixtures probed by forced Rayleigh scattering. Eur Phys J E. 2019;42(6):1–10.

78. Vollmer C, Thomann R, Janiak C. Organic carbonates as stabilizing solvents for transition-metal nanoparticles. Dalt Trans. 2012;41(32):9722–7.

79. Schütte K, Barthel J, Endres M, Siebels M, Smarsly BM, Yue J, et al. Synthesis of Metal Nanoparticles and Metal Fluoride Nanoparticles from Metal Amidinate Precursors in 1-Butyl-3-Methylimidazolium Ionic Liquids and Propylene Carbonate. ChemistryOpen. 2017;6(1):137–48.

80. Afanasiev P. Synthesis of finely divided molybdenum sulfide nanoparticles in propylene carbonate solution. J Solid State Chem. 2014;213:158–64.

81. Szilagyi I, Szabo T, Desert A, Trefalt G, Oncsik T, Borkovec M. Particle aggregation mechanisms in ionic liquids. Phys Chem Chem Phys. 2014;16(20):9515–24. Available from: https://xlink.rsc.org/?DOI=C4CP00804A

82. Smith JA, Werzer O, Webber GB, Warr GG, Atkin R. Surprising Particle Stability and Rapid Sedimentation Rates in an Ionic Liquid. J Phys Chem Lett. 2010 Jan 7;1(1):64–8. Available from: https://pubs.acs.org/doi/10.1021/jz9000642

83. Takács D, Tomšič M, Szilagyi I. Effect of Water and Salt on the Colloidal Stability of Latex Particles in Ionic Liquid Solutions. Colloids and Interfaces. 2021 Dec 31;6(1):2. Available from: https://www.mdpi.com/2504-5377/6/1/2

84. Sakai K, Okada K, Uka A, Misono T, Endo T, Sasaki S, et al. Effects of Water on Solvation Layers of Imidazolium-Type Room Temperature Ionic Liquids on Silica and Mica. Langmuir. 2015 Jun 9;31(22):6085–91. Available from:

https://pubs.acs.org/doi/10.1021/acs.langmuir.5b01184

85. Oh KI, Rajesh K, Stanton JF, Baiz CR. Quantifying Hydrogen-Bond Populations in Dimethyl Sulfoxide/Water Mixtures. Angew Chemie - Int Ed. 2017;56(38):11375–9.

86. Tourinho FA, Franck R, Massart R. Aqueous ferrofluids based on manganese and cobalt ferrites. J Mater Sci. 1990;25(7):3249–54.

87. Gomes JDA, Sousa MH, Tourinho FA, Aquino R, Da Silva GJ, Depeyrot J, et al. Synthesis of core-shell ferrite nanoparticles for ferrofluids: Chemical and magnetic analysis. J Phys Chem C. 2008;112(16):6220–7.

88. Aquino R, Tourinho FA, Itri R, E Lara MCFL, Depeyrot J. Size control of MnFe2O4 nanoparticles in electric double layered magnetic fluid synthesis. J Magn Magn Mater. 2002;252(1-3 SPEC. ISS.):23–5.

89. Vraneš M, Papović S, Idrissi A, Zec N, Panaget T, Ajduković J, et al. New methylpyridinium ionic liquids – Influence of the position of –CH3 group on physicochemical and structural properties. J Mol Liq. 2019;283:208–20.

90. Hamelin J, Bose TK, Thoen J. Dielectric constant and the electric conductivity near the consolute point of the critical binary liquid mixture nitroethane–3-methylpentane. Phys Rev A. 1990 Oct 1;42(8):4735–42. Available from: https://link.aps.org/doi/10.1103/PhysRevA.42.4735

91. Stetefeld J, McKenna SA, Patel TR. Dynamic light scattering: a practical guide and applications in biomedical sciences. Biophys Rev. 2016;8(4):409–27. Available from: http://dx.doi.org/10.1007/s12551-016-0218-6

92. Krumrey M. Small angle x-ray scattering (SAXS). In: Characterization of Nanoparticles. Elsevier; 2020. p. 173–83. Available from: https://linkinghub.elsevier.com/retrieve/pii/B9780128141823000110

93. Paula FLO, Aquino R, Da Silva GJ, Depeyrot J, Tourinho FA, Fossum JO, et al. Small-angle X-ray and small-angle neutron scattering investigations of colloidal dispersions of magnetic nanoparticles and clay nanoplatelets. J Appl Crystallogr. 2007;40:269–73.

94. Gazeau F, Dubois E, Bacri JC, Boué F, Cebers A, Perzynski R. Anisotropy of the structure factor of magnetic fluids under a field probed by small-angle neutron scattering. Phys Rev E - Stat Physics, Plasmas, Fluids, Relat Interdiscip Top. 2002;65(3):1–15.

95. Schmool DS, Kachkachi H. Collective Effects in Assemblies of Magnetic Nanoparticles. In 2016. p. 1–101. Available from: https://linkinghub.elsevier.com/retrieve/pii/S0081194716300029

96. Scherdel C, Miller E, Reichenauer G, Schmitt J. Advances in the Development of Sol-Gel Materials Combining Small-Angle X-ray Scattering (SAXS) and Machine Learning (ML). Processes. 2021 Apr 11;9(4):672. Available from: https://www.mdpi.com/2227-9717/9/4/672

97. Mériguet G, Wandersman E, Dubois E, Cebers A, de Andrade Gomes J, Demouchy G, et al. Magnetic fluids with tunable interparticle interaction: Monitoringtheunder-fieldlocal structure. Magnetohydrodynamics.

2012;48(2):415–26.

98. Djaniš JP, Prinčič GG, Mavrič A, Mertelj A, Iskra J, Lisjak D. New Insights into Amino-Functionalization of Magnetic Nanoplatelets with Silanes and Phosphonates. Nanomaterials. 2022;12(12).

99. Metzger M, Strehle B, Solchenbach S, Gasteiger HA. Hydrolysis of Ethylene Carbonate with Water and Hydroxide under Battery Operating Conditions. J Electrochem Soc. 2016 Apr 14;163(7):A1219–25. Available from: https://iopscience.iop.org/article/10.1149/2.0411607jes

100. Kneller EF, Luborsky FE. Particle size dependence of coercivity and remanence of single-domain particles. J Appl Phys. 1963;34(3):656–8.

101. Gomide G, Cabreira Gomes R, Gomes Viana M, Cortez Campos AF, Aquino R, López-Ortega A, et al. Nanoparticle Size Distribution and Surface Effects on the Thermal Dependence of Magnetic Anisotropy. J Phys Chem C. 2022 Jan 27;126(3):1581–9. Available from: https://pubs.acs.org/doi/10.1021/acs.jpcc.1c06664

102. Nunes WC, Folly WSD, Sinnecker JP, Novak MA. Temperature dependence of the coercive field in single-domain particle systems. Phys Rev B - Condens Matter Mater Phys. 2004;70(1):1–6.

103. Lin MY, Lindsay HM, Weitz DA, Ball RC, Klein R, Meakin P. Universal reaction-limited colloid aggregation. Phys Rev A. 1990 Feb 1;41(4):2005–20. Available from: https://link.aps.org/doi/10.1103/PhysRevA.41.2005

104. Campos AFC, Aquino R, Tourinho FA, Paula FLO, Depeyrot J. Influence of the spatial confinement at nanoscale on the structural surface charging in magnetic nanocolloids. Eur Phys J E. 2013;36(4).

105. Hunt PA. Why does a reduction in hydrogen bonding lead to an increase in viscosity for the 1-Butyl-2,3-dimethyl-imidazolium-based ionic liquids? J Phys Chem B. 2007;111(18):4844–53.

106. Vraneš M, Zec N, Tot A, Papović S, Dožić S, Gadžurić S. Density, electrical conductivity, viscosity and excess properties of 1-butyl-3-methylimidazolium bis(trifluoromethylsulfonyl)imide + propylene carbonate binary mixtures. J Chem Thermodyn. 2014;68:98–108.

107. Hofmann A, Migeot M, Hanemann T. Investigation of Binary Mixtures Containing 1-Ethyl-3-methylimidazolium Bis(trifluoromethanesulfonyl)azanide and Ethylene Carbonate. J Chem Eng Data. 2016;61(1):114–23.

108. Van Raap MBF, Zélis PM, Coral DF, Torres TE, Marquina C, Goya GF, et al. Self organization in oleic acid-Coated CoFe2O4 colloids: A SAXS study. J Nanoparticle Res. 2012;14(9).

109. Goodwin WB, Shin D, Sabo D, Hwang S, Zhang ZJ, Meredith JC, et al. Tunable multimodal adhesion of 3D, nanocrystalline CoFe 2 O 4 pollen replicas. Bioinspir Biomim. 2017 Nov 6;12(6):066009. Available from: https://iopscience.iop.org/article/10.1088/1748-3190/aa7c89

110. Lisjak D, Hribar Boštjančič P, Hribar Boštjančič P, Mertelj A, Mavrič A, Mavrič A, et al. Formation of Fe(III)-phosphonate Coatings on Barium Hexaferrite

Nanoplatelets for Porous Nanomagnets. ACS Omega. 2020;5(23):14086–95.

111. Weerasooriya R, Wickramarathna HUS. Modeling anion adsorption on kaolinite. J Colloid Interface Sci. 1999;213(2):395–9.

112. Frka-Petesic B, Dubois E, Almasy L, Dupuis V, Cousin F, Perzynski R. Structural probing of clusters and gels of self-aggregated magnetic nanoparticles. Magnetohydrodynamics. 2013;49(3–4):328–38.

113. Novak E V., Pyanzina ES, Sánchez PA, Kantorovich SS. The structure of clusters formed by Stockmayer supracolloidal magnetic polymers. Eur Phys J E. 2019 Dec 23;42(12):158. Available from: http://link.springer.com/10.1140/epje/i2019-11924-6

114. Mamusa M, Sirieix-Plénet J, Perzynski R, Cousin F, Dubois E, Peyre V. Concentrated assemblies of magnetic nanoparticles in ionic liquids. Faraday Discuss. 2015;181:193–209. Available from: https://xlink.rsc.org/?DOI=C5FD00019J

115. Han M, Espinosa-Marzal RM. Influence of Water on Structure, Dynamics, and Electrostatics of Hydrophilic and Hydrophobic Ionic Liquids in Charged and Hydrophilic Confinement between Mica Surfaces. ACS Appl Mater Interfaces. 2019 Sep 11;11(36):33465–77. Available from: https://pubs.acs.org/doi/10.1021/acsami.9b10923

116. Williamson AG, Catherall NF. Mutual solubilities of propylene carbonate and water. J Chem Eng Data. 1971 Jul 1;16(3):335–6. Available from: https://pubs.acs.org/doi/abs/10.1021/je60050a021

117. Shrestha S, Wang B, Dutta P. Nanoparticle processing: Understanding and controlling aggregation. Adv Colloid Interface Sci. 2020 May;279:102162. Available from: https://linkinghub.elsevier.com/retrieve/pii/S0001868619304816

118. Londoño OM, Tancredi P, Rivas P, Muraca D, Socolovsky LM, Knobel M. Small-Angle X-Ray Scattering to Analyze the Morphological Properties of Nanoparticulated Systems. In: Handbook of Materials Characterization. Cham: Springer International Publishing; 2018. p. 37–75. Available from: http://link.springer.com/10.1007/978-3-319-92955-2_2

DECLARAÇÃO DE ORIGINALIDADE DE DISSERTAÇÃO DE MESTRADO OU TESE DE DOUTORADO

Declaro que a presente dissertação/tese é original, elaborada especialmente para este fim, não tendo sido apresentada para obtenção de qualquer título e que identifico e cito devidamente todas as autoras e todos os autores que contribuíram para o trabalho, bem como as contribuições oriundas de outras publicações de minha autoria.

Declaro estar ciente de que a cópia ou o plágio podem gerar responsabilidade civil, criminal e disciplinar, consistindo em grave violação à ética acadêmica.

Brasília, 17 de dezembro de 2024

Assinatura do/a discente: Ana Alice Andrade Meireles Guerra

Programa: Programa de Pós-graduação em Química

Nome completo: Ana Alice Andrade Meireles Guerra

Título do Trabalho: Dispersões de nanopartículas de ferrita do tipo espinélio em solventes à base de líquidos iônicos para aplicações termoelétricas (Dispersions of spinel ferrite nanoparticles in ionic liquid-based solvents in view of thermoelectric applications)

Nível: ( ) Mestrado (x) Doutorado

Orientador/a: Alex Fabiano Cortez Campos /Emmanuelle Dubois